

DEVELOPMENT OF A SMART MATERIAL  
ELECTROHYDROSTATIC ACTUATOR  
CONSIDERING RECTIFICATION VALVE DYNAMICS  
AND IN SITU VALVE CHARACTERIZATION

A Thesis

Presented in Partial Fulfillment of the Requirements for  
the Degree Master of Science in the  
Graduate School of The Ohio State University

By

Thomas E. Walters, B.S.

\* \* \* \* \*

The Ohio State University

2008

Master's Examination Committee:

Dr. Marcelo Dapino, Adviser

Dr. Krishnaswamy (Cheena) Srinivasan

Approved by

---

Adviser

Graduate Program in  
Mechanical Engineering

© Copyright by  
Thomas E. Walters  
2008

## ABSTRACT

Owing to advantages in maintainability, weight, and system integration, there is a developing trend in the automotive and aerospace industries toward replacing traditional actuation systems with devices that are powered through electrical wires (power-by-wire). Smart material driven actuation systems provide the major advantages of power-by-wire systems with the additional benefits of superior spectral response, high power-to-weight ratio, and solid-state operation. A smart material electrohydrostatic actuator (EHA) is an electrically driven, self-contained actuator driven by the high-force vibrations of its smart material core. The smart material pump of an EHA must be driven at frequencies in the kHz range to achieve required flow rates. It follows that the outlet and inlet valves of the pump must be able to effectively convert the high pressure fluid pulses to continuous flow in the output hydraulic cylinder at these high frequencies. The flow control valves that perform this process, termed fluid rectification, along with the smart material EHA are the focal points for this research.

Lumped parameter system model techniques are used to represent the mechanical and fluid domains of a smart material EHA. The parameters for the mechanical model of the reed-type rectification valves are developed considering fluid loading and proximity effects. Fluid dynamic, finite element simulations are used to couple the bending motion of the valve to its effective flow resistance in the fluid domain. The

system model is formulated based on a prototype pump driven by the magnetic field-induced vibrations of the magnetostrictive material Terfenol-D. The system model is solved in MATLAB SIMULINK using a built-in ODE solver.

Correlation of model simulations and test data for a Terfenol-D pump under no-flow conditions up to a pumping frequency of 1200 Hz validates the parameters of the rectification valve model. Loaded actuator simulations show that the rectification valve dynamics limit the velocity bandwidth of the actuator relative to ideal valve behavior in the system model. The model predicts that higher actuation velocities can be obtained by increasing the velocity bandwidth of the actuator through increasing the resonant frequency of the rectification valves.

A novel method for in situ characterization of the outlet rectification valve and system level experiments for a Terfenol-D pump is presented along with measured data for the prototype Terfenol-D pump. Testing provides important data from the pump and validates the novel measurement method which expands the capability to characterize a magnetostrictive pump.

The contribution of this work is the development of a dynamic model for fluid rectification valves and implementation for a magnetostrictive pump as well as a technique for in situ characterization of smart material actuation systems.

## ACKNOWLEDGMENTS

My success is not entirely my own. My completion of this thesis and master's degree is the result of several individuals' superior effort and dedication. Thanks to the Ohio State University for allowing me to join, if only for a short while, a great academic community. Thanks also to the Graduate School and Department of Mechanical Engineering for funding my first year of research through a University Fellowship and providing the resources essential to making my education here a true success. I would like to express my gratitude to my advisor, Marcelo Dapino, for giving me the opportunity to work on an exciting and challenging project and for simply making me a better professional. Thanks also to Professor K. Cheena Srinivasan for helpful inquiries and sitting on my master's exam committee. I would also like to acknowledge the effort of Tom Greetham at Moog, Inc. for technical support and guidance throughout this research. I would like to also acknowledge my current source of funding, the National Science Foundation Industry & University Collaborative Research Center on Smart Vehicle Concepts.

I would like to thank Miami University and their Mechanical and Manufacturing Engineering Department for providing me with an outstanding undergraduate education and preparing me for success at the graduate level. Thanks to Professors Anna Dollár and Amit Shukla for believing in me and encouraging me to pursue a graduate degree. Every student coming through the MME department, including myself,

is inspired by the enthusiasm and passion of Professor Osama Ettouney who is an incredible mentor and friend.

My fellow graduate students have had quite an impact on my experience. To the members of the Smart Materials and Structures lab, I appreciate the help and guidance you've given me. I wish all of you the best in your future endeavors. Thanks to all my peers in the Mechanical Engineering department who've enriched my experience here; good luck to you all. A special thanks to Chris Cooley and Bob Lowe for sharing with me all the extraordinary experiences graduate school has to offer.

I've come to this point in my life principally due to the love and support of my family and friends. To my brothers, Joe and Zach, my grandparents, Pete and Millie, my uncles, aunts, cousins, and sister-in-law, thank you for your endless support and sacrifices. You have given me something to aspire to personally and professionally. To my nephew Aaron, who can always make me smile. Thank you to all my friends for giving me so many irreplaceable experiences and for your boundless optimism. Finally, and most importantly, I could not have come this far without the enormous sacrifices, unconditional love, guidance, patience, and encouragement of my wonderful parents, Greg and Marsha. Thank you both for all that you've done to make me who I am.

## VITA

September 25, 1983 ..... Born - Middletown, Ohio

June 2001 ..... Honors Diploma, Preble Shawnee  
High School

December 2005 ..... B.S. Mechanical Engineering &  
Manufacturing Engineering Magna  
Cum Laude, Miami University

2006 - 2007 ..... Graduate Fellow, The Ohio State Uni-  
versity

2007 - Present ..... NSF I/UCRC Smart Vehicle Concepts  
Center Fellow, The Ohio State Univer-  
sity

## FIELDS OF STUDY

Major Field: Mechanical Engineering

Studies in Smart Materials and Structures: Dr. Marcelo Dapino

Major Field: Mechanical and Manufacturing Engineering

## TABLE OF CONTENTS

	Page
Abstract . . . . .	ii
Acknowledgments . . . . .	iv
Vita . . . . .	vi
List of Tables . . . . .	x
List of Figures . . . . .	xi
Chapters:	
1. Introduction . . . . .	1
2. Background Information . . . . .	5
2.1 Motivation . . . . .	5
2.2 Objectives . . . . .	7
2.3 Smart Materials . . . . .	8
2.3.1 Overview . . . . .	8
2.3.2 Magnetostrictive Materials . . . . .	9
2.4 Smart Material Applications . . . . .	19
2.4.1 Overview . . . . .	19
2.4.2 Magnetostrictive Applications . . . . .	20
2.5 Smart Material Pumps and EHAs . . . . .	21
2.5.1 Principle of Operation . . . . .	22
2.5.2 Performance Characterization . . . . .	24
2.5.3 Literature Review . . . . .	26

3.	Modeling . . . . .	30
3.1	Mechanical Model . . . . .	31
3.1.1	Terfenol-D Pump . . . . .	31
3.1.2	Hydraulic Cylinder and Piston . . . . .	32
3.1.3	Rectification Reed Valves . . . . .	33
3.2	Fluid Model . . . . .	42
3.2.1	Fluid Bulk Modulus . . . . .	42
3.2.2	Lumped Fluid Resistance and Capacitance . . . . .	43
3.2.3	Hydraulic Circuit . . . . .	44
3.2.4	Fluid-Structure Coupling . . . . .	47
3.3	System Model . . . . .	52
3.3.1	System Model Equations . . . . .	52
3.3.2	Summary of System Model Parameters . . . . .	54
4.	Terfenol-D Pump and Reed Valve Testing . . . . .	56
4.1	Terfenol-D Pump Details . . . . .	56
4.2	Terfenol-D Pump Testing Setup . . . . .	58
4.2.1	Terfenol-D Rod Pre-Load . . . . .	59
4.3	In Situ Valve Measurement Setup . . . . .	61
4.3.1	Laser Sensor (LK-G32) . . . . .	61
4.3.2	Design and Manufacture of Modified Pump Cap . . . . .	62
4.3.3	Reed Valve Displacement Measurement . . . . .	64
4.4	Measurement Setup . . . . .	66
5.	Results and Discussion . . . . .	73
5.1	No-Flow Pressure Simulation and Testing . . . . .	73
5.1.1	No-Flow Pressure Trace . . . . .	73
5.1.2	No-Flow Pressure Response . . . . .	74
5.2	Loaded Actuator Simulation . . . . .	79
5.2.1	Characterization of Prototype EHA . . . . .	79
5.2.2	EHA Velocity Bandwidth Investigation . . . . .	82
5.3	Modeling Discussion . . . . .	84
5.4	In Situ EHA Characterization . . . . .	87
6.	Concluding Remarks . . . . .	93
6.1	Summary of Results and Contribution . . . . .	93
6.2	Research Opportunities . . . . .	95

Appendices:

A.	System Model Parameter Summary . . . . .	98
B.	Galfenol Unimorph Testing . . . . .	99
B.1	Experimental Setup . . . . .	99
B.2	Quasi-static Testing Results . . . . .	100
B.2.1	Displacement Results . . . . .	100
B.2.2	Blocked Force Results . . . . .	101
C.	Detailed Drawings . . . . .	104
	Bibliography . . . . .	106

## LIST OF TABLES

Table	Page
3.1 Summary of rectification reed valve properties. . . . .	36
3.2 Comparison of bimorph cantilever used by Naik et al. [36] and rectification reed valves used in EHA. Values denoted with (*) are approximate due to irregular geometry. . . . .	39
3.3 Comparison of fluid (FC-70) used by Naik et al. [36] and EHA working fluid (Mobil DTE25) used in EHA. . . . .	39
3.4 Summary of results for added mass and damping effects for bimorph cantilever submerged in FC-70 fluid by Naik et al. [36]. . . . .	40
3.5 Summary of parameters for Terfenol-D transducer, Terfenol-D pump, and rectification reed valve models in the mechanical and fluid domains.	54
3.6 Summary of parameters for the smart material EHA output cylinder, hydraulic circuit, and fluid accumulator. . . . .	55
A.1 System model parameters for the Terfenol-D pump, chamber, and rectification valves. . . . .	98
B.1 Galfenol unimorph samples tested for free displacement and blocked force. Galfenol is 0.015 inches thick and all samples have a length of 2 inches and a width of 0.25 inches. . . . .	100

## LIST OF FIGURES

Figure	Page
2.1 Illustration of the atomic contribution to magnetic moments and magnetic domains in a bulk magnetostrictive material. . . . .	11
2.2 Illustration of (a) magnetic domains above Curie temperature (b) spontaneous magnetostriction and (c) field-induced magnetostriction. . . .	12
2.3 Schematic of (a) random orientation of moments for unbiased magnetostrictive rod and (b) simplified plot of magnetostriction, $\lambda$ , versus applied magnetic field and three regions of domain growth (I) and rotation (II, III). . . . .	13
2.4 Plot of normalized magnetization (left) and magnetostriction (right) versus applied magnetic field for a typical magnetostrictive material. .	14
2.5 Schematic illustrating the (a) unbiased moment alignment, (b) rotation of moments perpendicular to compressive stress, and (c) maximum 90 degree rotation for axially applied magnetic field . . . . .	16
2.6 Plot of magnetostriction versus applied field for Terfenol-D at five compressive loads: 0 ksi, 2.5 ksi, 4.5 ksi, 7.5 ksi, and 16 ksi. The trends illustrate the range of compressive pre-loads in which Terfenol-D has largest field-induced magnetostriction. . . . .	17
2.7 Plot of Terfenol-D Young's modulus at constant compressive stress values (6.9 - 103.5 with 6.9 MPa steps) for constant applied magnetic fields (0 - 193.2 kA/m with 16.1 kA/m steps). The trends illustrate the range of values that a magnetostrictive material's Young's modulus can take based on operating conditions [32]. . . . .	18

2.8	Magnetostrictive material applications: (a) Terfenol-D ultrasonic rotational motor, (b) ultrasonic transducer with exponential horn, (c) ring transducer for sonar and (d) Tonpilz transducer for sonar. . . . .	21
2.9	General architecture and operation of a smart material EHA. (a) The smart material extension forces high-pressure fluid into the high-pressure side of the hydraulic cylinder. (b) The retraction of the smart material and piston allows fluid to refill the chamber from the low-pressure side of the cylinder and the accumulator. . . . .	24
2.10	Three common operating conditions for smart material pump and EHA characterization: (a) no-flow condition where the outlet port of pump is closed, (b) blocked condition where hydraulic cylinder piston motion is held to zero and (c) no-load condition where the system actuates against zero load. . . . .	27
3.1	(a) Solid modeling illustrating the configuration of the Terfenol-D driver, diaphragm, piston, and chamber. (b) Two degree-of-freedom model representing the Terfenol-D pump in the mechanical domain. . . . .	33
3.2	(a) Solid model of the output hydraulic cylinder and piston for the actuator. (b) Single degree-of-freedom model representing the output piston and actuator load in the mechanical domain of the model. . . .	34
3.3	(a) Solid drawing of the reed valve with surrounding structure including entry and exit ports. (b) Single degree-of-freedom model representing the rectification reed valves (inlet and outlet) in the mechanical domain. . . .	35
3.4	(a) 3D model of reed valve with contact area used for FE simulation to determine valve stiffness. Static pressure is applied over the contact area to deflect the valve flap. The force ( $p \times A$ ) over the tip displacement is the modeled stiffness of the valve ( $k_r = 6650$ N/m). (b) The contact area is equal to the port area covered by the valve flap. . . .	37
3.5	Schematic illustration of the hydraulic circuit and mechanical inputs for the smart material EHA. The fluid domain is defined by four state pressures, lumped resistances and capacitances. Fluid-structural coupling in the fluid domain is modeled through the dependence of rectification valve resistances ( $R_1$ and $R_2$ ) on valve motion ( $x_{ro}$ and $x_{ri}$ ). . . .	47

3.6	(a) Schematic of outlet reed valve orientation in EHA pump head with inlet and outlet port shown. (b) Finite element model geometry for characterization of fluid-structure coupling in mechanical reed valves.	50
3.7	Finite element simulation results of fluid-structure interaction for the rectification reed valves in the smart material pump. The simulation uses a constant flow rate condition to determine the fluid resistance for the valve (R) as a function of the tip displacements (x) from 2 to 1012 $\mu\text{m}$ .	52
4.1	3D exploded, sectioned view of Terfenol-D pump.	67
4.2	3D exploded, sectioned view of Terfenol-D pump head.	68
4.3	(a) Schematic illustrating the two sources of pre-load for the Terfenol-D rod: the force from the bias pressure applied to the piston area ( $F_{bias}$ ) and the compression from the pre-load bolt ( $x_b$ ). (b) Lumped model showing the stiffness of the Terfenol-D rod and diaphragm with the applied force, piston, and base displacement.	69
4.4	Illustration of the steps involved in one pre-load increment for pre-conditioning the Terfenol-D rod. (a) Initial state of piston, diaphragm, and Terfenol-D rod before pre-load is applied. (b) Incremental pressure is applied ( $\Delta P$ ) to the hydraulic circuit compressing the Terfenol-D rod and diaphragm by pre-defined displacement ( $\Delta x_{max}$ ). (c) Pre-load bolt is adjusted by $\Delta x_{max}$ to return diaphragm to un-deflected state. After steps (a), (b), and (c) the Terfenol-D rod has been stress by an increment of $\sigma_{pre} = \Delta x_{max} E_Y^H / L_{td}$ .	70
4.5	(a) 3D illustration of the LK-G32 laser sensor head and internal receiving components (Li-CCD and lens unit). (b) Schematic illustrating the principle of operation for the emission and reception of the laser beam for measuring a moving target. The charge of the array is proportional to the light intensity and knowing the location of the high charge indicates the relative location of the target.	71
4.6	(a) Exploded 3D solid model of modified pump cap, acrylic insert, and outlet reed valve. (b) Cutaway 3D model of assembled modified pump cap and insert. Epoxy is used to seal the gap between the insert and the pocket of the pump cap.	71

4.7	Cutaway view of a solid model of the experimental setup for in situ outlet reed valve displacement measurement with the LK-G32 laser displacement sensor, modified pump cap, insert, outlet reed valve and pumping chamber shown. . . . .	72
4.8	Schematic of full setup for data acquisition from smart material pump. The setup has capability to measure: solenoid coil current, $I$ , and voltage, $V$ , Terfenol-D rod strain, $\epsilon_{td}$ , outlet pressure, $p_o$ , and inlet pressure, $p_i$ , piston acceleration, $\ddot{x}_p$ , and outlet rectification valve motion, $x_{ro}$ . . . . .	72
5.1	Measured and simulated no-flow pressure trace for the Terfenol-D pump at (a) 5 and (b) 10 Hz. The solenoid coil input is a 20 amp peak-to-peak current with a 10 amp bias. . . . .	75
5.2	Measured and simulated no-flow pressure trace for the Terfenol-D pump at (a) 25 and (b) 50 Hz used to validate the parameters of the rectification reed valve model and fluid-structure interaction. . . . .	76
5.3	Results of time domain tests and simulations for the Terfenol-D pump under no-flow conditions from 1 to 1200 Hz. The “ideal” results are for a system model simulation absent of valve dynamics. The metric for evaluation is the average amount of pressure stored at each frequency by the pump and is given in equation (5.1). . . . .	78
5.4	Simulation results for pumping frequencies from 10 - 3500 Hz for the Terfenol-D pump attached to a hydraulic cylinder and piston and loaded inertially to create actuation. The dynamic response of the rectification valves limit the ability of the pump to deliver fluid to the cylinder at frequencies above 1200 Hz and thus attenuates actuator motion. . . . .	82
5.5	Normalized data for piston induced flow rate ( $q_{pi} = A_{pi}\dot{x}_p$ ), flow rate through the outlet valve, valve motion, and valve resistance vs. percentage of pumping cycle at 1420 Hz. The resulting simulation highlights the effect of phase mismatch between the valve and piston motion causing actuator reversal shown as negative velocity in figure 5.4. . .	83

5.6	Simulation results for pumping frequencies from 10 - 3500 Hz for the Terfenol-D pump attached to a hydraulic cylinder and piston and loaded inertially to create actuation. The valve resonance is increased by a factor of 2.45 over the baseline values presented in Figure 5.4 resulting in actuator bandwidth expansion and a higher maximum velocity at actuator resonance. . . . .	84
5.7	Terfenol-D pump response under no-flow conditions at 10 Hz. (a) In situ displacement time trace for the outlet reed valve; (b) normalized outlet reed motion, Terfenol-D pump outlet pressure, and Terfenol-D strain at 10 Hz pumping frequency for 5 cycles. . . . .	89
5.8	Terfenol-D pump response under no-flow conditions at 20 Hz. (top) In situ displacement time trace for the outlet reed valve at 20 Hz pumping frequency for two measured cases of different input amplitude to the solenoid coil. (bottom) In situ outlet pressure traces showing different steady state values. . . . .	90
5.9	Terfenol-D pump response under no-flow conditions at 20 Hz. Normalized outlet valve motion, outlet pressure, and Terfenol-D strain at 20 Hz pumping frequency for 8 cycles. The outlet valve is responsive to the pressurizing stroke of the piston showing two regions of negative slope during piston retraction leading to pressure recoil and backflow. . . . .	91
5.10	Terfenol-D pump response under no-flow conditions at 100 Hz. (a) In situ displacement trace for the outlet reed valve (b) normalized outlet reed motion and solenoid current at 100 Hz for 5 cycles. . . . .	92
B.1	Test stand for Galfenol unimorph sample testing. . . . .	100
B.2	Results of free displacement testing for Galfenol samples: (a) 0.015/0.015" brass/Galfenol (b) 0.005/0.015" stainless steel/Galfenol (c) 0.06/0.015" aluminum/Galfenol. . . . .	102
B.3	Results of blocked force testing for Galfenol samples: (a) 0.015/0.015" brass/Galfenol (b) 0.06/0.015" aluminum/Galfenol. . . . .	103
C.1	Detailed drawing of acrylic insert "viewing window" for in situ valve characterization. . . . .	104
C.2	Detailed drawing of modified pump cap for in situ valve characterization. . . . .	105

# CHAPTER 1

## INTRODUCTION

Smart materials are utilized in numerous engineering applications including industrial processes, medical devices, automobiles, aerospace, energy harvesting, and damage detection. The unique ability of these high energy density materials to transfer energy between two different domains over a wide frequency range makes them well suited for a variety of applications. These materials could thus have a significant impact on sensitivity, bandwidth, and power density in devices and systems.

The general focus of this thesis is on modeling and characterization of a smart material electrohydrostatic actuator (EHA) and fluid rectification valves. A magnetostrictive material responding to a magnetic field input is used to drive the piston of a hydraulic pump. The high force vibrations of the Terfenol-D core displace small bursts of fluid through a rectification valve delivering a continuous flow of high-pressure fluid to the output hydraulic cylinder and piston. A full explanation of this process is discussed in section 2.5.1. The fluid rectification process, which converts the small bursts of fluid produced by the pump to continuous flow, is critical for this type of system. High frequency operation of the pump increases the flow rate capability and resonant operation, typically in the kHz range, increases the ratio of output pressure to input energy. Rectification valves that respond up to the resonance frequency of the

pump have the capability to significantly improve performance and dynamic range. The contribution of this work is to establish a fluid-structure coupled model for the rectification valves in a smart material pump. Additionally a novel method for in situ characterization of a pump is described and implemented. A model framework is established by integrating a mechanical model for the fluid rectification reed valves used in a Terfenol-D pump, described in section 4.1, into a system mechanical model describing the motion of the pump and actuator piston. Valve motion is coupled to the fluid domain through the driving pressure of the working fluid, fluid loading, and proximity effects. The resistance to flow provided by the valve during operation of the pump is coupled to the motion of the valve and establishes the reliance of the fluid domain on the mechanical domain for the valves in the system model. The thesis is organized as follows.

Chapter 2 covers background information on smart materials and devices. The objectives and motivation for this research are described. A brief overview of smart materials is presented along with details on magnetically activated smart materials (magnetostrictive materials) in section 2.3. Section 2.4 reviews smart material applications while focusing on magnetostrictive applications. The final section in chapter 2, 2.5, gives an in depth discussion on the principle of operation for smart material pumps. A literature review of smart material pumps is presented with a focus on pressure and flow rate performance.

The mechanical and fluid domains of the system model are described in chapter 3. A lumped parameter model accounts for the dynamics of the Terfenol-D pump, rectification reed valves, and output hydraulic cylinder in the mechanical domain using Newton's  $2^{nd}$  law to derive equations of motion. Conservation of flow along with

lumped fluid elements resistance and capacitance is used to develop dynamic, first order equations for state pressures at the chamber, accumulator, high, and low pressure sides of the hydraulic cylinder. A detailed description of the fluid-structure coupling for the rectification reed valves is presented in this chapter. The mechanical model is presented in section 3.1 and the fluid model in section 3.2. System model equations and parameters are summarized in section 3.3.

A measurement system used to experimentally characterize the Terfenol-D pump is detailed in chapter 4. The details of the Terfenol-D pump used in this study are given in section 4.1. Terfenol-D pre-load (mechanical bias) is an important parameter for optimum performance. Section 4.2.1 presents the method for mechanically biasing the Terfenol-D. The details of the novel method for in situ valve characterization are given in section 4.3. Section 4.4 provides a schematic of the measurement system with the Terfenol-D pump indicating the equipment used and some important details.

Chapter 5 presents simulation and experimental results for no-flow operation of the Terfenol-D pump to validate the fluid-structure coupling and mechanical model for the fluid rectification valves as defined in chapter 3. This method of validation considers the valve-specific parameters and also accounts for the dynamic effects of the Terfenol-D pump and chamber fluid. The system model is used to assess the effect of rectification valve dynamic response on the actuation capability of the Terfenol-D pump by simulating the case of inertial loading on a hydraulic cylinder and piston driven by the pump. The system simulation captures the dynamic fluid-structure coupling of the rectification valves and their effect on the pump's ability to deliver high pressure flow to the cylinder of the actuator. The results are compared to system model simulations with ideal valve behavior to illustrate the effect of valve dynamics.

Rectification valve resonance is increased to expand actuator velocity bandwidth and is described in section 5.2.2. The model simulations indicate the ability to expand actuator bandwidth, defined as the frequency range of positive actuator velocity, by increasing valve resonance. Test data for in situ outlet reed valve measurement acquired using the method described in chapter 4 is presented. The results validate the proposed method for measuring valve motion along with other system variable at frequencies below 100 Hz. The challenges of implementing this method are discussed in chapter 4. The results of system simulation and experimental characterization are discussed in chapter 5 while chapter 6 discusses the impact and contribution of this work along with recommendations for future work.

## CHAPTER 2

### BACKGROUND INFORMATION

#### 2.1 Motivation

The aerospace and automotive industries are high-impact areas for smart material applications. Smart material systems can improve packaging, enhance performance, and reduce weight in vehicle actuators and sensors. Increased flexibility in device packaging can allow actuators and sensors to be located in areas previously regarded as unattainable or impractical. Smart material systems can expand the dynamic range of conventional systems and improve maintainability. The high power density, fast dynamic response, and sensitivity of these materials have the potential to reduce weight and volume in comparison to conventional devices.

There is a trend in the automotive and aerospace industries toward systems that use electrical control between the user input and system output termed fly-by-wire. In addition to fly-by-wire control, these industries are interested in replacing traditional power supply mechanisms (hydraulic circuits or mechanical linkages) by electric wires in power-by-wire systems. Digital fly-by-wire systems have been used since the early 1970's in military aircraft and were introduced to commercial aircraft in 1988 through the Airbus A320 program [8]. The automotive industry began to implement

drive-by-wire (throttle-by-wire) technology in the mid 1990's and is currently working to implement other 'by-wire' systems [5]. The mechanical and hydraulic systems of an aircraft, for example, are heavy and require redundancy to achieve mandatory levels of safety. There is limited flexibility in routing mechanical linkages and hydraulic lines that convert a user input to mechanical output within a vehicle. By replacing mechanical and hydraulic power transmission components with electrical wire, power-by-wire technology addresses many of the short-comings of traditional systems. The electrical interface between the user and system allows integration with a digital controller which can improve overall vehicle performance by combining user inputs with sensor feedback and control. The first implementation of power-by-wire technology has been in backup actuation systems for Lockheed Martins' F-35 joint strike fighter (JSF) and Airbus' A380 airliner. Smart material actuation systems provide all the benefits of the power-by-wire systems with additional gains in response time and power-to-weight ratio. The U.S. government has recognized the importance of compact actuators as Defense Advanced Research Projects Agency (DARPA) has sponsored the Compact Hybrid Actuator Program (CHAP) which focuses on development of compact, efficient, high power density actuation devices that meet stroke, rate, bandwidth, and force outputs of emerging technologies.

Smart material electrohydrostatic actuators (EHAs) are electrically driven, closed loop hydraulic systems that provide linear actuation. A smart material core replaces the traditional electro-mechanical driver for the EHA which can improve dynamic response, system weight, and scalability. Hydraulic advantage and fluid rectification, which will be described in detail in section 2.5.1, are used to amplify the

high-force, small-displacement of the smart material driver into large-force and large-displacement motion. System weight can be reduced and packaging improved by taking advantage of the power-by-wire operation. The solid-state, smart material driver reduces the number of moving parts in the system.

## **2.2 Objectives**

This project builds upon the research conducted in the Smart Materials and Structures Lab at The Ohio State University by Dr. Marcelo Dapino, David Nosse, and Mike Rupinsky in the area of smart material actuators. The research is supported through the National Science Foundation (NSF) Industry & University Cooperative Research Program (I/UCRC) on Smart Vehicle Concepts [19]. The SVC center investigates smart material-based solutions to future vehicle requirements and develops adaptive vehicle components and systems with superior dynamic response and multifunctional operation.

This research follows a specific methodology to develop a compact actuator driven by a smart material that will meet performance and packaging needs of the aerospace and automobile industries. The high-force, low-displacement motion of the smart material is converted to high-force and displacement output through motion amplification using hydraulic fluid rectification. The principle of operation is described in detail in section 2.5.1. Through application of engineering principles an accurate dynamic model is developed which characterizes the behavior and performance of a smart material pump and actuator built in our lab. A firm understanding of the system through first principles exposes critical aspects of the design which become the focus of the modeling and testing effort. Extensive testing experience and dynamic

modeling can be used to design smart material actuation systems that deliver the performance demands of the industry.

## **2.3 Smart Materials**

### **2.3.1 Overview**

A material is defined as smart when it has the capability to convert energy between two domains. Smart materials may also be referred to as controllable, active, adaptive, intelligent, or metamorphic depending on the application and function [17]. Many of the physical phenomena that are at the heart of smart material behavior occur naturally. Quartz is a naturally occurring material that has the property of producing an electric field under pressure. This effect is called piezoelectricity (“pressure electricity”) and was discovered by Pierre and Jacques Curie in 1880 [17]. Iron, one of the few naturally occurring ferromagnetic materials, exhibits a change in shape due to change in magnetization. This property, called magnetostriction, was discovered in 1842 by James Joule [17]. While many of the properties that make a material smart exist naturally, advances in solid-state physics and material science have enabled the technology to exploit these properties in useful devices. In the short time since smart materials were first synthesized the scientific community has characterized the extraordinary and complex behavior of these materials and applied them to create useful smart devices and smart systems. A general definition of a smart system is an ensemble whose dynamics can be monitored or modified by distributed sensors and actuators to accommodate time-varying external inputs or a changing environment [46]. Many notable milestones have been reached, but we are only just discovering the practicality of this technology. Smart materials have great potential

to improve human life and several examples are presented at the conclusion of this section following a more detailed discussion of magnetic smart materials.

### **2.3.2 Magnetostrictive Materials**

Magnetostriction is defined as magnetic field induced strain. Magnetostrictive materials deform in response to a change in magnetic moments per unit volume [23]. All magnetic materials are magnetostrictive to some degree while materials containing rare earth elements can exhibit “giant” magnetostriction above 0.1%. Joule discovered the magnetostrictive effect in 1842 [17]. In 1865 Pasquale Villari discovered the inverse of the Joule phenomenon that an applied stress would change the magnetization in magnetostrictive materials [17]. The Joule effect is referred to as the actuation effect while the Villari effect is referred to as the sensing effect. The most established giant magnetostrictive material, Terfenol-D, was developed at the Naval Ordnance Laboratory in the 1960’s and is an alloy of iron and the rare earth elements terbium and dysprosium [17]. Rare earth alloys exhibit large magnetostriction at cryogenic temperatures and little to none at room temperature while Terfenol-D is capable of producing strains up to 1600 parts-per-million (ppm) at room temperature at magnetic fields near 2000 Oe [16]. The large strains produced at room temperature make Terfenol-D the most viable option for magnetostrictive systems; however, geometries are limited because the material is brittle. Developed in 1998, the magnetostrictive material Galfenol, an alloy of iron and gallium, addresses the brittleness of Terfenol-D as it is much easier to machine and is very robust [1]. Galfenol vastly expands the possible applications for magnetostrictive materials, but currently produces only around a quarter of the magnetostriction of Terfenol-D.

The process of magnetostriction begins with an understanding of magnetic materials and magnetic domains. Figure 2.1 shows a schematic of the atomic, domain, and bulk level of a general ferromagnetic material. It is well known that a charged particle in motion will create a magnetic field. At the atomic level, shown schematically in Figure 2.1(a), there is a net magnetic moment which is a combination of the moment caused by the motion of electrons about the nucleus and the spin of the electrons [23]. The transition metals, rare earths, and actinides are the only groups of elements in the periodic table that exhibit magnetic moments [23]. When these elements bond to form solids the ionic electron configuration leaves unbalanced electron populations in the inner shell which results in a net magnetic moment [23]. In all other elements the ionic bonding that makes up bulk material negates the effect of unbalanced electrons and thus results in no net magnetic moment [23]. A magnetic domain is defined as a volume within the bulk material that has uniform magnetization or equally aligned magnetic moments as shown in Figure 2.1(b). The bulk material, shown in Figure 2.1(c), is comprised of magnetic domains which align along several preferred directions if the material is unbiased mechanically and magnetically. The effect is a nearly zero net magnetic moment for the bulk material. The magnetostriction occurs due to the rotation of these magnetic domains. The magnetostrictive effect can occur from two phenomena: spontaneous (temperature-based) or field-induced [18]. The two effects are illustrated in Figure 2.2. In each case the formation and rotation of the magnetic domains change the inter-atomic spacing of the material resulting in shape change [17]. Ferromagnetic materials undergo a magnetic phase transition from a disordered and random paramagnetic state to an ordered ferromagnetic state when cooled through the Curie temperature [18]. During this cooling process magnetic

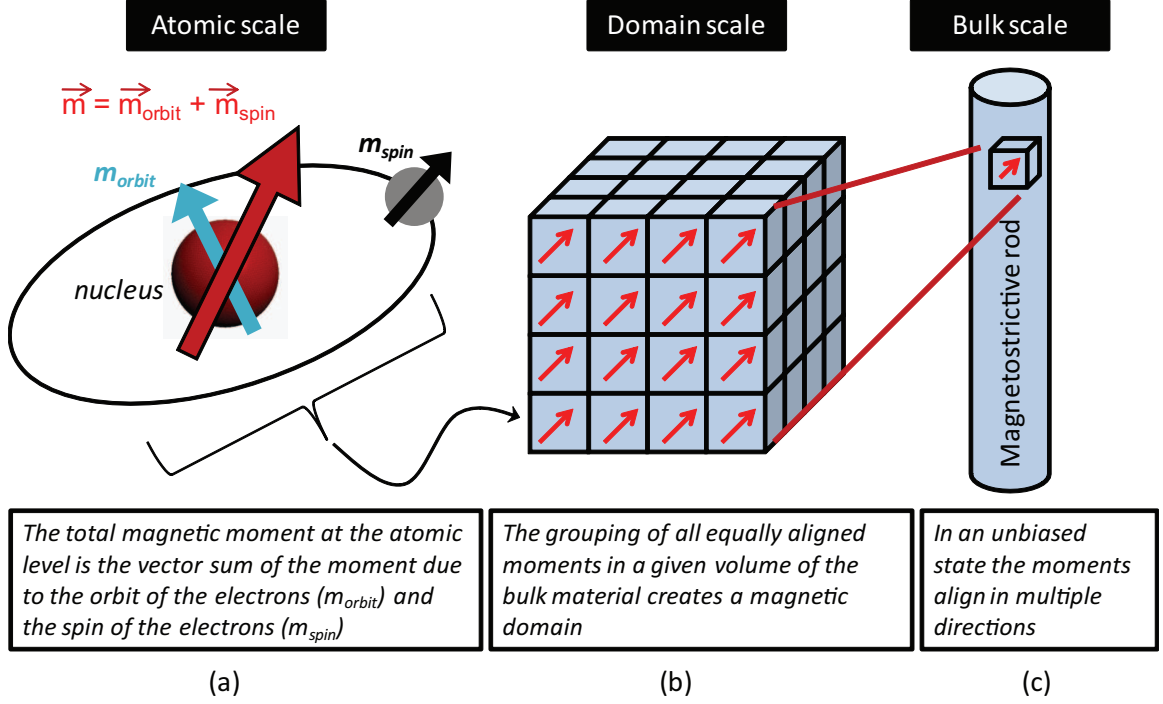


Figure 2.1: Illustration of the atomic contribution to magnetic moments and magnetic domains in a bulk magnetostrictive material.

moments align resulting in a spontaneous magnetization,  $M_s$ , leading to a spontaneous magnetostriction,  $\lambda_o$ , depicted in Figure 2.2(a) and (b) [18]. The spontaneous magnetostriction,  $\lambda_o$ , is approximately one third of the total magnetostriction,  $e$ . Figure 2.2(c) illustrates a large field-induced domain rotation where an applied magnetic field orients the magnetic domains in the direction of the field producing saturation magnetostriction,  $\lambda_s$ , where:

$$\lambda_s = \frac{2}{3}e. \quad (2.1)$$

Saturation magnetostriction is presented in more detail in Figure 2.3 considering a magnetostrictive rod. The magnetostrictive rod can be visualized as made up of

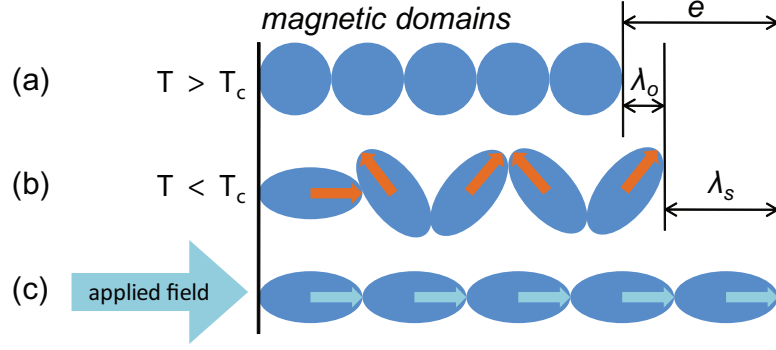


Figure 2.2: Illustration of (a) magnetic domains above Curie temperature (b) spontaneous magnetostriction and (c) field-induced magnetostriction.

sections of magnetic domains each with moments aligned in random directions for an isotropic material [7]. The result of this random orientation is zero net magnetization and the rod is termed demagnetized as shown in Figure 2.3(a). An increasing applied magnetic field along the length of the rod results in magnetostriction in three regions shown in Figure 2.3(b). Initially the rod is demagnetized and the magnetostriction lies at the origin of the magnetostriction versus applied field plot. As a low field is applied along the length of the rod, depicted in region I, domains aligned favorably with the applied field will grow at the expense of other domains in a nearly reversible process. Region II describes the behavior at moderate fields where magnetic domains aligned in unfavorable directions begin to rotate into energetically favorable directions close to the field direction, called easy axes [18]. The domain rotation in this region occurs suddenly and is the reason for the ‘burst’ of magnetostriction shown in Figure 2.3(b). As field increases into region III the rate of magnetic moment rotation slows until finally the entire rod becomes a single domain. At this point the rod has reached technical saturation magnetization with saturation magnetostriction,  $\lambda_s$ . Under very

large fields it is possible to increase beyond saturation magnetostriction into forced magnetostriction, but this effect is considered irrelevant for many applications due to the complication of applying the large fields.

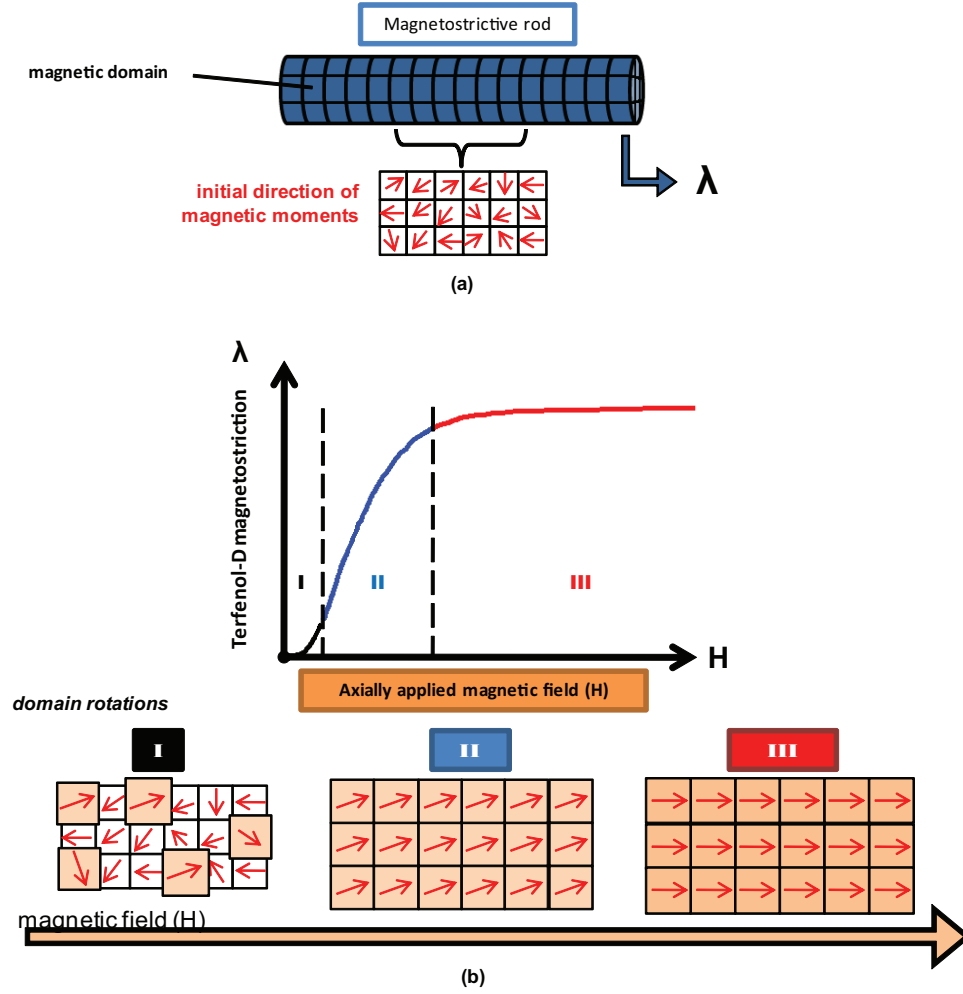


Figure 2.3: Schematic of (a) random orientation of moments for unbiased magnetostrictive rod and (b) simplified plot of magnetostriction,  $\lambda$ , versus applied magnetic field and three regions of domain growth (I) and rotation (II, III).

Typical magnetization and magnetostriction responses are shown in Figure 2.4. These response curves differ from the plot presented in Figure 2.3(b) in that they

illustrate the hysteretic nature of magnetostrictive materials. The domain wall motion at low fields is reversible, but as the amount of magnetic energy increases it will eventually exceed the pinning energy and the wall will dislocate from pinning sites. Pinning sites act like anchors for the domain walls and arise from crystal imperfections, stress concentrations, voids and cracks [18]. The energy lost to pinning is dissipated and is a source of hysteresis in the material. Therefore the nonlinear behavior of the material comes from two sources: the saturation behavior described in Figure 2.3 and the hysteretic behavior caused by the dissipation of energy as magnetic domains rotate between easy axes and domain walls translate across pinning sites.

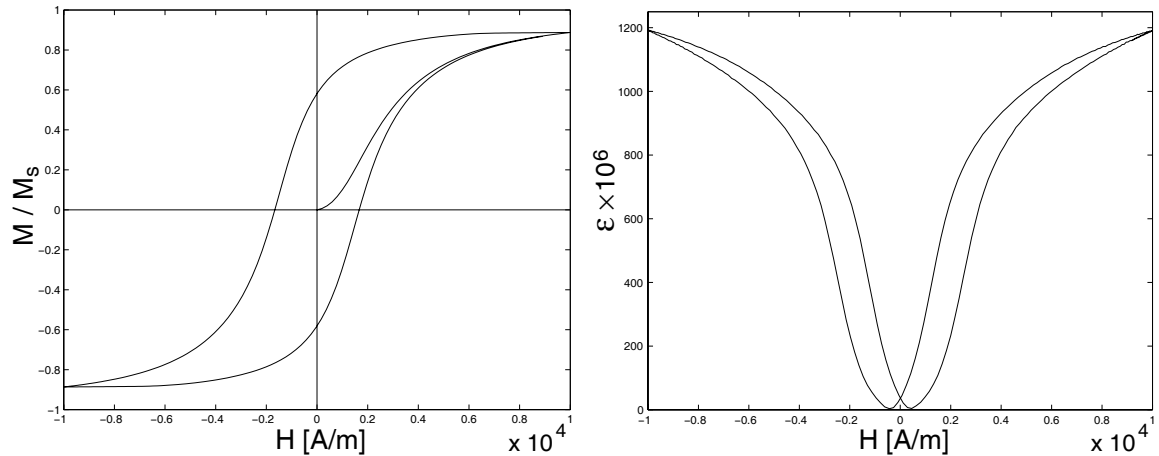


Figure 2.4: Plot of normalized magnetization (left) and magnetostriction (right) versus applied magnetic field for a typical magnetostrictive material.

The general description of domain rotation and magnetostriction presented in Figure 2.3 assumes the magnetostrictive material is initially unbiased magnetically and mechanically. In practice it is useful to bias the material mechanically, magnetically,

or both. Terfenol-D is twenty-five times stronger in compression than in tension and therefore in almost all applications the material requires a compressive pre-stress to ensure the magnetostriction does not place the material in tension. In addition to ensuring structural integrity, a compressive stress also pre-aligns magnetic moments in a favorable orientation. The compressive stress produces a significant decrease in the internal energy in a direction perpendicular to the stress. The magnetic domains will tend to align along this energetically favorable axis allowing a full 90 degree (maximum) rotation when a field is applied perpendicular to the pre-aligned moments. Figure 2.5 illustrates the effect of pre-stressing a magnetostrictive material and the 90 degree domain rotation to achieve maximum saturation magnetostriction. Physical limits of the force output of the material negate the domain rotation benefit at large pre-stresses. Figure 2.6 illustrates the range at which pre-compression is beneficial for Terfenol-D. The plot shows the full magnetostriction ‘butterfly’ for applied magnetic fields between  $-3000$  and  $3000$  Oe at four pre-stresses [1, 17, 31]. Saturation magnetostriction at zero pre-stress is below 700 ppm where it exceeds 1400 ppm at a pre-stress of 2.5 ksi, and falls near 500 ppm at 16 ksi. The magnetostriction plot shown in Figure 2.4(b) illustrates the behavior of the material to produce positive strain irrespective of the direction of the applied field. This characteristic can lead to frequency doubling when an applied harmonic field input that crosses the x-axis produces magnetostriction at a frequency twice the input. A magnetostrictive material may be magnetically biased to eliminate frequency doubling while still allowing bi-directional operation. Actuating the material around a magnetic bias point in the ‘burst’ region can reduce the hysteretic effects and improve sensitivity.

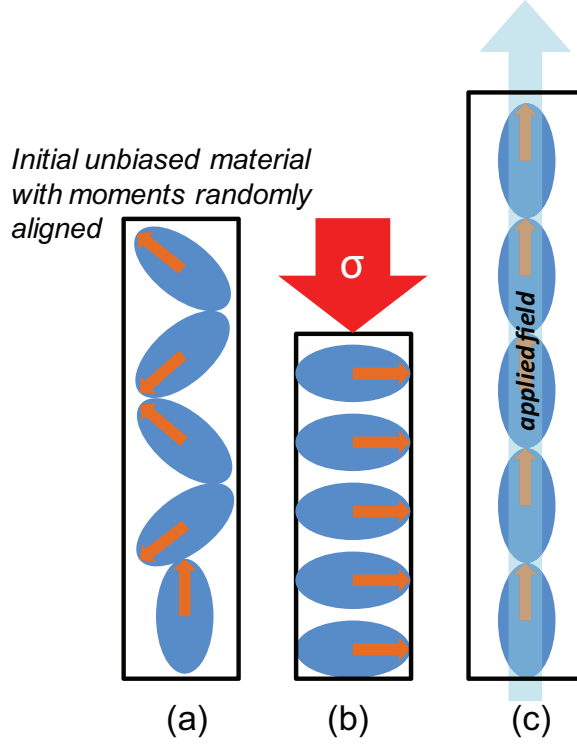


Figure 2.5: Schematic illustrating the (a) unbiased moment alignment, (b) rotation of moments perpendicular to compressive stress, and (c) maximum 90 degree rotation for axially applied magnetic field

The properties of most materials used in engineering applications are considered constant. As an example a particular type of steel may have an elastic modulus of 205 GPa for a range of stress up to yield at 310 MPa. For a designer this is a large range of stress to safely assume a constant modulus. Because smart materials possess the characteristic of converting energy between different domains they also have the mechanisms necessary to drastically vary their properties. The strong magnetoelastic coupling in magnetostrictive materials leads to large variation in elastic modulus called the  $\Delta E$  effect. There have been several studies on the  $\Delta E$  effect in magnetostrictive materials [14, 31]. Kellogg et al. studied the  $\Delta E$  effect of Terfenol-D in a

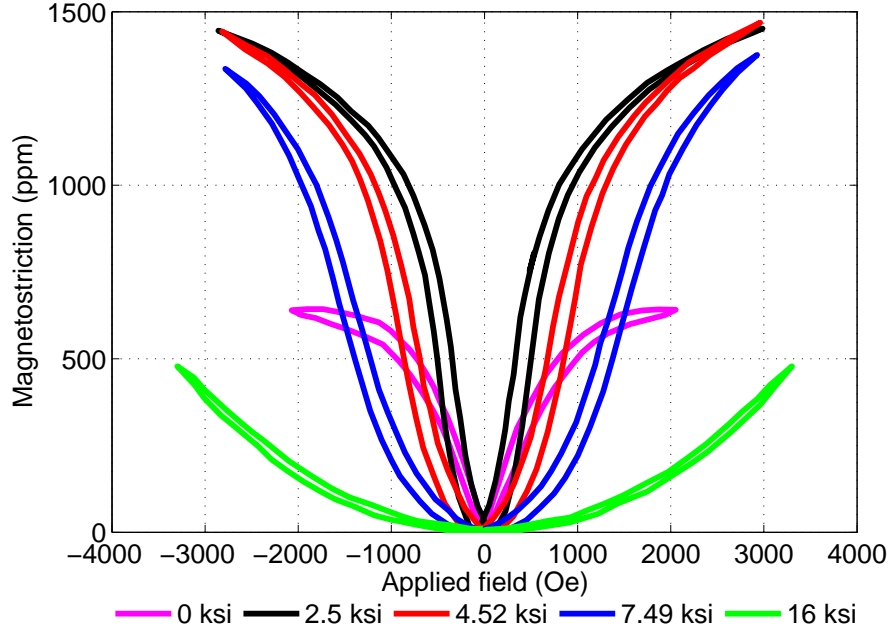


Figure 2.6: Plot of magnetostriction versus applied field for Terfenol-D at five compressive loads: 0 ksi, 2.5 ksi, 4.5 ksi, 7.5 ksi, and 16 ksi. The trends illustrate the range of compressive pre-loads in which Terfenol-D has largest field-induced magnetostriction.

transducer. The results of this study are presented in Figure 2.7 which illustrates the change in elastic modulus at DC magnetic bias fields up to 200 kA/m for constant compressive stresses ranging from 6.9 to 103.5 MPa. The circles provide the value of elastic modulus at a particular compressive stress and applied DC field and show the modulus can vary drastically from 115 GPa to 10 GPa. It is nearly impossible to maintain both a magnetic and mechanical bias during dynamic operation. Modeling of magnetostrictive materials within a dynamic system typically fixes the Young's modulus at a constant (or zero) bias field and is denoted by  $E_Y^H$ .

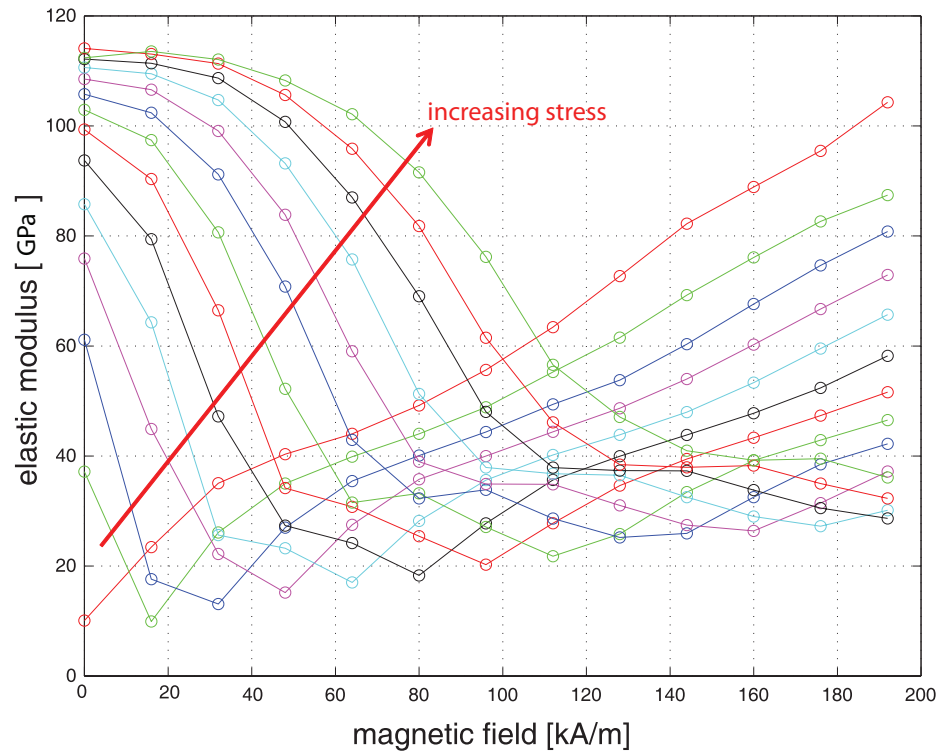


Figure 2.7: Plot of Terfenol-D Young's modulus at constant compressive stress values (6.9 - 103.5 with 6.9 MPa steps) for constant applied magnetic fields (0 - 193.2 kA/m with 16.1 kA/m steps). The trends illustrate the range of values that a magnetostrictive material's Young's modulus can take based on operating conditions [32].

## 2.4 Smart Material Applications

### 2.4.1 Overview

The unique characteristics of smart materials give them the potential to impact many areas of technology. The references presented in this section give several examples but in no way exhaust the large scope of smart material applications. In traditional technology smart materials have found uses in manufacturing processes, land and air vehicles and medical devices. Smith et al. developed an inverse compensation to control a Terfenol-D transducer in a high-speed milling application [47]. The high force, controllable output of the Terfenol-D transducer is well suited for high-speed out-of-round milling applications. Kalish and Henein investigated the use of piezoelectric actuators for diesel fuel injection [30]. Brei et al. reviewed the general use of smart materials in the automobile industry [4]. T. Lee and I. Chopra at the University of Maryland studied the use of piezoelectric devices for actuation of trailing edge flaps on a helicopter rotor [34]. Ahmadkhanlou et al. at Ohio State used magnetorheological fluid to design, build, and test a knee brace with controllable resistive torque for patient rehabilitation [2]. Smart materials also have applications in emerging areas such as nano-scale systems, structural health monitoring and energy harvesting. Smith et al. applied an inverse compensation methodology similar to that of the high-speed milling application for high-speed nano-positioning in atomic force microscopy [48]. Chang et al. reviewed smart material technology in damage detection and structural health monitoring and discussed the impact this technology has on civil infrastructure [9]. Smart materials have expanded the scope of energy harvesting systems. Sodano et al. reviewed power harvesting using piezoelectrics

discussing device architecture, efficiencies, and the future directions [50]. The application areas of smart material systems will continue to expand due to increase in demand for integrated structures and as high-volume use reduces manufacturing costs for certain materials.

## 2.4.2 Magnetostrictive Applications

Applications for magnetostrictive materials include: sonar, vibration control, pumps, exoskeleton telemanipulators, degassing in manufacturing processes, and ultrasonic cleaning [16]. Figure 2.8 illustrates several devices utilizing the most common magnetostrictive material, Terfenol-D. Two magnetostrictive *exciters* are used to create an elliptical tip motion driving the rotational motion of a shaft shown in Figure 2.8(a). The ultrasonic transducer illustrated in Figure 2.8(b) can be used in a number of applications (degassing, cleaning, welding, solid dispersion in liquid) where the underlying principles are cavitation effects, heat generation, mechanical effects, and chemical effects [18]. One of the original applications for magnetostrictives was in sonar transduction. Figure 2.8(c) and (d) show a ring transducer and a Tonpilz (inertial) transducer used for radiating sound waves. The ring transducer can generate dipole or quadrupole acoustic fields depending on the phasing of each ring section motion. In addition to the transducer applications presented here, magnetostrictive materials are also employed in deformation, position, torque and force sensors [16]. The applications of magnetostrictive materials have been extensive in the past years. As technology improves and demand for high performance, smart sensors and actuators increases, these materials will see expansion and growth in applications that will have a large influence in emerging technology.

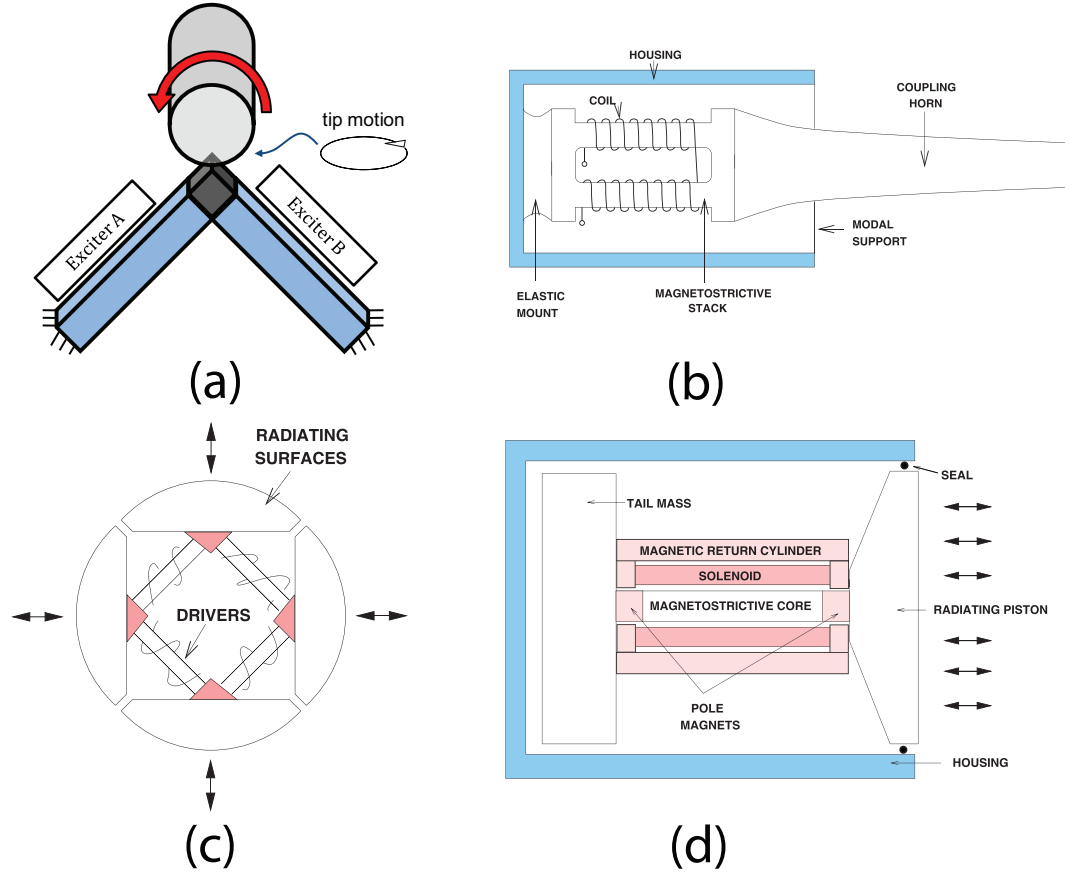


Figure 2.8: Magnetostrictive material applications: (a) Terfenol-D ultrasonic rotational motor, (b) ultrasonic transducer with exponential horn, (c) ring transducer for sonar and (d) Tonpilz transducer for sonar.

## 2.5 Smart Material Pumps and EHAs

Magnetostrictive and piezoelectric smart materials present an interesting challenge when used as drivers in hydraulic pumps and actuators. Piezoelectric materials have similar characteristics to magnetostrictive (i.e., high-force, low-displacement, solid-state motion) but are coupled through the electrical and mechanical domains. Other differences between these two materials will be presented throughout this section. The challenge of using these materials is creating large stroke actuation from the

low strain output of the material. Magnetostrictives can reach strains up to 0.16% and piezoelectrics around 0.1%. The method most commonly used to convert the low strain output of the smart material driver to large actuator stroke and force is hydraulic advantage. These pumps work on the principle of displacing small pulses of high-pressure fluid at a high frequency creating high-pressure, large-volume flow. While all the benefits of power-by-wire systems discussed in section 2.1 apply to these devices, their unique characteristics present an exciting engineering design challenge. The remainder of this section will describe the operational principles of smart material EHAs, present performance metrics and the progress in the area of smart material pumps and actuators.

### 2.5.1 Principle of Operation

A schematic illustrating the general architecture of a typical smart material electrohydrostatic actuator and the two steps necessary for operation are shown in Figure 2.9(a) and (b). The system includes a smart material driver along with an element to convert electrical input to the required energy to drive the material. Either tubing (not shown) or a manifold will house either unidirectional (not shown) or bi-directional valves and connect to an output hydraulic cylinder and piston. Fluid accumulators can be placed on either the high-pressure, low-pressure, or both sides of the hydraulic circuit. The actuator's pump is driven by a smart material which exhibits a mechanical response to an external stimulus. This research uses a Terfenol-D driven pump which responds to an applied magnetic field. **Fluid rectification** is defined as the process of converting the small fluid pulses from the smart material pump into continuous fluid flow. This process is critical for delivering continuous, high-pressure

fluid flow from the pump to the hydraulic cylinder. Fluid rectification can generally be described in two steps which happen concurrently with the overall operation of the smart material EHA. The state of the rectification valves is shown along with each system schematic in Figure 2.9(a) and (b) to illustrate the rectification process. In the first step, smart material extension shown in Figure 2.9(a), a positive strain is induced in the smart material driver which pushes a piston into a small, fluid-filled chamber. The fluid compression increases the pressure and induces a pressure differential in the preferred direction of fluid flow through the outlet rectification valve. As the state of the outlet rectification valve moves from closed to open, fluid flows through the outlet port, manifold, and directional valve to the high-pressure side of the output hydraulic cylinder. The high-pressure fluid pushes against the piston in the hydraulic cylinder creating actuation. The fluid refill stage of operation begins as the piston and smart material retract as shown in Figure 2.9(b). The expansion of the chamber volume causes the chamber pressure to drop which leads to a pressure differential in the non-preferred direction of the outlet valve. The pressure differential pulls the valve closed at the same time that the inlet valve, oriented in the opposing direction, opens allowing fluid to refill the chamber from the low-pressure side of the hydraulic cylinder and the accumulator. Each cycle of the pump pushes one pulse of fluid through the outlet valve. This process occurs at a rate referred to as the **pumping frequency**. The smart material pump will exhibit resonance typically in the kHz range. Ideally the pump should run at resonance to improve the pressure and flow rate output per input electrical power.

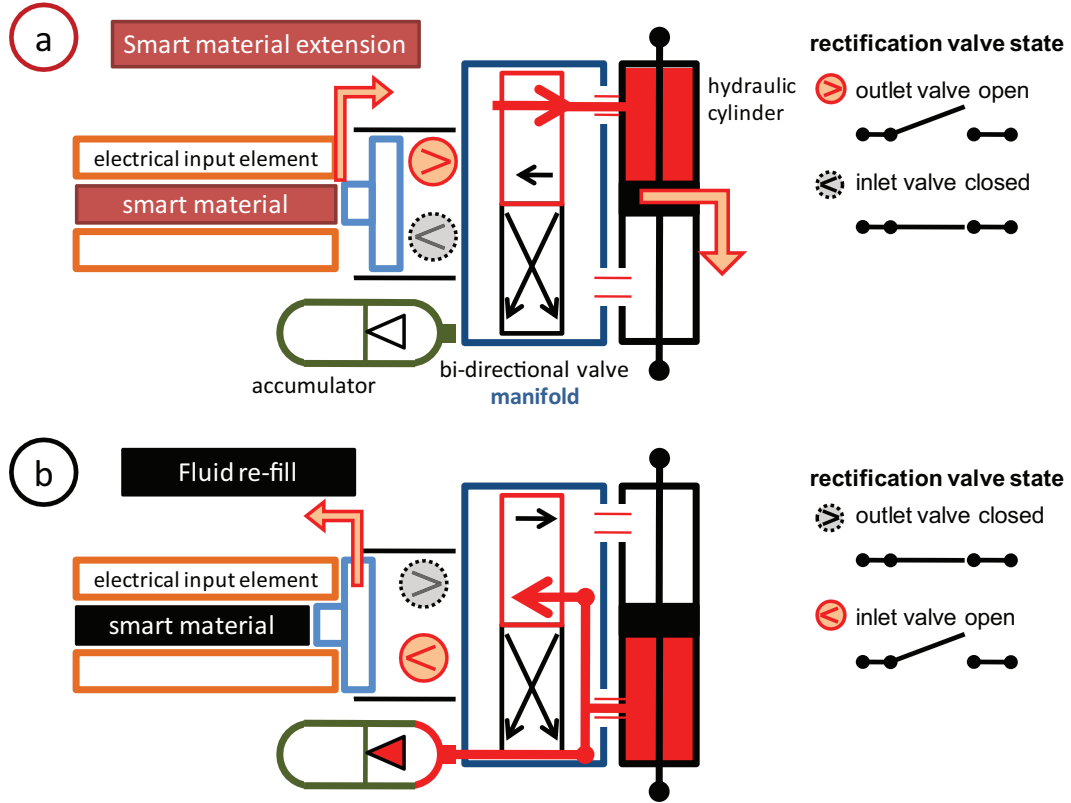


Figure 2.9: General architecture and operation of a smart material EHA. (a) The smart material extension forces high-pressure fluid into the high-pressure side of the hydraulic cylinder. (b) The retraction of the smart material and piston allows fluid to refill the chamber from the low-pressure side of the cylinder and the accumulator.

### 2.5.2 Performance Characterization

Before comparing the performance of recently developed smart material pumps it is necessary to discuss the parameters for performance characterization. Compact actuation is the most common application for smart material pumps presented in the literature. This application requires a hydraulic cylinder be attached to the pump so the pressure and flow rate of the pump can be converted to force and velocity. The

typical performance metrics of hydraulic pumps, pressure and flow rate, are characterized by force and displacement (or velocity) for the actuator system. In this section, examples of smart material pumps and EHAs are generally characterized using two methods: no-flow (blocked) pressure and no-load flow rate. Figure 2.10 illustrates the three commonly used methods for characterizing the maximum pressure, force, or velocity of a smart material pump or EHA. The no-flow condition, shown in Figure 2.10(a), characterizes the maximum pressure performance of the smart material pump. The pump is allowed to run with the outlet port of the hydraulic circuit blocked until there is no fluid flow from the chamber. The pressure generated in this condition is the maximum pressure the pump is able to produce. Figure 2.10(b) illustrates the blocked condition, which characterizes the maximum force of the EHA. Mass suspended such that the EHA is working against its gravitational acceleration is incrementally increased until there is no motion of the output hydraulic cylinder piston. The force applied by the suspended mass that results in zero output motion characterizes the maximum force the EHA can produce. Characterization using this method includes the losses associated with the hydraulic circuit and output cylinder where the no-flow condition does not. The maximum force the actuator can produce can also be characterized using a force sensor located at the rigid boundary of the output piston. Both characterization methods are described in the literature. In all applicable cases the blocked force, found using blocked conditions, will be converted to a blocked pressure by dividing the force by the piston contact area of the output cylinder. While this gives a consistent metric for pump comparison, it is not strictly equivalent because of the losses in the circuit and cylinder. The maximum pressure results that are converted to equivalent pressure will be denoted with an asterisk (\*).

Figure 2.10(c) illustrates the no-load condition for EHA performance characterization. This condition characterizes the smart material pump and EHA's ability to produce flow rate and output velocity. The pump is allowed to run when no load is attached to the piston of the output cylinder. The velocity produced at the actuator output can be converted to flow rate by multiplying by the contact area of the output piston. The results presented in this section will be formulated in this way unless stated otherwise.

### 2.5.3 Literature Review

Konishi et al. developed one of the first reported piezoelectric actuators capable of 34 W of power output at 300 Hz [33]. The piezopump concept has existed since the mid 1960's [52]. Some of the earliest published work on magnetostrictive pumps was by Gerver et al. who developed a Terfenol-D water pump capable of producing 1.83 in<sup>3</sup>/s of flow rate and a pressure of 5 psi [24]. A patent filed in 1986, entitled *Magnetostrictive Pump*, by Cusak had the stated objective: "to produce a hydraulic pump capable of producing a pressure based on the magnetostrictive effect" [15]. Due to the great progress of piezoelectric and magnetostrictive materials, improvements in power electronics and an increasing demand for high density actuation systems, smart material pump development has grown particularly in the last ten years. M. Rupinsky and M. Dapino developed a Terfenol-D pump capable of producing 1100 psi of no-flow pressure and 0.28 in<sup>3</sup>/s no-load flow rate [41]. Maximum pressure occurs at a pumping frequency of 10 Hz and maximum flow rate at 165 Hz. A high friction hydraulic cylinder limited the actuation capability above

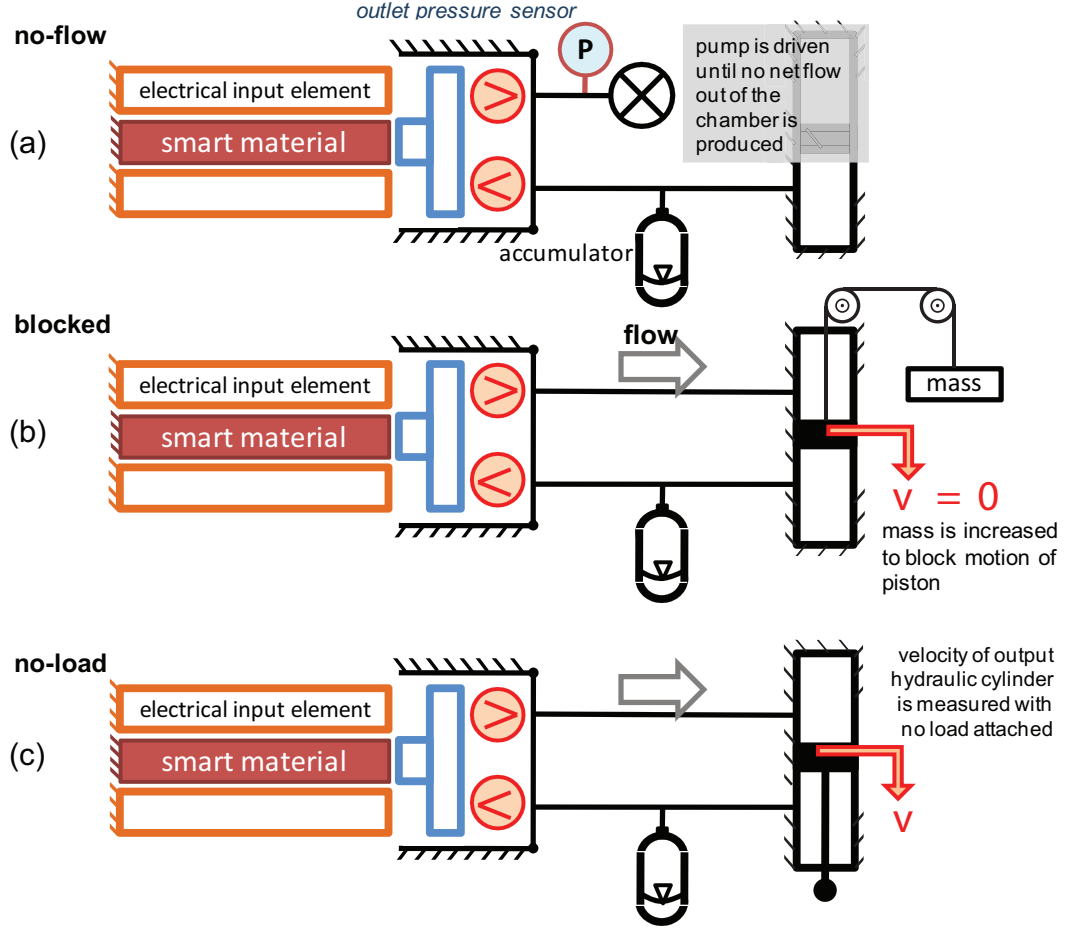


Figure 2.10: Three common operating conditions for smart material pump and EHA characterization: (a) no-flow condition where the outlet port of pump is closed, (b) blocked condition where hydraulic cylinder piston motion is held to zero and (c) no-load condition where the system actuates against zero load.

165 Hz. A state-space time-domain model and frequency-domain model developed using electroacoustic theory accurately predicted system dynamic response and no-flow pressure of the Terfenol-D pump. Nosse and Dapino also developed a novel magnetorheological (MR) rectification valve for a Terfenol-D pump capable of 0.25 in<sup>3</sup>/s of flow rate and 6 inches of stroke at 0.5 Hz [37, 38]. The University of Maryland has developed several piezoelectric and magnetostrictive pumps over the past several

years [11, 12, 13, 21, 22, 26, 27, 28, 29, 43, 44, 45, 53, 54]. John et al. compared the performance of a piezoelectric, electrostrictive, and magnetostrictive pumps using driving elements of similar size [28]. The electrostrictive (PMN) and magnetostrictive (Terfenol-D) performed at a similar level producing 87 psi\* and 66 psi\* of blocked pressure and 1.6 in<sup>3</sup>/s\* and 1.48 in<sup>3</sup>/s\* of no-load flow rate, respectively. John et al. also developed a bi-directional actuation system utilizing a Terfenol-D pump and MR valves configured in a wheat-stone bridge [27]. The bi-directional system is capable of actuating a 15 lb. load at a frequency of 3 Hz and stroke of 0.3 inches at a pumping frequency of 100 Hz. The paper also presents a lumped parameter model using a pressure-based rectification valve model. To this author's knowledge this is the most advanced implementation of a bi-directional smart material EHA presented in the literature. The paper by John et al. contains links to online video of the bi-directional testing. Keller et al. developed a relatively lighter PZT pump (82 grams) capable of 600 psi of no-flow pressure and 0.05 in<sup>3</sup>/s of no-load flow rate [10]. Mauck and Lynch developed a piezoelectric pump capable of 500 psi of no-flow pressure with a no-load flow rate of 0.31 in<sup>3</sup>/s when the pumping frequency was limited to 60 Hz due to heating of the stack [35]. Bridger et al. used linear network analysis software, 3D finite element software, and two design iterations to develop a Tonpilz (inertial-based) pump capable of producing 3000 psi [6]. The pump's chamber pressure was measured via a transducer mounted in the chamber. This differs from the more common method of using the blocked condition described in Figure 2.10(b). Eliminating the external losses through utilizing this method means the characterization of the pump is more isolated; however a drop in maximum pressure would be expected for the pump connected to a hydraulic circuit and cylinder. The work done by Bridger

et al. tested the pump at the highest pumping frequencies (2.4 kHz) seen in literature to date for meso-scale magnetostrictive pumps. Through DARPA's Compact Hybrid Actuator Program (CHAP), Sneed et al. developed a Terfenol-D pump capable of producing 1800 psi of no-flow pressure and 1 in<sup>3</sup>/s\* of flow rate at a pumping frequency of 200 Hz [49]. A series and parallel combination of the pump was successfully tested and results were consistent with the expectation of doubling the pressure (series) and the flow rate (parallel), respectively. For pressure measured across the output hydraulic cylinder this is the largest pressure differential currently reported in the literature. The pump was being developed to actuate a morphing wing for an autonomous vehicle but had not yet been tested in the loop.

## CHAPTER 3

### MODELING

A smart material EHA is comprised of subsystems in the fluid, mechanical, electrical, and magnetic domains. Lumped parameter modeling is well suited for multi-domain modeling and has been used extensively throughout the literature [11, 25]. A dynamic system model describing the relationship between electrical, mechanical, and fluid domains is presented here. Particular attention is paid to the fluid-structure coupling of the rectification valves. **Fluid-structure coupling** is defined as the relationship between mechanical motion of the rectification valve and its effect on the fluid domain and is a critical process in smart material pumps and actuation systems. A well-defined model, which incorporates fluid-structure coupling, captures the important high frequency behavior of the Terfenol-D pump and rectification valves. Capturing the effect of fluid-structure coupling in the system model expands the capability of model-based design. Through determining the optimum parameters to increase rectification valve frequency response, the bandwidth of the system can be tuned to the optimum point. Operating the smart material pump at resonance, which typically occurs in the kHz range, increases pressure and flow rate per input power.

## 3.1 Mechanical Model

### 3.1.1 Terfenol-D Pump

Figure 3.1(a) shows a cutaway solid model of the major mechanical components of the Terfenol-D pump highlighting the details used in the mechanical model. Figure 3.1(b) shows the two degree-of-freedom model for the Terfenol-D pump in the mechanical domain. The model accounts for the fluid loading and coupling through the mass of the fluid in the chamber,  $m_f$ , and the force of the chamber pressure on the cross sectional area of the piston,  $F_{fl} = p_{ch}A_{pi}$ . The fluid mass is assumed to translate in only one direction as it is fixed within the walls of the chamber. The Terfenol-D rod applies a force,  $F_{td}$ , which under the assumption of low-signal input current  $I$  has the form [42]:

$$F_{td} = Nqk_{td}I, \quad (3.1)$$

where  $N$  is the total number of turns in the solenoid coil,  $q$  is the piezomagnetic coupling coefficient, and  $k_{td}$  is the stiffness of the Terfenol-D rod given by [42]:

$$k_{td} = \frac{E_Y^H A_{td}}{L_{td}}, \quad (3.2)$$

where  $E_Y^H$  is the Young's modulus at constant magnetic field, and  $A_{td}$  and  $L_{td}$  are the cross-sectional area and length of the Terfenol-D rod, respectively. The Terfenol-D core acts as a pushrod on the pump piston and diaphragm. The dynamic mass of the Terfenol-D rod,  $\tilde{m}_{td} = \frac{1}{3}m_{td}$ , is lumped with the mass of the piston and diaphragm and is represented by effective mass,  $m_{eff}$ . The constant fluid mass is a function of the initial chamber volume,  $V_c$ , and the fluid density,  $\rho_f$ , by:

$$m_f = V_c * \rho_f, \quad (3.3)$$

The fluid stiffness is a function of the bulk modulus,  $\beta_{eff}$ , chamber height,  $h_{ch}$ , and the chamber's cross sectional area,  $A_{pi}$  by:

$$k_f = \frac{\beta_{eff} A_{pi}}{h_{ch}}. \quad (3.4)$$

The effective bulk modulus of the fluid is an important parameter for system performance and is discussed in more detail in section 3.2.1. The stiffness of the Terfenol-D rod and the sealing diaphragm are in parallel, hence combined stiffness is:

$$k_{eff} = k_{td} + k_d. \quad (3.5)$$

The damping constants,  $b_{eff}$  and  $b_f$ , are determined using dynamic simulations and account for the bulk dissipation effects within the smart material pump [42]. The equations of motion for the effective transducer mass,  $m_{eff}$ , and fluid mass,  $m_f$ , are solved using Newton's method and given by:

$$m_{eff}\ddot{x}_p + (b_f + b_{eff})\dot{x}_p - b_f\dot{x}_f + (k_{eff} + k_f)x_p - k_fx_f = Nqk_{td}I, \quad (3.6)$$

$$m_f\ddot{x}_f - b_f\dot{x}_p + b_f\dot{x}_f - k_fx_p + k_fx_f = p_{ch}A_{pi}. \quad (3.7)$$

### 3.1.2 Hydraulic Cylinder and Piston

The hydraulic cylinder, shown in Figure 3.2(a), houses two volumes of fluid on the 'high' and 'low' pressure sides of the output piston. The high-pressure,  $p_h$ , produced by the Terfenol-D pump acts on the piston area,  $A_{po}$ , to create linear actuation,  $x_{act}$ . The low-pressure,  $p_l$ , acts on the piston and opposes positive displacement. Figure 3.2(b) shows the single degree-of-freedom model for the actuator output piston and load. The mass of the piston and actuator load, typically attached to the free

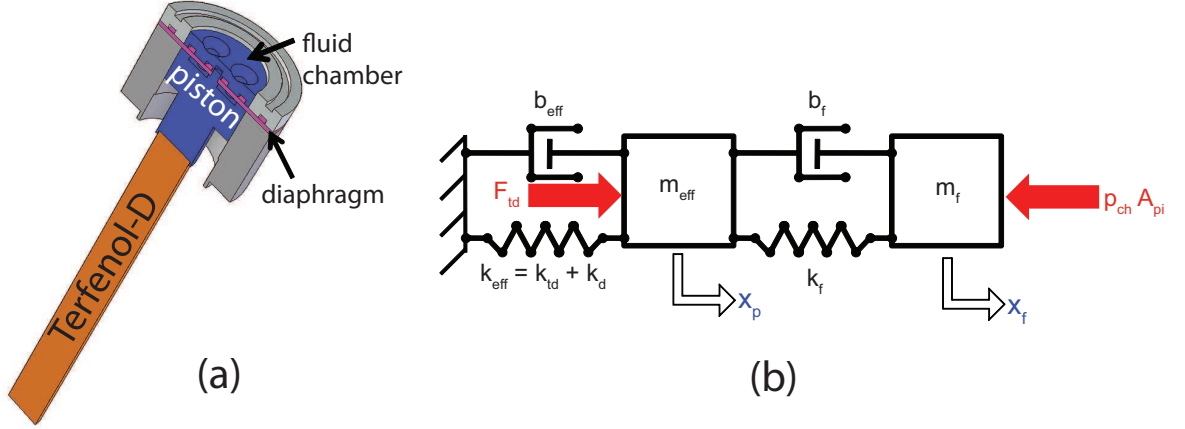


Figure 3.1: (a) Solid modeling illustrating the configuration of the Terfenol-D driver, diaphragm, piston, and chamber. (b) Two degree-of-freedom model representing the Terfenol-D pump in the mechanical domain.

end of the piston, are lumped into a single mass,  $m_l$ , based on the assumption that the piston shaft is rigid. In the simplest case the actuator load is purely inertial, represented by mass,  $m_l$ . The mechanical model shown in Figure 3.2(b) is a general mass-spring-damper system where the dissipation in the load is accounted for by damping term,  $b_l$ , and stiffness by,  $k_l$ . In practice, different types of loading can be used to characterize the actuator. A general case is presented here. The equation of motion for the general case presented here, from Newton's method, is:

$$m_l \ddot{x}_{act} + b_l \dot{x}_{act} + k_l x_{act} = (p_h - p_l) A_{po}. \quad (3.8)$$

### 3.1.3 Rectification Reed Valves

Figure 3.3(a) shows a solid model of the outlet reed valves used for fluid rectification installed in the smart material pump. Both the inlet and outlet reed valves

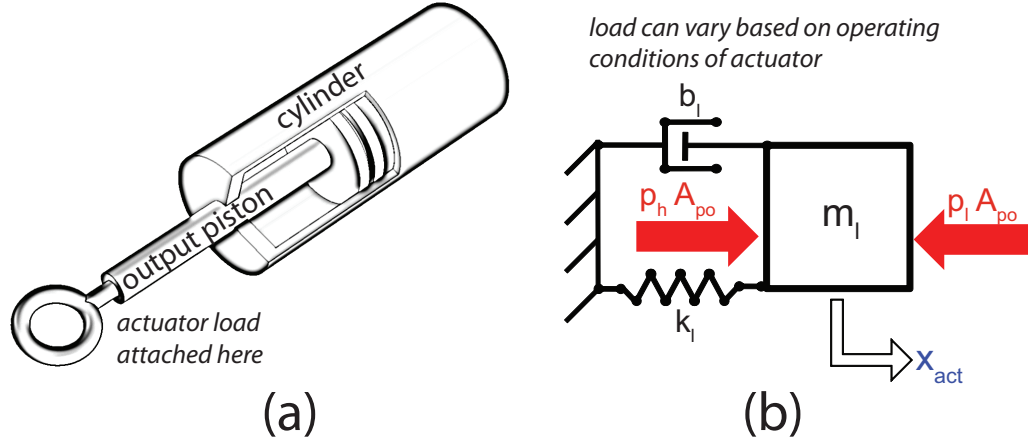


Figure 3.2: (a) Solid model of the output hydraulic cylinder and piston for the actuator. (b) Single degree-of-freedom model representing the output piston and actuator load in the mechanical domain of the model.

are represented by single degree-of-freedom mass-spring-damper models in the mechanical domain. Figure 3.3(b) illustrates the general mechanical model for the reed valves. In the mechanical domain the fluid-structure coupling for the reed valves is characterized in two ways: (1) the upstream,  $p_u$ , and downstream,  $p_d$ , pressures drive the motion of the valve as shown in Figure 3.3(b) and (2) the surrounding fluid and structure add equivalent damping and mass to the model. The mass and damping values are represented by  $\bar{m}_r$  and  $\bar{b}_r$ , respectively, and account for the fluid and structural effects. The directional notation for the upstream and downstream pressures refers to the preferred flow direction for each rectification valve. The valve motion,  $x_r$ , is modeled as the displacement of the tip indicated in Figure 3.3(a). A complete mechanical model for the reed valve is presented including the definition of valve stiffness,  $k_r$ , characterization of the effective mass and damping,  $\bar{m}_r$  and  $\bar{b}_r$ , and the loading due to fluid pressure. Using Newton's method of force balance the equations

of motion for the outlet and inlet rectification reed valves are:

$$\bar{m}_r \ddot{x}_{ro} + \bar{b}_r \dot{x}_{ro} + k_r x_{ro} = (p_{ch} - p_o) A_r \quad (3.9)$$

$$\bar{m}_r \ddot{x}_{ri} + \bar{b}_r \dot{x}_{ri} + k_r x_{ri} = (p_i - p_{ch}) A_r \quad (3.10)$$

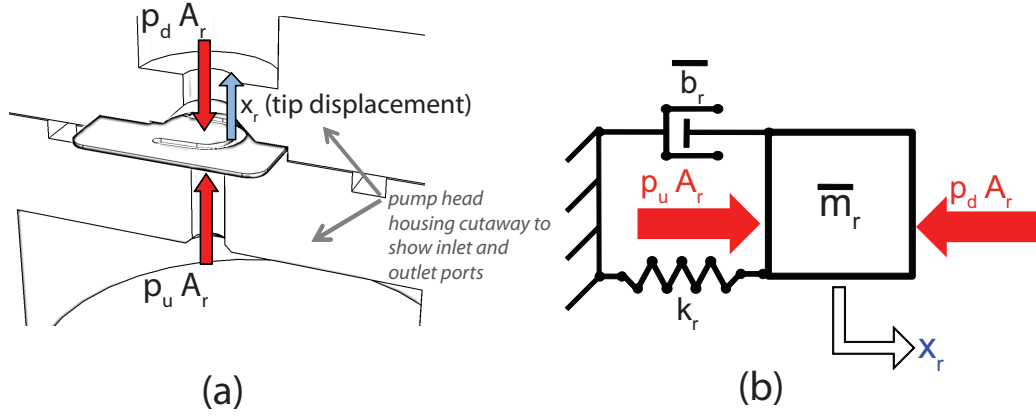


Figure 3.3: (a) Solid drawing of the reed valve with surrounding structure including entry and exit ports. (b) Single degree-of-freedom model representing the rectification reed valves (inlet and outlet) in the mechanical domain.

### Reed Valve Stiffness

As the chamber pressure increases during the positive displacement of the pump's piston, the pressure differential opens the outlet rectification reed valve in the preferred direction of flow. Similarly the pressure differential induced when the piston retracts and chamber pressure drops below the system bias pressure opens the inlet rectification valve. The reed valves are clamped between the halves of the pump head, which constrains the valve as a cantilever. The cantilever support of the valve means

the valve will deflect primarily in bending. The details of the reed-type rectification valves used in this study are summarized in Table 3.1.

<b>material</b>	304 stainless steel
<b>Young's modulus</b>	200 GPa
<b>density</b>	8000 kg/m <sup>3</sup>
<b>thickness</b>	0.005 in

Table 3.1: Summary of rectification reed valve properties.

A static, 3D finite element (FE) analysis using the structural mechanics module of the FE package COMSOL is used to determine the valve bending stiffness. In the simulation, pressures from 12.7 kPa - 12.7 MPa are applied in the out-of-plane direction on an area the size of the port the valve flap covers. The port has a diameter of 0.125 in and the corresponding area is 0.003068 in<sup>2</sup> (7.9 mm<sup>2</sup>). Figure 3.4(a) shows the contact area used in the FE analysis to determine valve stiffness. Stiffness is determined by taking force applied to the valve flap ( $p \times A$ ) over the tip deflection of the modeled reed. The 3D geometry used in the simulation is given in Figure 3.4(b). The results for four static cases are averaged to determine a valve stiffness,  $k_r = 6650 \text{ N/m}$ .

### Reed Valve Mass and Damping

While the valve stiffness can be determined rather simply from FE simulations, reed mass,  $\bar{m}_r$ , and damping,  $\bar{b}_r$ , are more difficult to quantify due to the dynamics of the surrounding fluid and the interaction with the surrounding structure. Considering the single degree of freedom model in Figure 3.3 oscillating in a fluid harmonically so

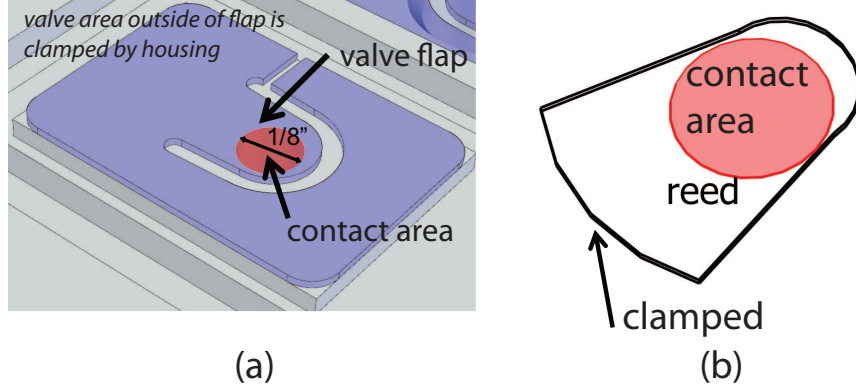


Figure 3.4: (a) 3D model of reed valve with contact area used for FE simulation to determine valve stiffness. Static pressure is applied over the contact area to deflect the valve flap. The force ( $p \times A$ ) over the tip displacement is the modeled stiffness of the valve ( $k_r = 6650 \text{ N/m}$ ). (b) The contact area is equal to the port area covered by the valve flap.

that the motion is described as:

$$x_r(t) = X_r \sin(\omega t), \quad (3.11)$$

the time derivatives of the displacement equation, velocity and acceleration, are:

$$v_r(t) = X_r \omega \cos(\omega t), \quad (3.12)$$

$$a_r(t) = -X_r \omega^2 \sin(\omega t). \quad (3.13)$$

Ignoring the higher harmonic terms, the motion will produce an oscillating force from the surrounding fluid which can generally be described as [3]:

$$F = a_1 \sin(\omega t) + b_1 \cos(\omega t). \quad (3.14)$$

Comparing equation (3.14) with equations (3.12) and (3.13) it can be seen that the force can be rewritten as:

$$F = -Aa_r(t) - Bv_r(t). \quad (3.15)$$

where,

$$A = \frac{a_1}{X_r\omega^2}, \text{ and} \quad (3.16)$$

$$B = \frac{-b_1}{X_r\omega}. \quad (3.17)$$

Based on Newton's laws the equation of motion for the forced mechanical oscillator can be written as:

$$m_r a_r(t) + b_r v_r(t) + k_r x_r(t) = F. \quad (3.18)$$

Combining equations (3.12), (3.13), and (3.14) with (3.18) gives:

$$(m_r + A)a_r(t) + (b_r + B)v_r(t) + k_r x_r(t) = 0. \quad (3.19)$$

Based on this equation of free motion and the terms  $m_r + A$  and  $b_r + B$  it is concluded that the effect of the surrounding fluid is to add effective mass and damping to the structure. The analytical added mass of the cantilever plate in the first mode of vibration is:

$$\tilde{m}_r = \frac{\pi}{4} \rho_f a b^2 [3], \quad (3.20)$$

where  $a$  and  $b$  are the length and width of the cantilever beam, respectively, and  $\rho_f$  is the density of the surrounding fluid.

In addition to analytical treatment, experimental evaluation can aid in quantifying the complex interactions that cause a structure to respond differently in a highly viscous medium. Naik et al. [36] presented a study on the response of a cantilever beam submerged in a fluid and near a solid structure. The study measured the

broadband amplitude response of a piezoelectric bimorph submerged in several fluids. The bimorph was actuated using a function generator and an electrical connection through the base of the beam. Additionally the study quantified the effect of a solid structure near the bottom surface of the beam. While not identical to the reed valve and port used in the EHA, the study quantifies the same physical phenomena that affect frequency response in a similar system. Pressure waves propagating in the fluid will reflect off the surface and affect the dynamics of the beam. For comparison, Table 3.2 summarizes the bimorph cantilever and the EHA rectification reed valve. Table 3.3 summarizes the properties of the highest viscosity fluid used in the study and the EHA working fluid.

	<b>Bimorph Cantilever</b>	<b>Reed Valve</b>
<b>Thickness [in]</b>	0.020	0.005
<b>Length [in]</b>	0.346	0.240*
<b>Width [in]</b>	0.039	0.200*

Table 3.2: Comparison of bimorph cantilever used by Naik et al. [36] and rectification reed valves used in EHA. Values denoted with (\*) are approximate due to irregular geometry.

	<b>FC-70 Fluid</b>	<b>Mobil DTE25 Fluid</b>
<b>Density (<math>\rho_f</math>) [kg/m<sup>3</sup>]</b>	1940	876
<b>Dynamic viscosity (<math>\mu_f</math>) [Pa-s (10<sup>-3</sup>)]</b>	27.16	48.36
<b>Kinematic viscosity (<math>\nu_f</math>) [cSt]</b>	14	55.4

Table 3.3: Comparison of fluid (FC-70) used by Naik et al. [36] and EHA working fluid (Mobil DTE25) used in EHA.

The study estimates effective mass and damping by experimentally quantifying the quality factor and resonance frequency. The flexural rigidity is estimated from experimental measurements and used to calculate the stiffness of the beam at a given resonance. The effective mass and damping are determined from the frequency response and quantified for each resonance of the beam up to the third harmonic. Knowing the values of mass and damping in air allows one to quantify the effective damping and added mass from the surrounding fluid and structure. The experimental results presented by Naik et al. show the large effect that the surrounding fluid and structure has on the response of the beam. Table 3.4 summarizes the change in damping ratio and resonant frequency comparing test results for the beams response in air, immersed in an infinite fluid and near a solid wall. The resonant frequency of the beam oscillating in an infinite fluid is reduced by 17% while oscillating in the same fluid near a solid surface is decreased by 41%.

	<b>Air</b>	<b>FC-70 fluid (infinite)</b>	<b>% change</b>	<b>FC-70 fluid (near wall)</b>	<b>% change</b>
<b>Effective <math>\zeta</math> (%)</b>	2.1	2.88	37%	23.5	1017.6%
<b><math>2^{nd} f_r</math> [kHz]</b>	18.6	15.5	-17%	11.0	-41%

Table 3.4: Summary of results for added mass and damping effects for bimorph cantilever submerged in FC-70 fluid by Naik et al. [36].

The phenomena to be quantified by the single degree-of-freedom reed valve mechanical model are complex. Losses occur from the viscous force around the boundary of the valve. Even at high speeds the viscous force on the upper and lower boundary of the valve will likely be a significant source of loss. The viscous forces on the

valve at interfaces near the solid structure will create a pressure proportional to the magnitude of the velocity and is the basis for the added damping. In addition to inertia loading due to the motion of the high density fluid on the valve, the static mass of the fluid increases the effective mass of the moving valve. The intention of this study is to generally quantify these effects in a simple framework that can be expanded in future efforts. It is beyond the scope of the work to investigate the effects described above for the valves used in this smart material EHA. The simple, single degree-of-freedom model attempts to capture the fluid and structural loading effects through two parameters: mass,  $\bar{m}_r$ , and damping,  $\bar{b}_r$ . The values used for system model simulation will be guided by the analytical and experimental work presented in this section. No-flow pressure testing of the Terfenol-D pump is used to correlate not only the mechanical dynamics presented in this section and section 3.1.3 but also the fluid-structural coupling in the fluid domain presented in section 3.2.4. The results of these simulations are presented in section 5.1 and 5.1.1. The effective mass of the valve is given by estimating a factor of 2.75 increase in mass due to structural effects over the analytical added mass predicted by equation (3.20). The equation for effective mass is given by:

$$\begin{aligned}\bar{m}_r &= 2.75(m_r + \tilde{m}_r) \\ \bar{m}_r &= 2.75 \left( (\rho_r * V_r) + \left( \frac{\pi}{4} \rho_f L_r w_r^2 \right) \right)\end{aligned}\tag{3.21}$$

The resulting effective mass,  $\bar{m}_r$ , is then  $0.364 \times 10^{-3}$  kg. The damping ratio is set at 0.1285 giving an effective damping coefficient,  $\bar{b}_r$ , of 0.4 Ns/m.

## 3.2 Fluid Model

### 3.2.1 Fluid Bulk Modulus

Fluid bulk modulus is a measure of the volume change,  $\Delta V$ , relative to some initial volume,  $V_o$ , for an applied pressure differential,  $\Delta P$ , defined by:

$$\beta = \frac{\Delta P}{\Delta V/V_o}. \quad (3.22)$$

If a fluid column is being compressed with constant cross-sectional area, equation (3.22) becomes:

$$\beta = \frac{\Delta P}{\Delta h/h_o}, \quad (3.23)$$

where  $\Delta h$  is the change in height of the fluid column and  $h_o$  is the initial height. In this form the bulk modulus is equivalent to the Young's modulus for solid materials where applied stress,  $\sigma$ , is equivalent to the applied difference in pressure,  $\Delta P$ . From equation (3.23) it can be shown that for a given compression,  $\Delta h$ , and initial height,  $h_o$ , an increasing bulk modulus will increase the pressure of the fluid. Therefore it is desirable to use a working fluid in the EHA system with a high bulk modulus. The bulk modulus can be adversely affected by air trapped in the fluid as well as expansion of the surrounding structure. The model assumes a very stiff structure and accounts for entrapped air by considering the volume change due to compression of gas,  $\Delta V_{gas}$ , with an initial volume,  $V_o$ , as a function of the percentage of gas in the fluid,  $\alpha$ , and bulk modulus of the gas,  $\beta_{gas}$  given by:

$$\Delta V_{gas} = \frac{\alpha V_o}{\beta_{gas}} \Delta P. \quad (3.24)$$

Assuming adiabatic compression the gas bulk modulus is a function of the ratio of specific heats for the gas,  $\gamma$ , and the bias pressure of the fluid in the circuit,  $p_{bias}$ ,

given by:

$$\beta_{gas} = \gamma p_{bias} \text{ [25]}. \quad (3.25)$$

An effective bulk modulus of the fluid is obtained by solving for the total volume expansion using equations (3.22) and (3.24) and putting into the form of equation (3.22) where  $\Delta V$  is  $\Delta V_{total}$  giving:

$$\beta_{eff} = \frac{\Delta P}{\Delta V_{total}/V_o} = \frac{1}{\left(\frac{1-\alpha}{\beta} + \frac{\alpha}{\beta_{gas}}\right)} \text{ [20]}. \quad (3.26)$$

This expression accounts for the primary source of volume expansion in a given volume containing a fluid with trapped gas. From equation (3.26) it can be seen that increasing the amount of entrained air will reduce the effective bulk modulus. For a high bias pressure of 1 ksi a relatively small percentage of air, 1%, can reduce the bulk modulus by over 60% [25].

### 3.2.2 Lumped Fluid Resistance and Capacitance

The topic of lumped parameter fluid modeling has been discussed in the literature and several textbooks [20, 25]. This section will briefly review the lumped fluid resistance and capacitance elements used in the fluid domain model for the EHA. Fluid resistance arises from friction in a rigid fluid conduit. The frictional contact of the fluid flowing against a rigid wall has a dissipative effect that necessitates a pressure differential to drive the fluid through a conduit. Ignoring the density of a lump of fluid with pressure difference  $\Delta P_{12}$  the flow rate through the fluid lump,  $q_{12}$ , will be:

$$q_{12} = \Delta P_{12}/R_f \text{ [20]}. \quad (3.27)$$

The fluid resistance element,  $R_f$ , is equivalent to an electrical resistance and equation (3.27) is the fluid equivalent of Ohm's Law for electrical circuits where  $\Delta P$  and  $q$

are the fluid equivalent of voltage and current. For laminar flow in a circular conduit the fluid resistance is:

$$R_f = \frac{128\mu L}{\pi D^4}, \quad (3.28)$$

where  $\mu_f$  is the dynamic viscosity of the fluid,  $L$  and  $D$  are the length and diameter of the conduit respectively. Fluid compliance accounts for the compressibility of the fluid and can be derived from applying conservation of mass to a lumped fluid element [25]. In this formulation, the compliance element is essentially a volumetric storage term. This is given by:

$$C_f = \frac{AL}{\beta}, \quad (3.29)$$

where  $\beta$  is the fluid bulk modulus, and  $A$  and  $L$  are the cross sectional area and length of the fluid element, respectively.

### 3.2.3 Hydraulic Circuit

Figure 3.5 shows a schematic representation of the hydraulic circuit for the smart material EHA. Flow continuity is used to develop four, first-order ordinary differential equations representing the dynamics of four state pressures. These pressures are located at the chamber,  $p_{ch}$ , fluid accumulator,  $p_{acc}$ , and low and high-pressure sides of the hydraulic cylinder,  $p_l$  and  $p_h$ . Each pressure is associated with a compressible control volume which gives rise to a fluid compliance as define by equation (3.29). Flow enters the pumping chamber through the inlet port,  $q_{ch,i}$ , and exits through the outlet port,  $q_{ch,o}$ . The piston pushes fluid at a volumetric rate proportional to its

velocity,  $q_{pi}$ . The flow continuity equation for the pumping chamber is:

$$\sum Q_{stored} = \sum Q_{in} - \sum Q_{out} \quad (3.30)$$

$$q_{str,ch} = q_{ch,i} + q_{pi} - q_{ch,o}$$

$$C_{ch}\dot{p}_{ch} = \frac{p_i - p_{ch}}{R_2(x_{ri})} + A_{pi}\dot{x}_p - \frac{p_{ch} - p_o}{R_1(x_{ro})}. \quad (3.31)$$

Solving for the intermediate pressures just upstream of the chamber outlet valve,  $p_o$ , just downstream of the inlet valve,  $p_i$ , and at the junction of the accumulator,  $p_a$ , yields the algebraic expressions:

$$p_o = \frac{R_1(x_{ro})}{R_1(x_{ro}) + R_3}p_h + \frac{R_3}{R_1(x_{ro}) + R_3}p_{ch},$$

$$p_i = \frac{R_2(x_{ri})}{R_2(x_{ri}) + R_4}p_a + \frac{R_4}{R_2(x_{ri}) + R_4}p_{ch},$$

$$p_a = \frac{(R_4R_5)p_l + (R_4R_6)p_{acc} + (R_5R_6)p_i}{R_4R_5 + R_4R_6 + R_5R_6}.$$

Defining equivalent resistances  $R_{eqv}$  and  $\hat{R}_{eqv}$  as

$$R_{eqv} = (R_2(x_{ri}) + R_4)(R_5 + R_6) + R_5R_6,$$

$$\hat{R}_{eqv} = \frac{R_5R_6(R_1(x_{ro}) + R_3) - R_{eqv}(R_1(x_{ro}) + R_2(x_{ri}) + R_3 + R_4)}{R_{eqv}(R_1(x_{ro}) + R_3)(R_2(x_{ri}) + R_4)},$$

the chamber pressure dynamic equation can be written as a function of the state pressures and piston velocity as:

$$\dot{p}_{ch} = \frac{A_{pi}}{C_{ch}}\dot{x}_p + \frac{\hat{R}_{eqv}}{C_{ch}}p_{ch} + \frac{R_6}{C_{ch}R_{eqv}}p_{acc} + \frac{1}{C_{ch}(R_1(x_{ro}) + R_3)}p_h + \frac{R_5}{C_{ch}R_{eqv}}p_l. \quad (3.32)$$

Flow is supplied to the pumping chamber during the refill stage of the pump from the low-pressure side of the hydraulic cylinder and the accumulator. The fluid stored due to the compressibility at the accumulator ( $C_{acc} \times p_{acc}$ ) is equal to the flow rate

exiting the low-pressure side of the hydraulic cylinder,  $q_l$ , less the flow to the inlet of the pumping chamber given by:

$$q_{str,acc} = q_l - q_{ch,i}$$

Using a method similar to that used to derive equation (3.32) the rate of change of the accumulator pressure is solved as:

$$\dot{p}_{acc} = \frac{R_6}{C_{acc}R_{eqv}}p_{ch} + \frac{R_6(R_2(x_{ri}) + R_4) - R_{eqv}}{C_{acc}R_5R_{eqv}}p_{acc} + \frac{R_2(x_{ri}) + R_4}{C_{acc}R_{eqv}}p_h. \quad (3.33)$$

The high-pressure pulses of fluid that pass through the outlet rectification reed valve produce nearly continuous flow into the high-pressure side of the hydraulic cylinder. The flow pushes against the output piston inducing a volumetric change per unit time,  $q_{po}$ . The flow continuity for this section is given by:

$$q_{str,h} = q_{ch,o} - q_{po}.$$

From flow continuity the high-side pressure time derivative is solved as:

$$\dot{p}_h = \frac{1}{C_h(R_1(x_{ro}) + R_3)}p_{ch} - \frac{1}{C_h(R_1(x_{ro}) + R_3)}p_h - \frac{A_{po}}{C_h}\dot{x}_{act}, \quad (3.34)$$

As the output hydraulic cylinder piston moves, fluid is displaced to the inlet of the pump and the accumulator. The flow continuity equation for the low-pressure side of the hydraulic circuit is:

$$q_{str,l} = -q_l + q_{po}. \quad (3.35)$$

From this continuity equation the low-side pressure time derivative is:

$$\dot{p}_l = \frac{R_5}{C_lR_{eqv}}p_{ch} + \frac{R_2(x_{ri}) + R_4}{C_lR_{eqv}}p_{acc} + \frac{R_5(R_2(x_{ri}) + R_4) - R_{eqv}}{C_lR_6R_{eqv}}p_l + \frac{A_{po}}{C_l}\dot{x}_{act}. \quad (3.36)$$

The lumped capacitances for each state pressure are derived using equation (3.29). The fluid-structure coupling in the fluid domain is characterized by the relationship between the rectification valve resistance and motion represented by  $R_1(x_{ro})$  and  $R_2(x_{ri})$ . The method used to develop this relationship is described in the following section.

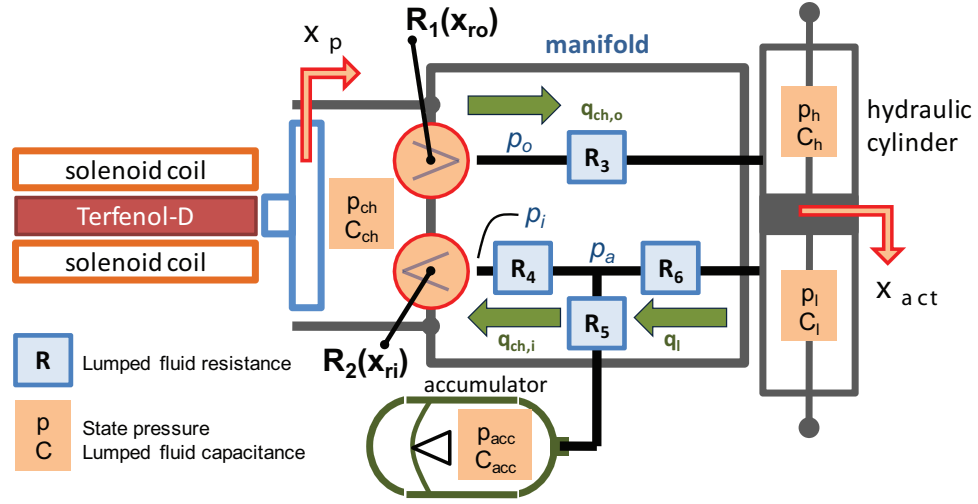


Figure 3.5: Schematic illustration of the hydraulic circuit and mechanical inputs for the smart material EHA. The fluid domain is defined by four state pressures, lumped resistances and capacitances. Fluid-structural coupling in the fluid domain is modeled through the dependence of rectification valve resistances ( $R_1$  and  $R_2$ ) on valve motion ( $x_{ro}$  and  $x_{ri}$ ).

### 3.2.4 Fluid-Structure Coupling

Fluid-structure coupling describes the complex interaction of a working fluid for an EHA and the rectification valves in a Terfenol-D pump. Design optimization of the smart material EHA rectification valves can be accomplished by fully understanding the fluid dynamics and structural interaction effects. As mentioned previously

the goal of this study is not to fully quantify this coupling, but rather to establish a baseline understanding of the phenomena and simple framework implementation. The process of rectification is reiterated as follows. During the positive stroke of the pumping piston an increasing pressure difference is created on the outlet rectification reed valve. This pressure difference, represented in the mechanical domain by  $p_{ch} - p_o$ , drives the valve open allowing the high-pressure fluid in the chamber to pass to the high side of the hydraulic cylinder. The retraction of the piston and subsequent chamber volume expansion reduces the chamber pressure. The drop in chamber pressure reduces the driving differential for the outlet valve and increases the pressure difference for the inlet valve,  $p_i - p_{ch}$ . Each driving pressure difference is only significant when greater than zero, as the valve seat restricts motion in the non-preferred direction of flow. This section presents a method for quantifying the fluid-structure coupling in the fluid domain as the effect of the valve motion on the fluid resistance ( $R_1(x_{ro})$  and  $R_2(x_{ri})$ ).

Multi-physics finite element software (COMSOL v3.4) is used to determine the coupling between the position of a reed valve and the fluid resistance associated with that position. A schematic illustrating the location and orientation of the outlet reed valve with respect to the pump head housing is shown in Figure 3.6(a). The geometry used in the finite element model is the same as the actual geometry of the reed and port and is shown in Figure 3.6(b). Mobil DTE25 hydraulic oil is simulated flowing through the valve. The properties of this fluid are given in Table 3.3 in section 3.1.3. The chamber piston motion is the source of the flow rate through the outlet valve. To determine the average flow rate through the outlet valve the piston motion is assumed

harmonic as:

$$x_p = -X_p \cos(\omega t) + X_p, \quad (3.37)$$

where  $X_p$  is the magnitude of the piston motion ( $L_{td}\epsilon_{td}$ ). The flow rate induced by the piston,  $q_{pi} = A_{pi}\dot{x}_p$ , will then be:

$$q_{pi} = A_{pi}X_p\omega \sin(\omega t). \quad (3.38)$$

The average outlet valve flow rate is defined as the total amount of fluid volume displaced through the outlet valve by the piston over one cycle. Only the positive half of the harmonic flow rate is considered because it is assumed the valve is closed during the negative cycle of the piston. Without this assumption the total flow through the valve for an entire cycle would be zero. The average flow rate through the outlet valve is:

$$\bar{Q}_{oc} = \frac{1}{T} \int_0^{\frac{T}{2}} A_{pi}X_p\omega \sin(\omega t) dt = 2A_{pi}X_pf, \quad (3.39)$$

where  $f$  is the pumping frequency and  $T$  is the period.

The finite element analysis simulates a constant flow rate through the valve at static valve openings defined by tip displacement. The finite element analysis evaluates the fluid dynamics of the complex 3D geometry and flow path and determines how the resistance to flow changes as the valve opens. No slip boundary conditions are used at all surfaces other than the inlet and outlet shown in Figure 3.6(b). The piston is assumed to displace 0.0036 in which is equivalent to a strain of  $800 \mu\epsilon$  for a 4.5 in Terfenol-D rod. Equation (3.39) shows the average flow rate induced by the pump through the outlet valve is proportional to frequency. A relatively low frequency is selected at 20 Hz which gives a flow rate through the outlet valve of  $1.58 \times 10^{-6} \text{ m}^3/\text{s}$ . This flow rate is used as the input boundary condition for the finite element model.

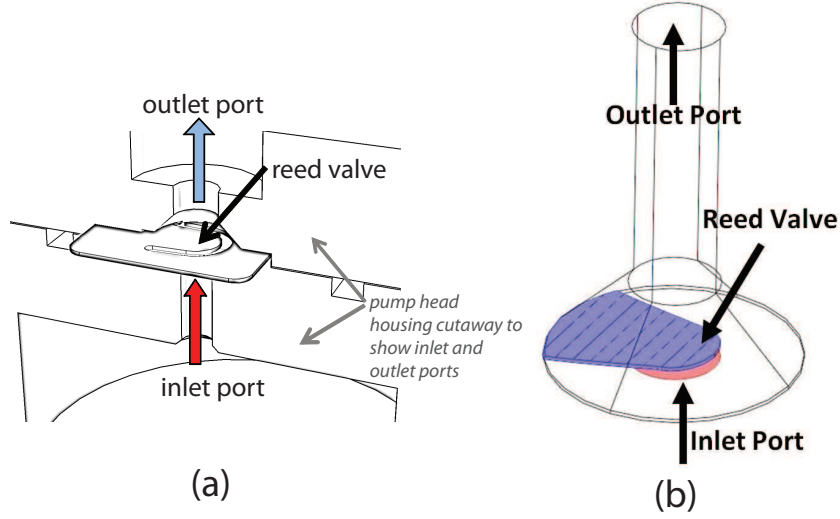


Figure 3.6: (a) Schematic of outlet reed valve orientation in EHA pump head with inlet and outlet port shown. (b) Finite element model geometry for characterization of fluid-structure coupling in mechanical reed valves.

Test cases of varying flow rates for a given valve deflection verify the resistance to be independent of an applicable range of flow rates in the simulation. A flow rate of  $1.58 \times 10^{-6} \text{ m}^3/\text{s}$  allows for efficient solution of the complex, 3D model and is applied to all FEA cases presented here. The outlet boundary condition is a constant pressure of 1 psi which ensures the constant flow rate condition for the simulation. Figure 3.7 shows a plot of the simulation results for valve tip displacements from 2 to 1210  $\mu\text{m}$ . The simulation results show a very rapid decrease in resistance as the valve opens as the resistance drops 70% from a valve opening from 2 to 49  $\mu\text{m}$ . As the valve opens further, the resistance rate of decrease slows. The plot can be approximated by an exponential function also shown in Figure 3.7 given as:

$$\tilde{R}(x) = 2.34 \times 10^{11} e^{(-0.025x)}. \quad (3.40)$$

Linear interpolation between the data points from the FE simulation is used to establish the fluid-structure coupling in the fluid domain ( $R(x)$ ). The end points of this function are not obtained from the simulation results. The theoretical fluid resistance at a reed valve tip displacement of zero is infinite. The numerical solver used for the system model cannot converge on a solution using an infinite value for the closed-valve fluid resistance. Based on experience with the fluid resistance in the model a value of  $1 \times 10^{17}$  Pa-s/m<sup>3</sup> is used to approximate the infinite, closed-valve resistance. The assumption is made that the valve will not deflect more than 5 mm and the valve resistance will not drop below  $4.5 \times 10^8$  Pa-s/m<sup>3</sup>. This assumption established the end point for the function  $R(x)$  and ensures the resistance stays in a range that is reasonable for the valve motion. The 3D finite element simulation results along with the lumped parameter equations developed in section 3.2.3 fully define the fluid-structure coupling of the reed valves and the fluid domain of the system model.

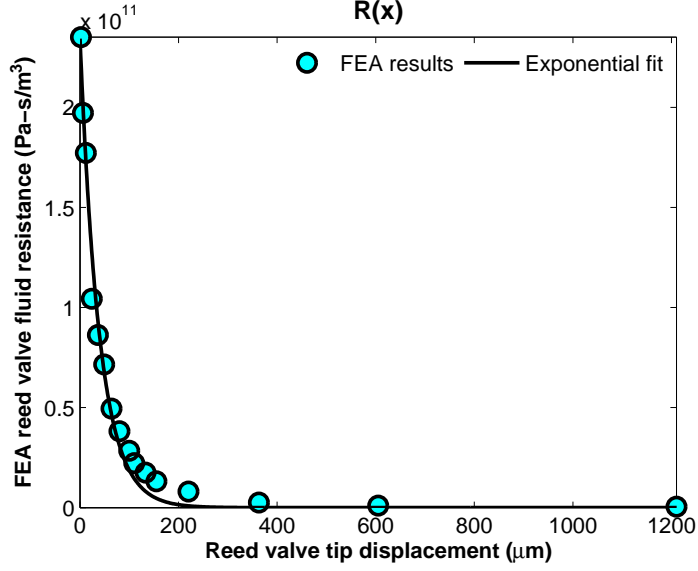


Figure 3.7: Finite element simulation results of fluid-structure interaction for the rectification reed valves in the smart material pump. The simulation uses a constant flow rate condition to determine the fluid resistance for the valve ( $R$ ) as a function of the tip displacements ( $x$ ) from 2 to 1012  $\mu\text{m}$ .

### 3.3 System Model

#### 3.3.1 System Model Equations

The equations presented in sections 3.1 and 3.2 capture the dynamic behavior of the mechanical and fluid domain of the smart material EHA. In the mechanical domain Newton's method is used along with discrete models to derive the equations of motion for the input piston, chamber fluid mass, rectification reed valves, and output piston. The effects of the fluid-structure interaction are considered when developing the mechanical models for the reed valves. Mass and damping values of the reed model are adjusted to account for these effects. Fluid volume flow continuity along

with lumped fluid resistance and capacitance are used to develop the dynamic, time-domain equations for the fluid domain. Fluid-structure interaction is introduced as a dependence of rectification valve resistance on valve motion from the mechanical domain. This coupling between the fluid and mechanical domain is the basis for the fluid-structure coupling for the rectification valves. The system equations are summarized here. Simulation results of the system model are presented in chapter 5.

$$\begin{aligned}
m_{eff}\ddot{x}_p + (b_f + b_{eff})\dot{x}_p - b_f\dot{x}_f + (k_{eff} + k_f)x_p - k_fx_f &= Nqk_{td}I \\
m_f\ddot{x}_f - b_f\dot{x}_p + b_f\dot{x}_f - k_fx_p + k_fx_f &= p_{ch}A_{pi} \\
m_l\ddot{x}_{act} + b_l\dot{x}_{act} + k_lx_{act} &= (p_h - p_l)A_{po} \\
\bar{m}_r\ddot{x}_{ro} + \bar{b}_r\dot{x}_{ro} + k_rx_{ro} &= (p_{ch} - p_o)A_r \\
\bar{m}_r\ddot{x}_{ri} + \bar{b}_r\dot{x}_{ri} + k_rx_{ri} &= (p_i - p_{ch})A_r \\
\dot{p}_{ch} &= \left(\frac{A_{pi}}{C_{ch}}\right)\dot{x}_p + \left(\frac{\hat{R}_{eqv}}{C_{ch}}\right)p_{ch} + \left(\frac{R_6}{C_{ch}R_{eqv}}\right)p_{acc} \\
&\dots + \left(\frac{1}{C_{ch}(R_1(x_{ro}) + R_3)}\right)p_h + \left(\frac{R_5}{C_{ch}R_{eqv}}\right)p_l \\
\dot{p}_{acc} &= \left(\frac{R_6}{C_{acc}R_{eqv}}\right)p_{ch} + \left(\frac{R_6(R_2(x_{ri}) + R_4) - R_{eqv}}{C_{acc}R_5R_{eqv}}\right)p_{acc} \\
&\dots + \left(\frac{R_2(x_{ri}) + R_4}{C_{acc}R_{eqv}}\right)p_h \\
\dot{p}_h &= \left(\frac{1}{C_h(R_1(x_{ro}) + R_3)}\right)p_{ch} - \left(\frac{1}{C_h(R_1(x_{ro}) + R_3)}\right)p_h - \left(\frac{A_{po}}{C_h}\right)\dot{x}_{act} \\
\dot{p}_l &= \left(\frac{R_5}{C_lR_{eqv}}\right)p_{ch} + \left(\frac{R_2(x_{ri}) + R_4}{C_lR_{eqv}}\right)p_{acc} \\
&\dots + \left(\frac{R_5(R_2(x_{ri}) + R_4) - R_{eqv}}{C_lR_6R_{eqv}}\right)p_l + \left(\frac{A_{po}}{C_l}\right)\dot{x}_{act}
\end{aligned}$$

### 3.3.2 Summary of System Model Parameters

<b>Terfenol-D Transducer Properties</b>	
$E_Y^H$	Terfenol-D rod Young's modulus at constant field
$A_{td}$	Cross-sectional area of Terfenol-D rod
$L_{td}$	Length of Terfenol-D rod
$k_{td}$	Stiffness of Terfenol-D rod ( $E_Y^H A_{td}/L_{td}$ )
$k_d$	Stiffness of diaphragm
$k_{eff}$	Combined stiffness of Terfenol-D rod and diaphragm ( $k_{td} + k_d$ )
$m_{eff}$	Mass of piston and dynamic mass of Terfenol-D rod
$b_{eff}$	Damping coefficient of diaphragm and Terfenol-D rod
$N$	Number of turns in solenoid coil
$I$	Solenoid current
$q$	Piezomagnetic coefficient
$F_{td}$	Force produced by Terfenol-D rod ( $Nqk_{td}$ )
<b>Pumping Chamber, Piston, &amp; Fluid Properties</b>	
$h_{ch}$	Height of pumping chamber
$A_{pi}$	Area of chamber piston
$V_c$	Volume of chamber ( $A_{pi}h_{ch}$ )
$\beta_{eff}$	Effective fluid bulk modulus (equation (3.26))
$C_{ch}$	Chamber fluid capacitance ( $A_{pi}h_{ch}/\beta_{eff}$ )
$\rho_f$	Fluid density
$\mu_f$	Fluid dynamic viscosity
$k_f$	Chamber fluid stiffness ( $\beta_{eff}A_{pi}/h_{ch}$ )
$b_f$	Damping coefficient of fluid in chamber
$m_f$	Mass of fluid in chamber ( $V_c \times \rho_f$ )
<b>Rectification Reed Valve Properties</b>	
$k_r$	Bending stiffness of cantilever valve
$\bar{b}_r$	Effective damping coefficient accounting for fluid effects
$\bar{m}_r$	Effective mass accounting for fluid effects
$A_r$	Fluid contact area
$R_1(x_{ro})$	Dynamic fluid resistance of outlet reed valve
$R_2(x_{ri})$	Dynamic fluid resistance of inlet reed valve

Table 3.5: Summary of parameters for Terfenol-D transducer, Terfenol-D pump, and rectification reed valve models in the mechanical and fluid domains.

<b>Output Hydraulic Cylinder Properties</b>	
$A_{po}$	Contact area of output piston
$L_{act}$	Wetted length of output cylinder
$\xi_h$	Ratio of wetted length on high-pressure side of the cylinder ( $< 1$ )
$C_h$	Capacitance of fluid in high-pressure side ( $A_{po}\xi_h L_{act}/\beta_{eff}$ )
$C_l$	Capacitance of fluid in low-pressure side ( $A_{po}(1 - \xi_h)L_{act}/\beta_{eff}$ )
$k_l$	Stiffness of load attached to actuator
$b_l$	Damping coefficient of load attached to actuator
$m_l$	Mass of output piston and load attached to actuator
<b>Hydraulic Circuit Properties</b>	
$d_{line}$	Diameter of fluid lines
$L_{line}$	Line length
$R_{3,4,5,6}$	Line resistances ( $128\mu_f L_{line}/\pi d_{line}^4$ )
<b>Fluid Accumulator Properties</b>	
$m_{gas}$	Mass of gas in accumulator
$R$	Gas constant
$T_{acc}$	Temperature of gas in accumulator
$p_{bias}$	Bias pressure of fluid
$C_{acc}$	Capacitance of fluid in accumulator ( $m_{gas}RT_{acc}/p_{bias}^2$ )

Table 3.6: Summary of parameters for the smart material EHA output cylinder, hydraulic circuit, and fluid accumulator.

## CHAPTER 4

### TERFENOL-D PUMP AND REED VALVE TESTING

#### 4.1 Terfenol-D Pump Details

The magnetostrictive material Terfenol-D is employed as the driver for the pump studied in this research. Terfenol-D is the smart material indicated in Figure 2.9 and a solenoid coil is the electrical input element. The solenoid coil produces the driving magnetic field for the Terfenol-D rod from the electrical voltage and current input. This section presents the details of the Terfenol-D pump studied.

Figure 4.1 shows a 3D model exploded cutout view of the Terfenol-D pump with the major elements specified. The large base mass decreases experimental noise by isolating the pump from external vibratory disturbances. The method for pre-loading the Terfenol-D rod is discussed in section 4.2.1. A pre-load bolt and the hydraulic circuit bias pressure apply the pre-load to the Terfenol-D rod. Six Alnico V magnets are assembled in a precisely machined sleeve and form the outer housing around the Terfenol-D rod and solenoid coil. In addition to providing a magnetic bias, the magnet stack provides the critical alignment between the pump head and the base which ensures the Terfenol-D rod is not loaded in torsion or bending. Additional information on the magnet stack is given in section 4.1 and Appendix B.1 of reference [42]. The

solenoid coil has 860 turns using 20 AWG insulated copper wire. The DC resistance is approximately  $1.9\ \Omega$  and the inductance is 1.30 mH. The Terfenol-D rod, magnet stack, and solenoid coil are located concentrically and are clamped between the pump head and base. The entire pump is secured to the base using seven struts. Hex bolts at the upper end of the strut apply pressure to the pump head clamping the pump head, piston assembly, and magnet stack to the base.

Figure 4.2 shows an exploded section view of the pump head. The piston assembly is comprised of two piston halves and a 0.005 in stainless steel diaphragm. To seal the pumping chamber the two piston halves clamp the diaphragm as shown in Figure 4.2. The outer edge of the diaphragm is then clamped between the chamber ring and the top face of the piston guide ring. The piston guide ring is the structural element between the piston assembly and the magnet stack shown in Figure 4.1. The chamber ring defines the height of the pumping chamber (0.05 in). Additional sealing is provided by two Parker #2-228 o-rings located in the grooves located on the upper and lower faces of the chamber ring. System compliance significantly reduces pump performance. As the piston compresses the fluid in the chamber, the high pressure fluid will expand to and deform the o-ring seals. Even small volume changes created by the deformed o-ring will be significant relative to the volume displacement of the piston. Improperly designed seals can significantly reduce pump performance and should be a major consideration in design.

The inlet and outlet rectification reed valves are located on the upper face of the chamber housing. The valves are located on rectangular protrusions on the chamber housing and pump cap. The outlet valve on a protrusion from the chamber housing and the inlet valve from the pump cap. The protrusion feature on each piece is

matched with a pocket on the opposing face which allows enough clearance to clamp the 0.005 in stainless steel reed valves in place. The surface around the valve flap is clamped between the pump cap and chamber housing leaving the flap free to deflect in the preferred direction of flow. The fluid rectification process is critical to the operation of the pump and is described in detail in section 2.5.1. Other pertinent details of the pump geometry are summarized in appendix A in Table A.1. The chamber housing and pump cap have seven clearance holes for the struts. Hex bolts are assembled at the threaded end of the struts to clamp the pump head, piston assembly, and magnet stack to the base.

## 4.2 Terfenol-D Pump Testing Setup

To properly characterize the Terfenol-D pump the acquisition system must be able to capture fluid, electrical, and mechanical variables. Figure 4.8 at the end of this chapter illustrates the setup to acquire data from the smart material EHA. Key information about the testing setup is given in this schematic and further specifics are contained in section 4.3 of reference [42]. Additionally the pump requires two pre-conditioning steps to maximize performance during testing. The discussion in section 3.2.1 indicated that air trapped in the working fluid of the EHA would significantly degrade performance. Section 4.2.1 of reference [42] describes a procedure for removing entrapped air in the fluid. This method is used for all tests whose results are presented here. The second pre-conditioning step in pump setup is applying the mechanical bias (pre-load) to the Terfenol-D rod. Figure 2.6 in section 2.3.2 illustrated the effect pre-load has on the strain output of the Terfenol-D rod. The following section will describe this step.

### 4.2.1 Terfenol-D Rod Pre-Load

Pre-loading the Terfenol-D rod ensures operation in a compressive state where the material can withstand higher stress. Additionally the pre-stress aligns magnetic moments in a favorable orientation for 90 degree domain rotation producing maximum magnetostriction as discussed in section 2.3.2. In the Terfenol-D pump, pre-loading is applied from two sources: the pre-load bolt and hydraulic circuit bias pressure. Figure 4.3(a) is a schematic of the Terfenol-D pump including the sealing diaphragm and illustrates the two sources of pre-load. The pre-loading force is related to the bias pressure in the hydraulic circuit by the piston cross-sectional area by:

$$F_{bias} = A_{pi}p_{bias}. \quad (4.1)$$

Figure 4.3(b) shows a lumped model illustrating the bias force working against the stiffness of the Terfenol-D rod and the diaphragm. The pre-load bolt shown in Figure 4.3(a) is used to adjust the position of the Terfenol-D rod to return the diaphragm to an un-deflected position. Pre-loading of the Terfenol-D rod occurs after the assembly of the pump and circuit as well as the addition and subsequent degassing of the hydraulic fluid. Figure 4.4 illustrates the necessary steps to incrementally pre-load the Terfenol-D rod. The bias pressure must be incrementally increased alternating with pre-load bolt adjustment. Two values must be specified before the pre-loading steps: the Young's modulus of the Terfenol-D rod at constant field ( $E_Y^H$ ) and the maximum deflection of the sealing diaphragm ( $\Delta x_{max}$ ). Young's modulus at constant field of 300 Oe (supplied by the permanent magnet) is approximately 30 GPa. The maximum deflection of the diaphragm should be set such that the diaphragm does not permanently deform. The diaphragm and piston assembly stiffness was measured in a MTS

compression system and elastic deformation occurred up to 0.008 mm [42]. To ensure permanent deflection does not occur, the maximum allowable diaphragm deflection ( $\Delta x_{max}$ ) is set at 0.008 mm. Figure 4.4(a) shows the Terfenol-D rod and diaphragm in an undeformed state with zero pre-stress. An incremental pressure ( $\Delta P$ ) is applied to the hydraulic circuit. The amount of pressure is determined from the maximum diaphragm deflection by:

$$\Delta P_{max} = \frac{k_d + k_{td}}{A_{pi}} \Delta x_{max}. \quad (4.2)$$

This equation is derived from equating the diaphragm deflection with the piston deflection ( $x_p$ ) shown in Figure 4.3 and holding the base deflection ( $x_b$ ) to zero. The diaphragm stiffness is found via testing to be 2.15 MN/m and the Terfenol-D rod stiffness is related to the Young's modulus by equation (3.2). Figure 4.4(b) illustrates the deflection of the Terfenol-D rod and diaphragm by the pre-defined maximum. The incremental strain induced in the Terfenol-D rod by this bias force is related to the length of the Terfenol-D rod,  $L_{td}$ , by:

$$\Delta \epsilon_{td} = \frac{\Delta x_{max}}{L_{td}}. \quad (4.3)$$

Figure 4.4(c) shows the last step in one increment of the pre-loading process where the pre-load bolt is adjusted to return the diaphragm to an undeformed state. By equating the preload bolt adjustment ( $\Delta x_b$ ) to the maximum deflection of the diaphragm the incremental strain is held constant determined by equation (4.3). The total pre-stress is related to the strain of the Terfenol-D rod and the Young's modulus by:

$$\sigma_{pre} = E_Y^H \epsilon_{td}. \quad (4.4)$$

The Young's modulus at a DC bias magnetic field of 300 Oe is approximately 30 GPa. A pre-stress of 1.5 ksi is selected as the optimum mechanical bias for the Terfenol-D

rod. Based on equation (4.4) the required strain in the material is  $345 \mu\epsilon$ . Equation (4.2) gives a pressure increment ( $\Delta P_{max}$ ) of 81 psi for the values presented here. The specified value of the system bias pressure ( $p_{bias}$ ) will determine the number of pre-load increments, outlined in Figure 4.4, to reach the desired pre-stress in the Terfenol-D rod. The amount of pressure increment will likely need to decrease as the Terfenol-D rod strain nears the value given by equation (4.4). The decrease in pressure increment will be accompanied by a decrease in the diaphragm deflection in step (b) of Figure 4.4. The pre-load bolt adjustment will need to be altered based on the formulas presented in this section to ensure the bolt displacement ( $x_b$ ) is equal to the diaphragm deflection ( $x_p$ ).

### 4.3 In Situ Valve Measurement Setup

This section presents a method for measuring the displacement of the rectification reed valve in-situ. Acquiring the time domain motion of the reed valve as the pump is running characterizes the valve response to the fluid loading of the prototype Terfenol-D pump. This information elevates the level of characterization for the Terfenol-D pump. This section will review the measurement instrument used in this method, describe the method of measurement, present the modifications to the Terfenol-D pump which allow the measurement, and discuss the future work in the context of designing for more accurate measurements.

#### 4.3.1 Laser Sensor (LK-G32)

A Keyence model LK-G32 laser displacement sensor is used to measure the reed valve displacement. This section will briefly describe the principle of operation for this device. Figure 4.5(a) shows the laser head as well as the receiving components

for the reflected laser beam. Figure 4.5(b) shows the process of measuring the relative target displacement schematically. A beam of laser light is emitted perpendicular to the bottom face of the head toward the object to be measured (“target”). While the target will scatter the beam in many directions the laser head is set up to receive the reflected beam at a 40 degree angle on a Li-CCD array. The Li-CCD, or linearized charge-coupled device, is capable of converting the incoming light into electrons. The charge accumulated on each section of the Li-CCD array is proportional to the amount of light received. The initial position of the target will reflect the beam to a certain position on the Li-CCD array increasing the electrical charge in that small area of the array. The location of that charge indicates the position of the target as shown by the green spike of light intensity in Figure 4.5(b). As the target moves away from the beam source the reflected position on the CCD array shifts along with the location of the maximum light intensity. This shift, shown by the orange spike in Figure 4.5(b), is very accurately proportional to the amount of motion of the target. The system is capable of measuring small motions of the target through this method of converting the energy of the laser beam to an electrical charge on the CCD array. The Keyence LK-G32 laser is capable of measuring 10 mm of displacement with a repeatability of  $0.05\text{ }\mu\text{m}$  at a rate of 50,000 samples per second.

### **4.3.2 Design and Manufacture of Modified Pump Cap**

A transparent path from the laser sensor head to the reed valve is required because the laser sensor uses a visible laser beam to measure displacement. The implementation of this method is further complicated by the laser sensor head requiring two

transmission paths for the laser: emitted and received. The Terfenol-D pump described in section 4.1 does not have the necessary transparent paths for the laser beam to pass through. A modified pump cap was designed and manufactured in house to accommodate this requirement. A detailed drawing of the insert and modified pump cap are given in appendix C. Figure 4.6 shows a 3D drawing and section view of the modified pump cap insert. The flow path dimensions of the insert are equivalent to that used in the Terfenol-D pump shown in section 4.1 however the 90 degree bend relocates the obstruction created by the fitting attached to the outlet port away from the path of the laser beam. Dow Corning 832 sealant is used to seal the insert in the modified pump cap to prevent leakage from the outlet port shown in Figure 4.6(b).

Machining of the acrylic insert scores and renders the surface opaque. The scored surface can be polished to nearly the original transparency of the part. Because of the challenges the small passages and surfaces of the insert presented for polishing, the part was made by a company with the capability to rework the surfaces to a nearly transparent finish. The modified pump cap, which houses the insert, was made using a computer-controlled milling machine from M-code created from the 3D solid model and the program Feature CAM. An aluminum disk was turned to diameter and thickness prior to loading in the CNC mill. The CNC milling process creates the reed seats, partially drills the port holes, and drills locating holes for the struts. Post machining on a vertical mill is necessary to finish the port holes and drill the clearance holes for the struts. A bottom-tap is used to create the threads for the fittings connecting the tubing to the pump cap. A bottom-tap is necessary because of the face o-ring seal of the fittings. The reed seat protrusion on the modified pump

cap is filed and sanded to create a smooth surface that would mate with the existing pump. The thickness and diameter of the modified pump cap are larger than the original cap to accommodate the insert while all other dimensions critical for mating to the Terfenol-D pump are the same.

### 4.3.3 Reed Valve Displacement Measurement

Figure 4.7 shows a solid model of the experimental setup for measuring outlet rectification reed valve displacement in situ. Because the laser stand cantilevers the laser sensor head it is prone to vibrational noise and is clamped to the tubing of the hydraulic circuit to attenuate this effect. The software provided with the sensor has the capability to allow the user to observe light intensity during measurement. This function is used to ensure the highest strength signal to the laser sensor receiver. Prior to each test the head is adjusted so the light intensity plot shows a large spike at a given location and a low level of noise away from the peak similar to the illustration in Figure 4.5(b). This means that a small area of the CCD array is being activated by the reflected beam and a robust measurement of the target is being collected. The sensor is zeroed once a large, stable peak appears on the light intensity plot. Once the sensor head is adjusted and zeroed, measurements are taken during operation of the pump.

While the results presented in section 5.4 in chapter 5 establish the capability of this novel measurement method, there are several characteristics of this method that provide challenges in obtaining measurements. A literature review on the topic of in situ valve characterization for smart material pumps revealed that this is a new venture in this area. The challenges faced in this venture are discussed here to be used

as a guide for future design. Figure 4.6 indicates the location of the epoxy used to seal the insert in the pocket of the modified pump cap. Without the epoxy sealant, the high pressure at the outlet port would push hydraulic oil through the interface of the modified pump cap and insert leaking to the top of the cap. While sealing in some form is necessary, the epoxy located on the shoulder (step) of the insert allows displacement in the vertical direction shown in Figure 4.7. Minimizing system compliance is crucial for pump performance. Analysis shows that the compliance of the insert seal causes a 32% decrease in no-flow pressure at a 10 Hz pumping frequency. The refraction of the laser through the acrylic insert is another design challenge. As the beam passes from air to the acrylic insert to the hydraulic oil the change in speed will be accompanied by a change in angle. The motion of the insert due to epoxy compliance and the flowing oil adds to the complexity of this issue. Prior to the design of the insert, testing confirmed the laser's capability to measure accurately through acrylic and non-flowing hydraulic oil. Based on experience in testing using this method, the transparency and motion of the insert are critical for accurate measurements. In some cases during measurement the opaqueness of the insert, debris or bubbles in the oil interfere with the beam and push the measured displacement out of range. The primary impact of refraction is the uncertainty of location of measurement on the valve. The location of the laser determines the amount of displacement measured as the valve will deflect more at the tip relative to near the root. While successful in acquiring measurements, this first iteration design did not account for this effect and should be addressed in future iterations. Finally, photoelastic effects may be significant in this application due to a property called birefringence. This means that the stress and strain in the material effect the refraction of the insert and will

change how the laser beam passes through the acrylic. Based on the experience of this implementation, future design should focus on the machining and post-machining of the insert to minimize the amount of surface to be polished, leaving as much of the virgin material as possible. Additionally any compliance allowing motion of the insert should be eliminated and designs for a highly accurate measurement method may need to consider natural and stress-induced refraction.

## 4.4 Measurement Setup

Data collected to characterize the performance and behavior of the smart material pump and EHA comes from the electrical, mechanical, and fluid domains. The no-flow test condition described in section 2.5.2 is used for all data acquired through testing presented in chapter 5. The no-flow condition gives a repeatable test condition to measure valve motion and pump data. Simulation of the no-flow condition is also simple to implement.

Data is collected via a Data Physics Quattro system capable of receiving inputs at  $\pm 10$  V and supplying signals at  $\pm 5$  V. The signal out of the Quattro is amplified before being applied to the solenoid coil. Measurements can be acquired from the voltage and current monitors of the AE Techtron 5050 amplifier as well as from pressure transducers, strain gage, accelerometer, and the LK-G32 laser displacement sensor. Figure 4.8 illustrates the setup used to acquire data in the no-flow condition along with frequency bandwidth and sensitivity of the instruments. Additional information on the measurement instruments used can be found in section 4.3 of reference [42]. The operating conditions for the Terfenol-D pump and EHA are presented in section 2.5.2.

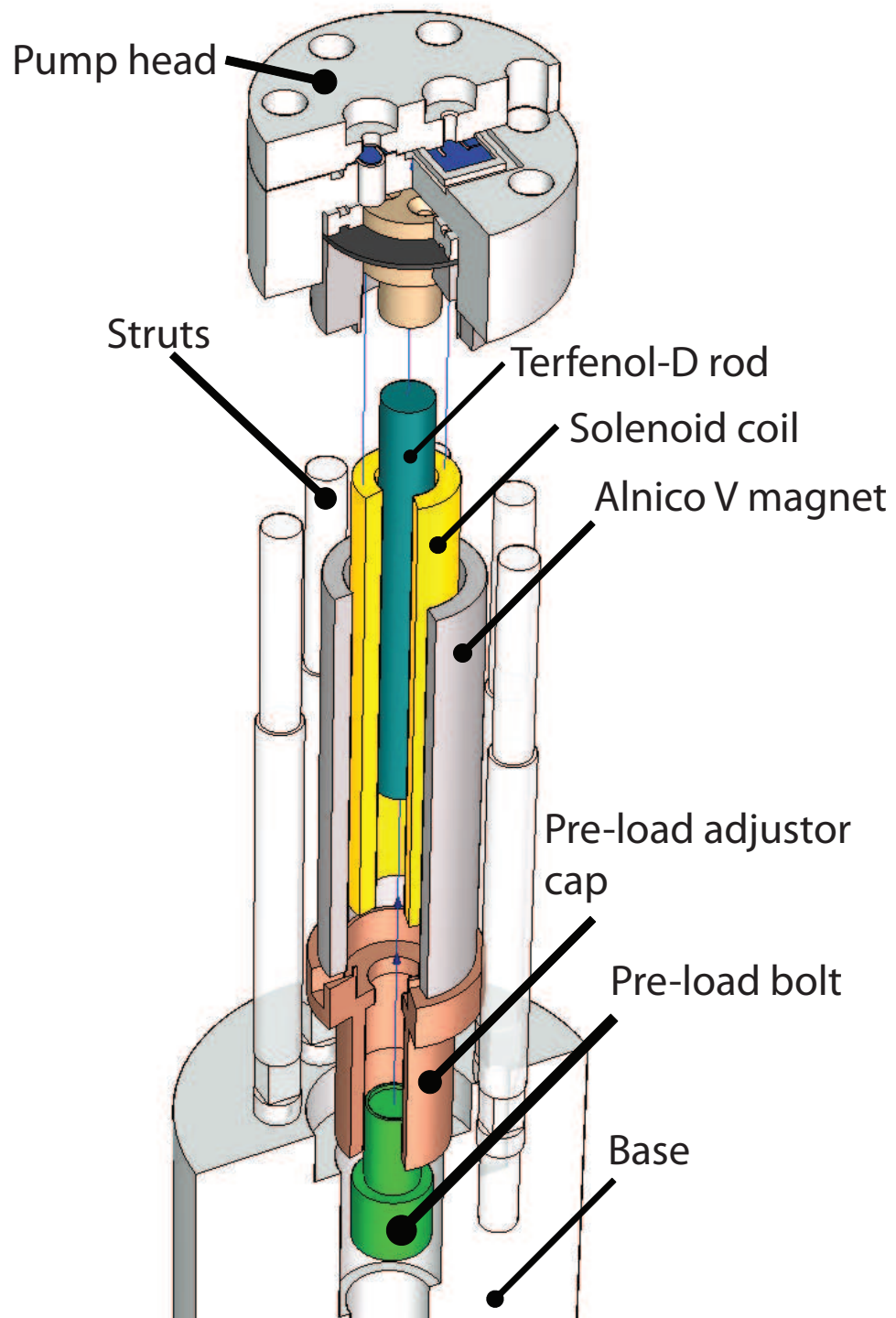


Figure 4.1: 3D exploded, sectioned view of Terfenol-D pump.

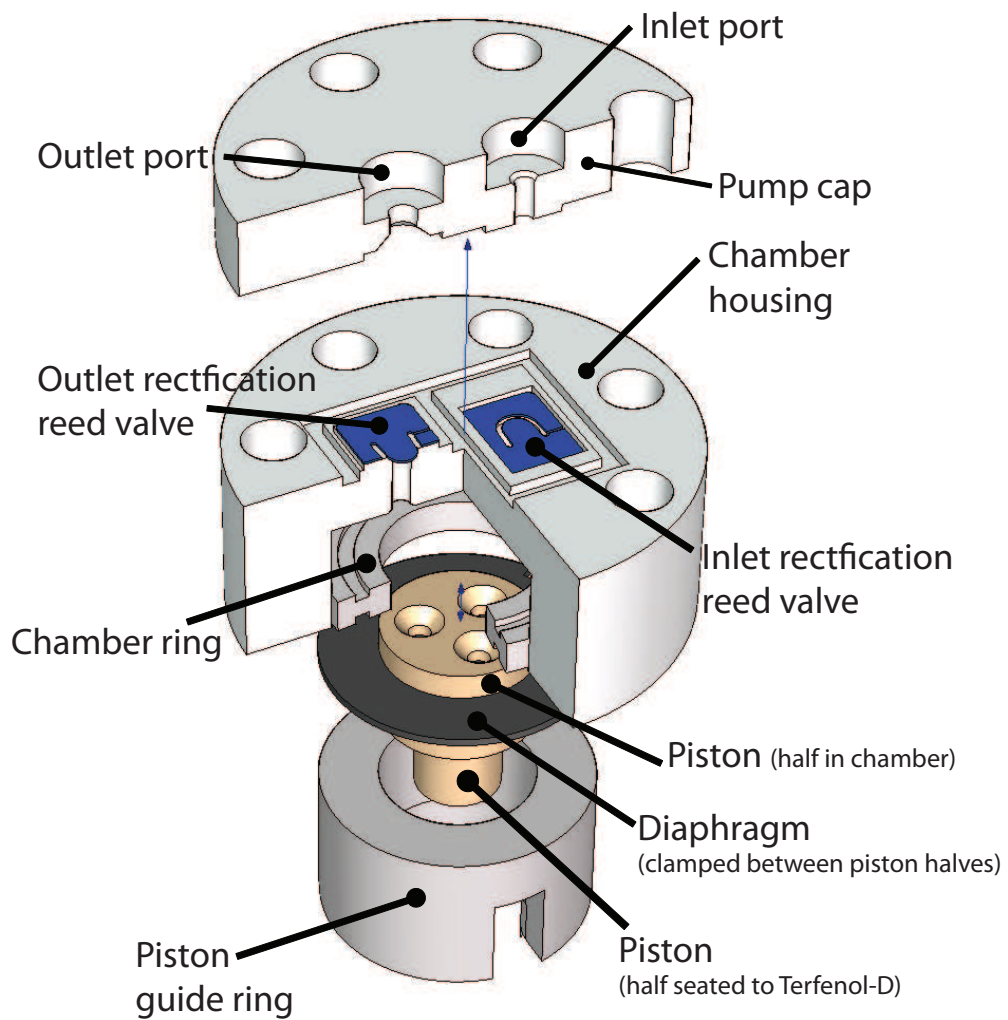


Figure 4.2: 3D exploded, sectioned view of Terfenol-D pump head.

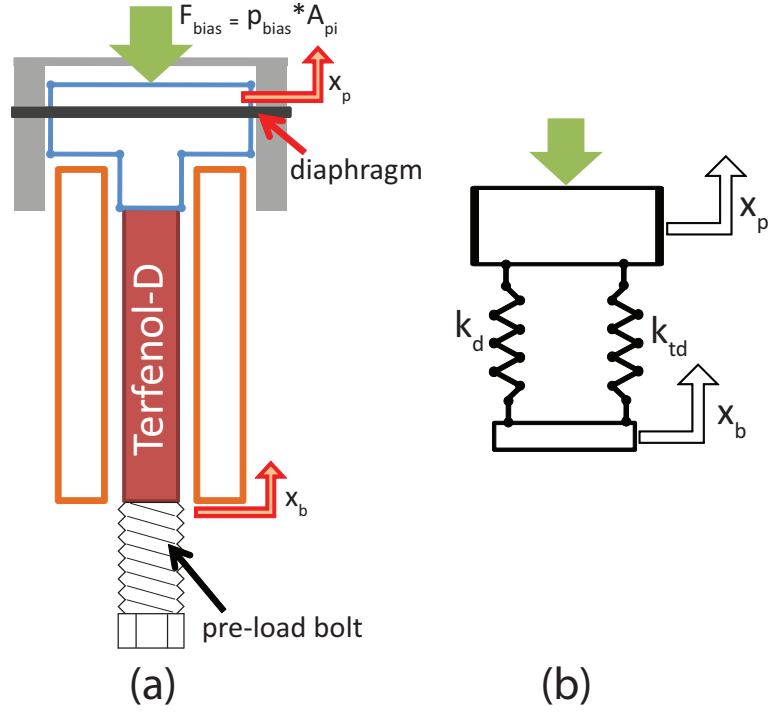


Figure 4.3: (a) Schematic illustrating the two sources of pre-load for the Terfenol-D rod: the force from the bias pressure applied to the piston area ( $F_{bias}$ ) and the compression from the pre-load bolt ( $x_b$ ). (b) Lumped model showing the stiffness of the Terfenol-D rod and diaphragm with the applied force, piston, and base displacement.

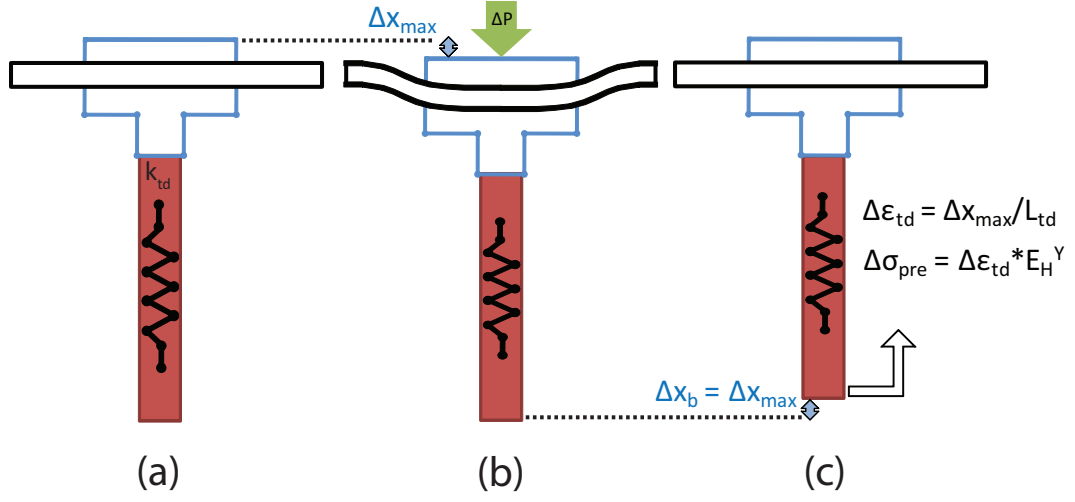


Figure 4.4: Illustration of the steps involved in one pre-load increment for preconditioning the Terfenol-D rod. (a) Initial state of piston, diaphragm, and Terfenol-D rod before pre-load is applied. (b) Incremental pressure is applied ( $\Delta P$ ) to the hydraulic circuit compressing the Terfenol-D rod and diaphragm by pre-defined displacement ( $\Delta x_{max}$ ). (c) Pre-load bolt is adjusted by  $\Delta x_{max}$  to return diaphragm to un-deflected state. After steps (a), (b), and (c) the Terfenol-D rod has been stress by an increment of  $\sigma_{pre} = \Delta x_{max} E_Y^H / L_{td}$ .

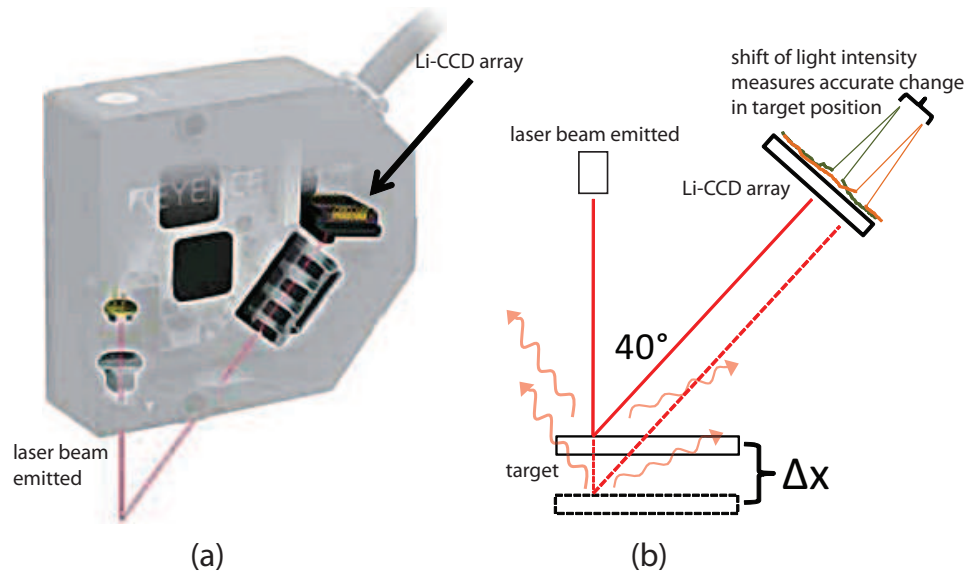


Figure 4.5: (a) 3D illustration of the LK-G32 laser sensor head and internal receiving components (Li-CCD and lens unit). (b) Schematic illustrating the principle of operation for the emission and reception of the laser beam for measuring a moving target. The charge of the array is proportional to the light intensity and knowing the location of the high charge indicates the relative location of the target.

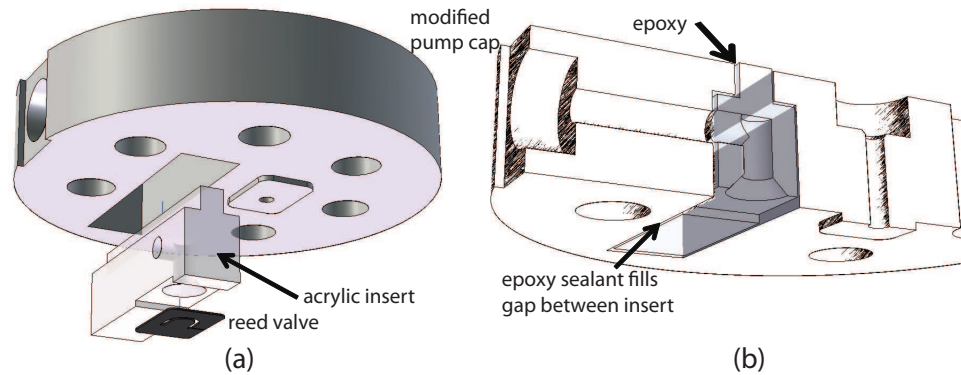


Figure 4.6: (a) Exploded 3D solid model of modified pump cap, acrylic insert, and outlet reed valve. (b) Cutaway 3D model of assembled modified pump cap and insert. Epoxy is used to seal the gap between the insert and the pocket of the pump cap.

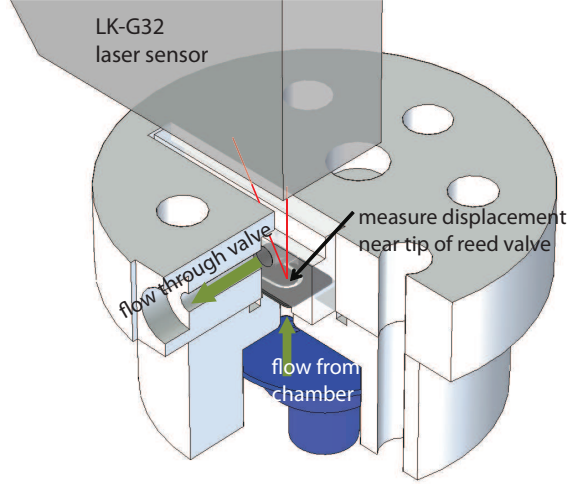


Figure 4.7: Cutaway view of a solid model of the experimental setup for in situ outlet reed valve displacement measurement with the LK-G32 laser displacement sensor, modified pump cap, insert, outlet reed valve and pumping chamber shown.

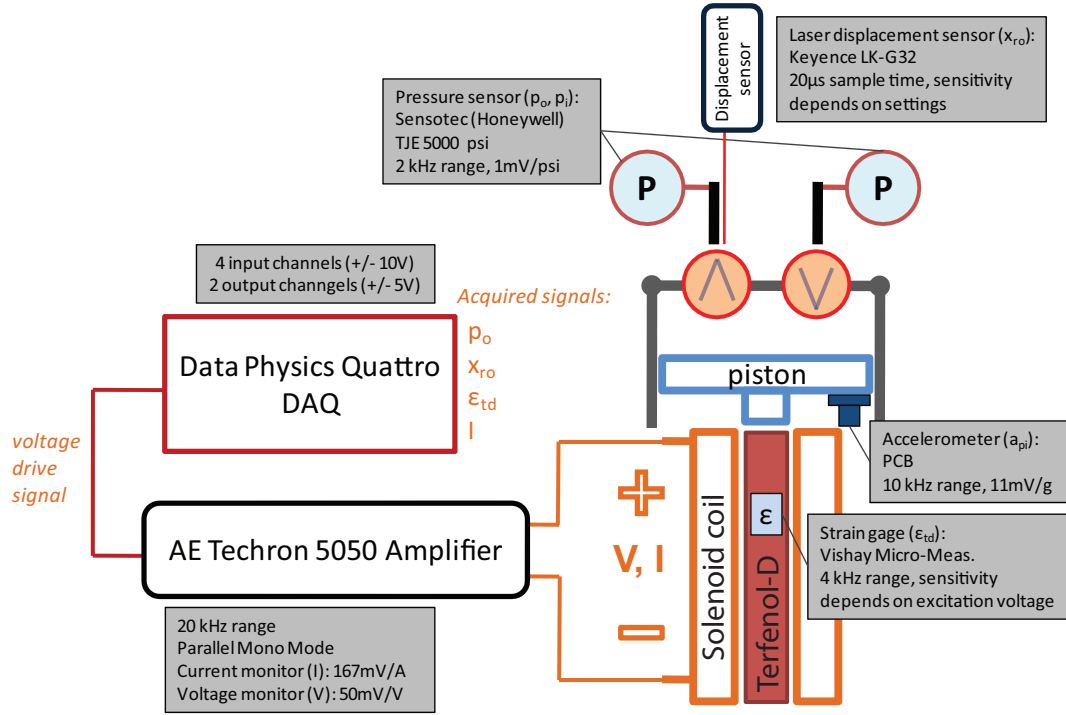


Figure 4.8: Schematic of full setup for data acquisition from smart material pump. The setup has capability to measure: solenoid coil current,  $I$ , and voltage,  $V$ , Terfenol-D rod strain,  $\epsilon_{td}$ , outlet pressure,  $p_o$ , and inlet pressure,  $p_i$ , piston acceleration,  $\ddot{x}_p$ , and outlet rectification valve motion,  $x_{ro}$ .

## CHAPTER 5

### RESULTS AND DISCUSSION

#### 5.1 No-Flow Pressure Simulation and Testing

The no-flow operating condition for the smart material pump is shown in Figure 2.10 in section 2.5.2 and characterizes the maximum pressure the pump can produce. This condition, which is easy to implement in simulation, gives a repeatable test under which to characterize the Terfenol-D. The system model presented in chapter 3 is simulated under no-flow conditions by increasing the actuator mass,  $m_{act}$ , to  $1 \times 10^{12}$  kg.

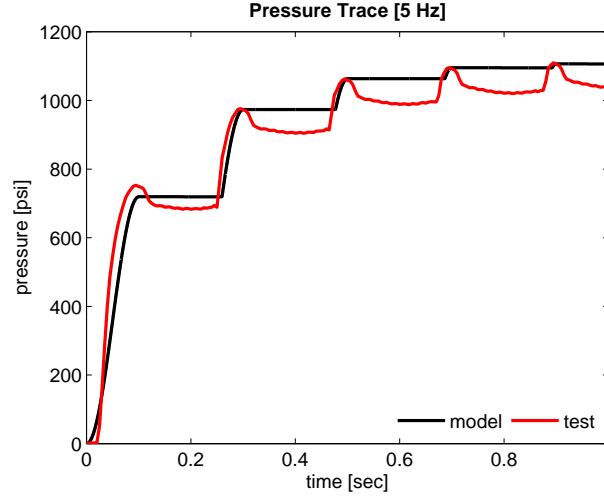
##### 5.1.1 No-Flow Pressure Trace

Figure 5.1 presents the model simulations along with time domain pressure traces from the Terfenol-D pump at 5 and 10 Hz pumping frequency. The input to the solenoid coil is 20 amp peak-to-peak sinusoid with a 10 amp bias. The pressure trace magnitude matches the data from the pump, but does not capture the brief pressure drop following the peak of each cycle. This event is referred to as pressure recoil and is physically explained by the pressure drop associated with a small amount of fluid backflow into the pumping chamber. It follows that there should be a slight time delay

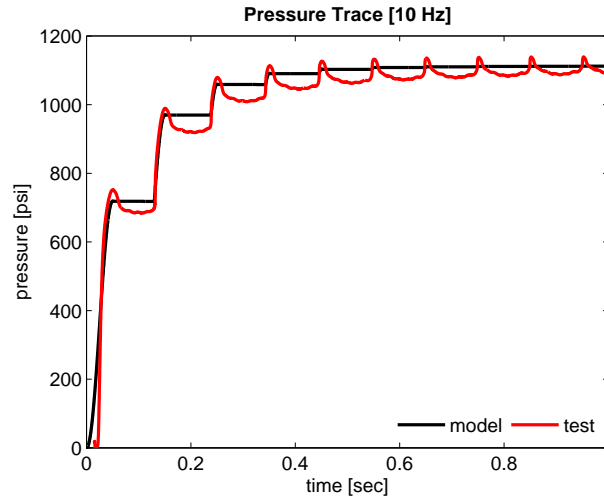
between the beginning of the negative cycle of the pumping piston and the outlet reed valve closing allowing backflow. Figure 5.2 shows the pressure trace at 25 and 50 Hz along with pump data. The reed valve dynamics and fluid-structure coupling capture the pressure recoil behavior at these frequencies. The results presented here validate the parameters selected for the reed valve model, presented in Table 3.5 in section 3.3, and the resistance curve, shown in Figure 3.7 in section 3.2.4. While the simple, single degree-of-freedom model does not capture the pressure recoil phenomenon in the low frequency range up to 10 Hz, the correlation at higher frequencies establishes the dynamic valve model and fluid-structure coupling. The following section presents results in the frequency range up to 1200 Hz. A stronger validation of the valve model is obtained using the no-flow simulation condition which accounts for not only the dynamics of the valve model but also the dynamics of the mechanical and fluid domain of the system.

### 5.1.2 No-Flow Pressure Response

The results presented in the previous section (5.1.1) illustrate the Terfenol-D pump's ability to generate and store pressure at low frequencies ( $< 50$  Hz). The outlet rectification valve is stiff enough and has a low enough mass to respond quickly to the pressure of the flowing fluid by closing during the refill stage of the pump. The discussion in section 3.1.3 described the effects that add equivalent mass and damping to the moving reed valve. This reduces the resonance and thus the usable operating range captured by the reed valve in the system model. Time domain, no-flow testing of the Terfenol-D pump was performed and the results were originally given in reference [42]. The input current is 4 amps peak-to-peak with a 2 amp bias. The reed



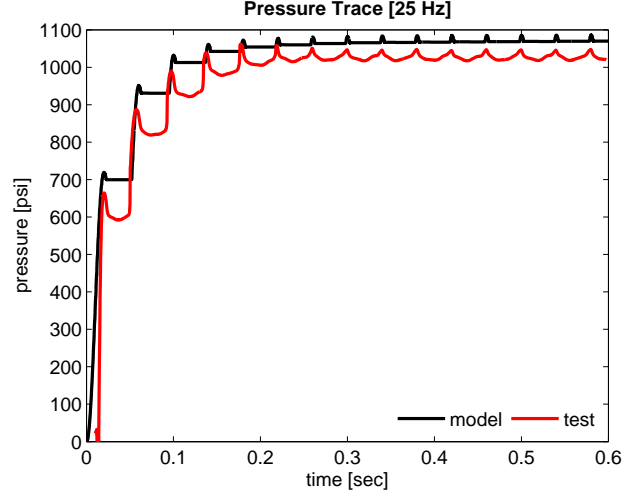
(a)



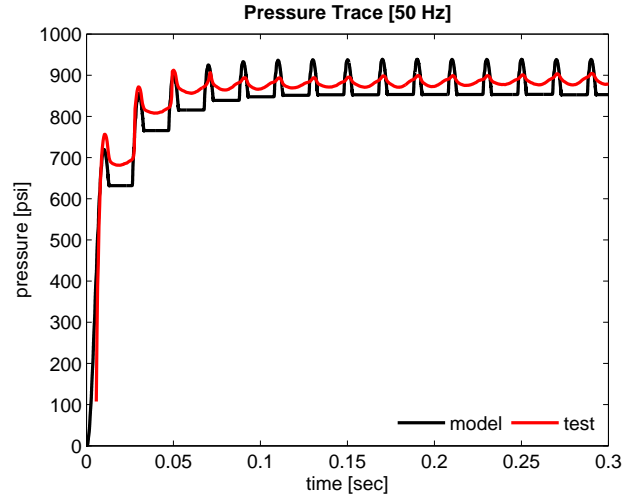
(b)

Figure 5.1: Measured and simulated no-flow pressure trace for the Terfenol-D pump at (a) 5 and (b) 10 Hz. The solenoid coil input is a 20 amp peak-to-peak current with a 10 amp bias.

valve model parameters are further validated by comparing simulation results up to the maximum frequency acquired from the Terfenol-D pump. The frequency domain pressure response results are generated using either time domain simulations or test data acquired at discrete frequencies. A metric termed ‘stored pressure’ is employed



(a)



(b)

Figure 5.2: Measured and simulated no-flow pressure trace for the Terfenol-D pump at (a) 25 and (b) 50 Hz used to validate the parameters of the rectification reed valve model and fluid-structure interaction.

for the model simulations and test data. Stored pressure is a measure of the average amount of pressure stored by the pump over the total run time given by:

$$p_{str} = \frac{1}{T} \int_0^T p_o(t) dt, \quad (5.1)$$

where  $T$  is the total run time. The test data is used to verify that the stored pressure metric gives very nearly the same value of steady state (hold) pressure at each frequency. As the time domain simulations of pressure response at frequencies above 100 Hz do not exhibit the ideal pressure hold behavior seen at low frequencies, the stored pressure is used as an equivalent metric to assess the response of the pump under no-flow conditions at high frequencies.

Figure 5.3 presents the results of the system model simulation under no-flow conditions up to 1.2 kHz along with test data and ideal valve simulation results. System model simulations with ideal valve behavior (no dynamics) are shown to emphasize the effect of rectification valve dynamics on the response of the pump. The system model is implemented in state-space and utilizes binary (ideal) valve logic dependent upon the pressure difference across the valve [42]. The test data shows the pump is able to produce around 200 psi of pressure up to 20 Hz at which point the maximum pressure quickly drops to 50 psi where it holds constant up to 1200 Hz. The system model simulations follow this trend for the stored pressure given in equation (5.1). The ideal valve system response highlights the effect of the rectification valves on the system response. The ideal valve will open and close in sync with the flow produced by the actuating stroke of the pumping piston displacing the small burst of high pressure fluid to the pump outlet. The dynamic valve model captures the fluid-structure coupling that limits the ability of the pump to hold pressure at the outlet. In this framework the valve behavior is no longer independent of the dynamics of the fluid flow, pressure, and piston motion resulting in non-ideal response. As frequency increases so does the time lag of the outlet valve due to its inertia and damping. The pressure stored at the outlet will be proportional to the amount of fluid

the pump can store past the outlet valve. This time lag allows fluid to backflow into the chamber thus reducing the maximum pressure the pump can hold at a given frequency. The model framework presented in chapter 3 for rectification valve dynamics is validated by the time domain pressure trace results presented in the previous section (5.1.1) and is further validated by capturing the non-ideal valve behavior under no-flow conditions. In each case the simulated data is correlated to test data acquired from the Terfenol-D pump. Whole system model validation for the dynamic valve model is superior to simply considering the valve alone as it considers the dynamics of the system applied to the valve during operation.

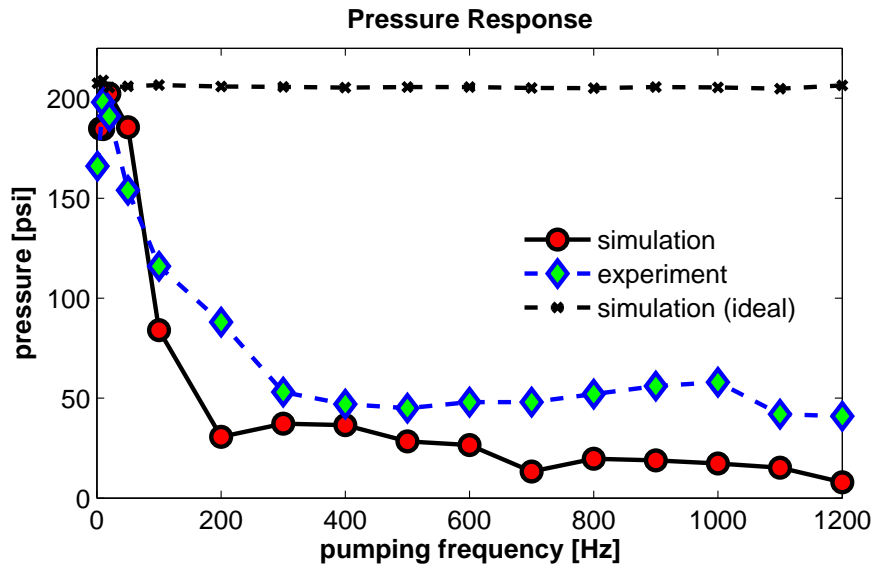


Figure 5.3: Results of time domain tests and simulations for the Terfenol-D pump under no-flow conditions from 1 to 1200 Hz. The “ideal” results are for a system model simulation absent of valve dynamics. The metric for evaluation is the average amount of pressure stored at each frequency by the pump and is given in equation (5.1).

## 5.2 Loaded Actuator Simulation

### 5.2.1 Characterization of Prototype EHA

In many practical applications the smart material EHA will need to drive an inertial load. Loaded actuator simulation evaluates the performance of the Terfenol-D pump and fluid rectification valves in the context of moving an inertial load attached to the output cylinder piston (see Figure 3.2). The smart material EHA motion is defined as the displacement of the output piston and the EHA velocity is the time rate of change of this motion. The Terfenol-D pump must be able to supply high pressure flow to the output cylinder and the reed valves are required to efficiently rectify that flow delivering it to the cylinder. The loaded case was discussed in section 2.5.1 and is shown schematically in Figure 2.10(c). Simulation results are presented here to fully illustrate the effect of rectification valve dynamic response on the performance of the actuator. Equation (3.39) shows that theoretically the fluid flow rate created by the smart material pump is linearly proportional to the pumping frequency. It is this high pressure flow that drives the motion of the output piston and so therefore the velocity of the smart material EHA should be linearly proportional to the input frequency. The model assumes the smart material EHA is working against a purely inertial load of 50 lbs. The time domain model is run for a specified number of cycles at a given frequency. The average actuator velocity for a given run is calculated similarly to the stored pressure in equation (5.1) by averaging the total velocity trace for the entire cycle given by:

$$\bar{v}_{act} = \frac{1}{T} \int_0^T v_{act}(t) dt. \quad (5.2)$$

Figure 5.4 shows simulation results for a pumping frequency of 10 to 3500 Hz for the case of ideal rectification valve behavior and fluid-structure coupled valve dynamics. The simulations are limited to 3500 Hz due to significant contributions of the valves 2<sup>nd</sup> mode of vibration past this frequency which can not be captured in the single degree-of-freedom model. The results are consistent with the conclusions presented in reference [42] where the 0.005 in thick reed valves have a bandwidth of approximately 1200 Hz. This conclusion was based on dynamic characterization of the Terfenol-D pump which showed deviation in the pressure response past 1200 Hz for the case of the reed valves installed and the valves removed. The ideal valve behavior simulation results violate this trend as actuation velocity increases nearly linearly with pumping frequency for the range investigated. The simulation results capture the dynamic effects of the Terfenol-D pump, chamber fluid mass, and fluid rectification valves on the theoretical performance of the actuator. At low frequency the outlet fluid rectification valve is able to respond in a favorable way allowing flow from the chamber to the hydraulic cylinder and blocking flow in the opposite direction. The relative motion between pumping piston and the inlet and outlet valves permits fluid rectification in a very effective manner. As frequency increases, the fluid and structural loading effects on the valves, captured by the effective mass and damping of the valve, begin to affect the dynamics in such a way that the pump can no longer deliver fluid effectively to the output cylinder. The result is a reduction in actuator motion illustrated in Figure 5.4 for an inertia loading of the actuator. The velocity increase up to 1200 Hz is not perfectly monotonic primarily due to the method of calculating the velocity at a given frequency shown in equation (5.2). Because the integral of the time domain actuator velocity is averaged over the total run time,

which is much less than unity for all cases, a small deviation in the integral between two frequencies will be magnified. The resonance in actuator velocity at 2600 Hz is due to the result of the frequency content of the forcing on the valve. The forcing will have a major contribution of frequency content at the driving frequency. However side bands also exist at twice the resonance of the valve (1360 Hz) brought about by the nonlinear contact due to the valve seat. At a pumping frequency of 2600 Hz side bands of the valve forcing lie at the resonance of the valve causing ideal motion and phasing. This behavior is not verified experimentally and should be investigated further to determine if this condition arises from physical effects or modeled effects.

The simulations results presented in Figure 5.4 indicate a reversal of actuator direction past 1200 Hz. This result highlights the concept of phase in the frequency response of the valve. Figure 5.5 shows normalized simulation results at 1420 Hz for the flow rate provided by the piston ( $q_{pi} = A_{pi}\dot{x}_p$ ), flow through the outlet valve ( $q_{oc}$ ), outlet valve motion ( $x_{ro}$ ), and outlet valve resistance ( $R_o$ ). The lag between piston motion (equivalent to  $q_{pi}$ ) and outlet valve response is large at this frequency due to the dynamics of the Terfenol-D pump, outlet valve, and fluid circuit. The valve displacement lags the piston flow rate by nearly 30% of the cycle at this frequency. The physical implication of this is the outlet valve opening (resistance of the outlet valve dropping) as the pump piston is trying to pull fluid into the chamber. The modeled phenomenon is effectively a reversal of actuator direction. This result is undesirable and is due to the dynamic and relative phasing of the rectification valves, Terfenol-D pump, and hydraulic circuit. The ideal valve behavior results, which exclude valve dynamics from the simulation, do not show this effect.

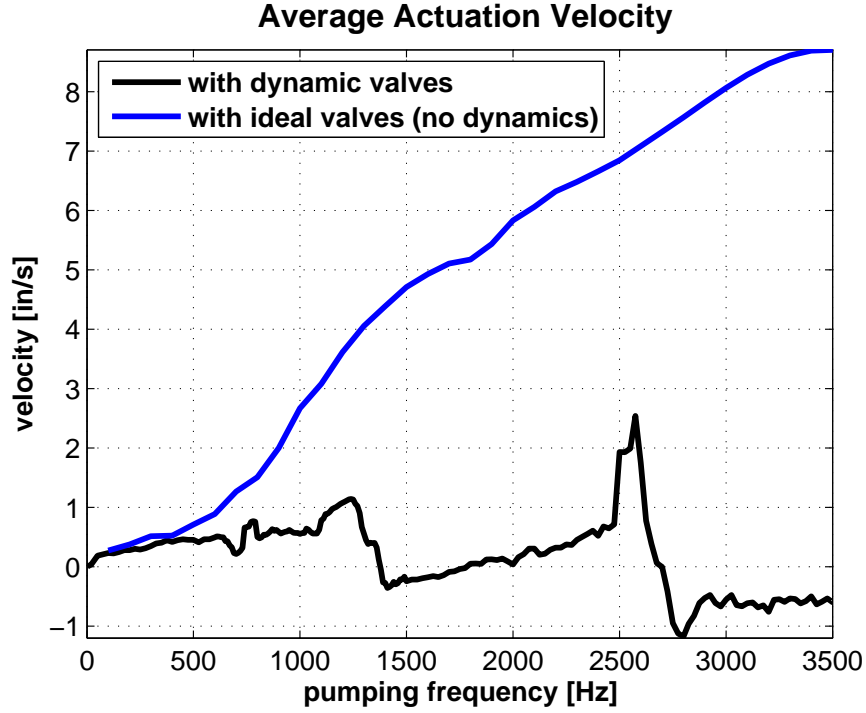


Figure 5.4: Simulation results for pumping frequencies from 10 - 3500 Hz for the Terfenol-D pump attached to a hydraulic cylinder and piston and loaded inertially to create actuation. The dynamic response of the rectification valves limit the ability of the pump to deliver fluid to the cylinder at frequencies above 1200 Hz and thus attenuates actuator motion.

### 5.2.2 EHA Velocity Bandwidth Investigation

It is advantageous to operate in certain frequency ranges for the smart material pump to improve response and reduce the amount of input energy. As part of this study the resonance of the fluid rectification reed valves is examined as a design parameter for bandwidth tuning. The implication of valve phasing was discussed in the previous section. If the valve passes through its first resonance and, for the single degree of freedom model, phase switches by 180 degrees accentuated backflow (recoil) will occur. Backflow severely limits the performance of the actuator. The simulation

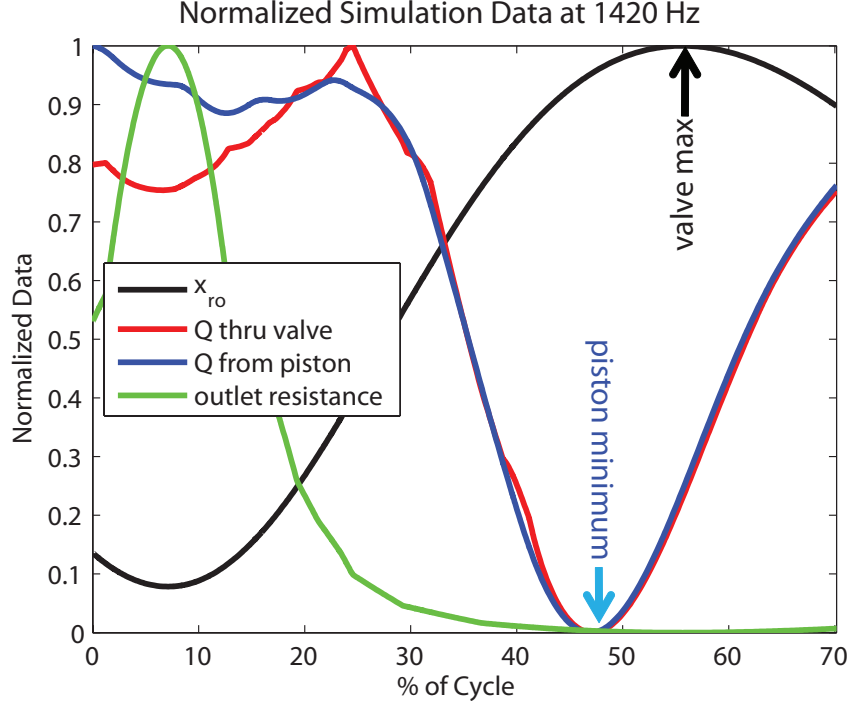


Figure 5.5: Normalized data for piston induced flow rate ( $q_{pi} = A_{pi}\dot{x}_p$ ), flow rate through the outlet valve, valve motion, and valve resistance vs. percentage of pumping cycle at 1420 Hz. The resulting simulation highlights the effect of phase mismatch between the valve and piston motion causing actuator reversal shown as negative velocity in figure 5.4.

is run with a valve stiffness 3 times the original stiffness and 50% of the original mass resulting in a factor of 2.45 increase in resonance. The parameter variation extends the resonance of the valve and by doing so the usable bandwidth of the actuation system. Figure 5.6 shows the simulations results for the EHA working against the same inertial load (50 lbs.) as presented in section 5.2 for pumping frequency range from 10 to 3500 Hz. The increased valve resonance allows the actuator to produce positive velocity up to 3100 Hz where high frequency pumping results in a maximum velocity increase of 1.5 times that of the baseline case.

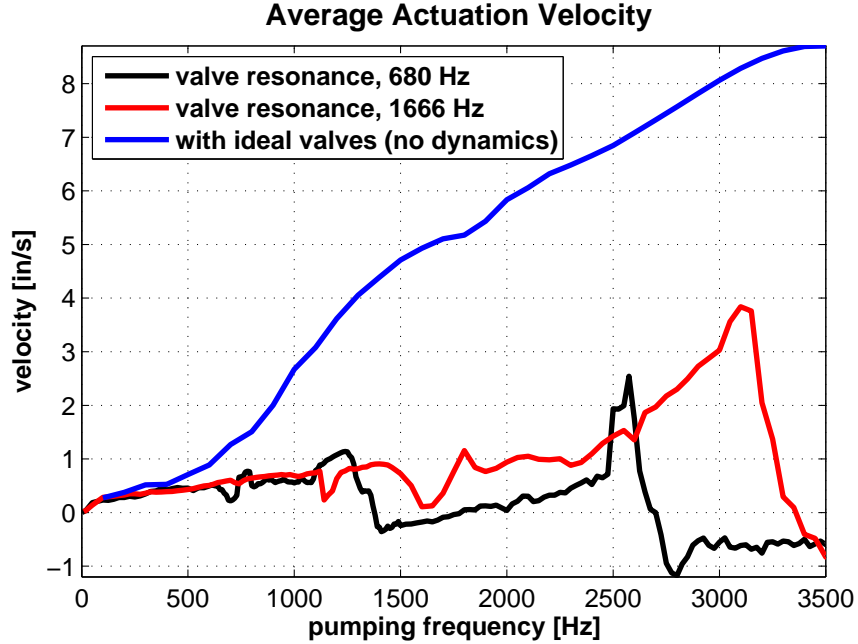


Figure 5.6: Simulation results for pumping frequencies from 10 - 3500 Hz for the Terfenol-D pump attached to a hydraulic cylinder and piston and loaded inertially to create actuation. The valve resonance is increased by a factor of 2.45 over the baseline values presented in Figure 5.4 resulting in actuator bandwidth expansion and a higher maximum velocity at actuator resonance.

### 5.3 Modeling Discussion

Discussion on the method and implications of implementing a model for the fluid rectification valve dynamics in a smart material EHA model is given in this section. The information here is meant to support the discussion of the model and the results presented in previous sections.

In a very general sense the fluid rectification valve model is comprised of two parts which interact in a coupled way in an attempt to fully capture the physical effects that impact valve dynamic behavior. The first is the mechanical model. It has been presented that fluid loading and proximity effects add equivalent mass and

damping to the valve model. An approximation of these parameters is made based on an analytical expression (equation (3.20)) and the experimental results of a relevant study of cantilever beam response [36]. This information provides guidance for the final mechanical model parameters, but does not quantify them. Steady state finite element simulations of the port and rectification valve give an effective fluid resistance for the valve at different tip displacements. The position of the valve is governed by the equation of motion for the mechanical model and is the independent variable in the expression for valve fluid resistance determined by the FE simulations. This describes one path in the fluid-structure coupling; that the position of the valve determines the fluid resistance of the valve. The second path in the coupling is the upstream and downstream pressures driving the motion of the valve. The pressures will depend upon the valve fluid resistance and this captures the coupling between the mechanical and fluid domain for the valve model. Finally the mechanical parameters are quantified by correlating the measured no-flow pressure trace of the Terfenol-D pump to the simulation results. This establishes confidence in the model using a holistic approach accounting for all the dynamics of the system.

The dependence of valve fluid resistance and valve motion are developed from the FE model solution for pressure drop and flow rate through the valve and equation (3.27). The results of this simulation, given in Figure 3.7, do not completely define the range of fluid resistance values the valve can take in the model. The pressure differential across the valve can become relatively large during operation particularly for no-flow conditions and the outlet valve. This is due to the outlet pressure being held at a high value while the pump piston retracts pulling fluid into

the chamber and returning the chamber pressure to the system bias in a no-flow condition. During intake, if the outlet valve is closed, flow should not enter the chamber from the outlet port. At the operating pressures of the pump, the valve's 'closed' fluid resistance must be high relative to the FE simulation results to eliminate large pressure recoil in the model. For this reason the closed valve fluid resistance is several orders of magnitude higher than highest resistance determined from FE simulations. Additionally, to ensure the minimum resistance is limited to a reasonable value an artificial point on the resistance versus valve position relationship ( $R(x)$ ) is set such that the resistance is unable to take a lower value. These two points, minimum and maximum, are not results of FE simulations for effective valve resistance but necessary bounds for successful valve model implementation. The implication of such a large 'jump' in valve fluid resistance is the potential for high oscillation, valve flutter at low frequencies, low valve stiffness, and mass. At low frequencies the valve is able to respond with little time lag to the changing pressure differential. If the valve has a low value of stiffness, slight changes in driving pressure difference will significantly increase or decrease valve displacement. Furthermore a low valve mass resulting in minimal inertial lag leads to the valve being more responsive to the driving pressure. As pressure in the chamber increases the valve cracks open and the outlet pressure attempts to equalize to the chamber. However due to the governing physical effects the outlet pressure will lag the chamber during the pressurizing stroke of the piston, which causes the pressure differential driving outlet valve motion. The variation in pressure differential will naturally fluctuate during the cycle and at high chamber pressures induces relatively large oscillations of the valve. The softer and lighter valve will deflect more and respond quicker to the pressure fluctuations compared to

a stiffer and heavier valve. High amplitude oscillations can occur if the valve position is located in a region of large negative slope on the  $R(x)$  curve because even small fluctuations cause large changes in fluid resistance leading to increased fluctuations in pressure. This behavior is similar to positive feedback as the small valve oscillations create large changes in resistance leading to high pressure fluctuations leading to larger valve oscillations. This behavior is a result of the valve model implementation but not completely unphysical. Valve flutter is a common design consideration in passive valve systems and occurs due to either a sudden (step) force causing an oscillating step response or from negative pressure building up in the valve seat due to Bernoulli effects [51]. In some cases, where damping and mass are low, this can result in oscillating amplitudes (flutter) equal to or higher than the forced opening of the valve. While the model is not formulated to capture these specific effects, it should be noted that the valve flutter seen at low frequency, high current input simulations are not completely without physical basis.

## 5.4 In Situ EHA Characterization

The method of measuring outlet reed valve motion described in section 4.3 is employed to give the results presented in this section. The no-flow condition for the Terfenol-D pump is used to give a repeatable testing state for the acquisition of outlet valve motion. The current through the solenoid coil for the 10 and 20 Hz testing is a 20 amps peak-to-peak current with a 10 amp bias. Outlet rectification valve measured displacement at 10 Hz is presented in Figure 5.7(a). Figure 5.7(b) gives the normalized measured reed motion, outlet pressure, and Terfenol-D strain. The maximum pressure differential generated by the pump during testing is 680 psi

at a maximum Terfenol-D strain of  $850 \mu\epsilon$ . As discussed in section 4.3 the reduced pressure performance is due to added compliance in the seal of the insert piece. The measured results indicate that the valve is very responsive during the positive (pressurizing) stroke of the pump. It is evident by examining the first cycle shown in Figure 5.7(b), where pressure recoil is very prevalent, the valve displacement ‘closing’ slope has two regions. The first region has a relatively small slope indicating the valve is ‘hanging’ open as the pumping piston retracts. This behavior allows fluid to backflow into the pumping chamber creating pressure recoil. The second region is characterized by a steeper negative slope indicating the valve is responding to a larger pressure differential pushing the valve closed. At the end of this second region the valve displacement abruptly reaches a ‘zero’ position indicating the valve has closed against its seat. At this time in the pressure trace the recoil behavior stops and a small amount of pressure drop is seen as the first cycle ends indicating a small amount of fluid is able to backflow through the outlet valve in its closed position. As the pump reaches the stall condition in the later cycles, the valve opens and closes at a much higher rate, allowing less fluid to backflow into the pumping chamber and reducing pressure recoil. The insert motion is superimposed on the valve measurement and is the source of apparent ‘valve float’ in the measured results. The results for 10 Hz are compensated by shifting the valve data by measured insert motion.

Figure 5.8 shows measured outlet valve displacement and outlet pressure trace at a pumping frequency of 20 Hz. The solenoid coil current, driving the motion of the Terfenol-D, is reduced from 20 amps to 8 amps peak-to-peak from test 1 to test 2. The pressure trace shows the expected reduction of no-flow pressure for test 2 due to the reduction in total input energy. This test was performed to illustrate the

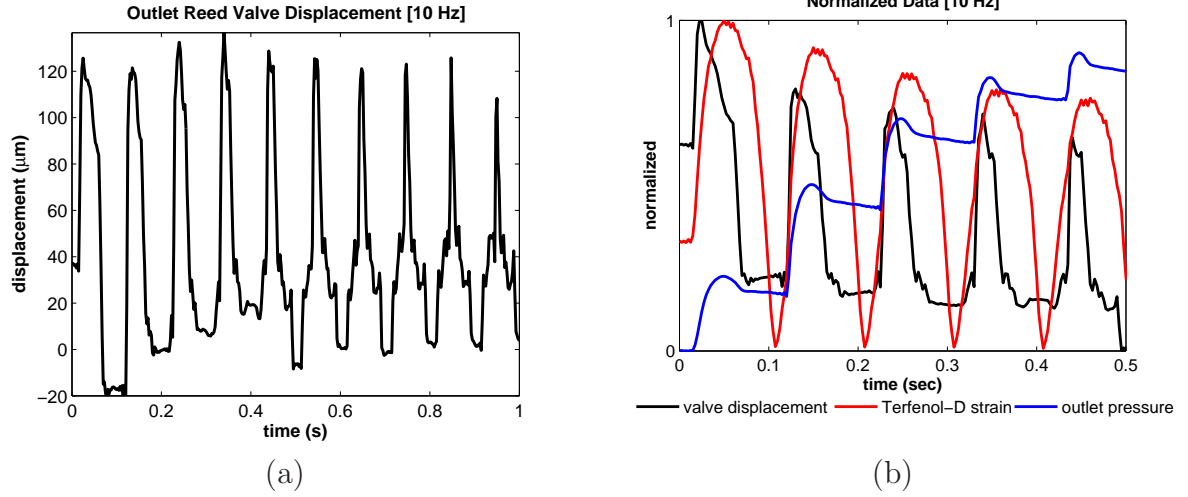


Figure 5.7: Terfenol-D pump response under no-flow conditions at 10 Hz. (a) In situ displacement time trace for the outlet reed valve; (b) normalized outlet reed motion, Terfenol-D pump outlet pressure, and Terfenol-D strain at 10 Hz pumping frequency for 5 cycles.

similarity in the valve displacement trace, particularly in the steady-state region, for both cases. The driving pressure of the outlet valve displacement is the difference in measured outlet pressure and the unmeasured chamber pressure. This result indicates that this pressure difference is nearly the same for each case even though the outlet pressure trace is not. The implication of this result is that the way in which the high pressure flow cracks open the outlet valve and exits the chamber is nearly the same for two cases where the steady state pressure differs by nearly 50% and therefore is independent of the steady state pressure and solenoid current amplitude in this range. Figure 5.9 shows the normalized valve displacement with Terfenol-D strain and outlet pressure for test 1 shown in Figure 5.8. The results are similar to the 10 Hz data in that the valve is responsive to the positive stroke and has two regions of negative slope leading to pressure recoil.

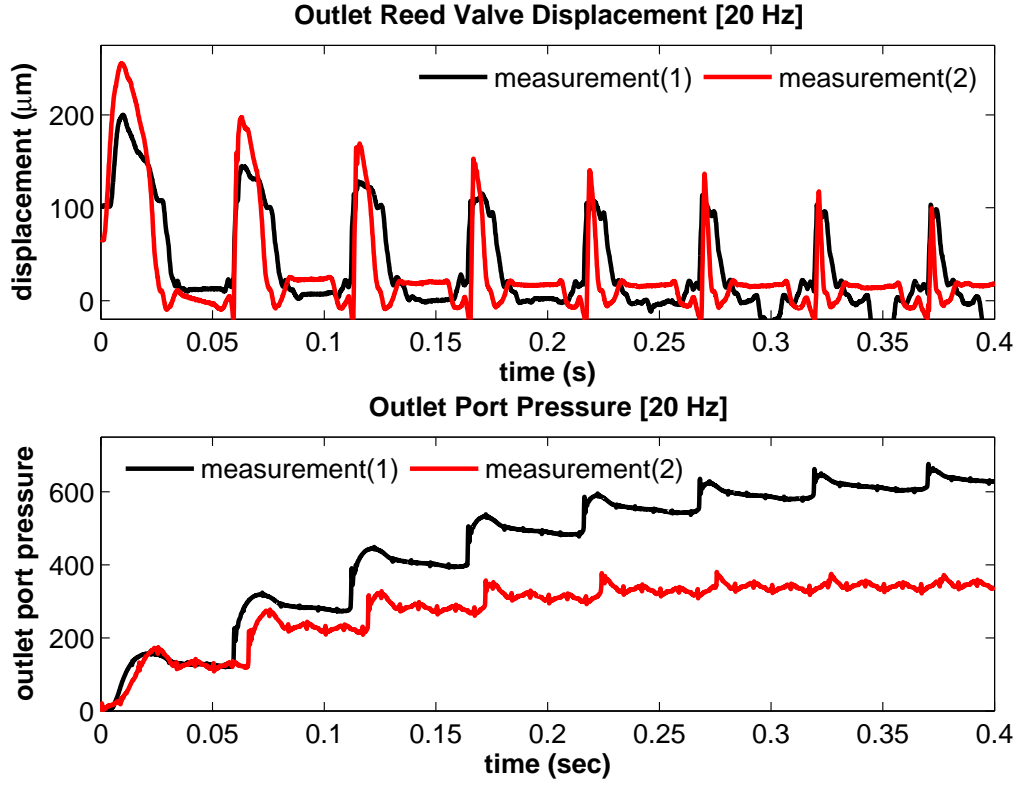


Figure 5.8: Terfenol-D pump response under no-flow conditions at 20 Hz. (top) In situ displacement time trace for the outlet reed valve at 20 Hz pumping frequency for two measured cases of different input amplitude to the solenoid coil. (bottom) In situ outlet pressure traces showing different steady state values.

Figure 5.10(a) shows the steady state measured outlet valve displacement at a pumping frequency of 100 Hz. The input current is reduced from 20 to 5 amps to ensure the Terfenol-D rod accelerations are kept in the range of safe operation. Difficulties in measurement discussed in section 4.3 limited the capture of data for the initial rise of no-flow pressure. The steady state displacement of  $650\text{ }\mu\text{m}$  is much higher than that seen at 10 and 20 Hz. Each test at 10 and 20 Hz showed a region of flat (zero) displacement response that indicated the valve was contacting the seat.

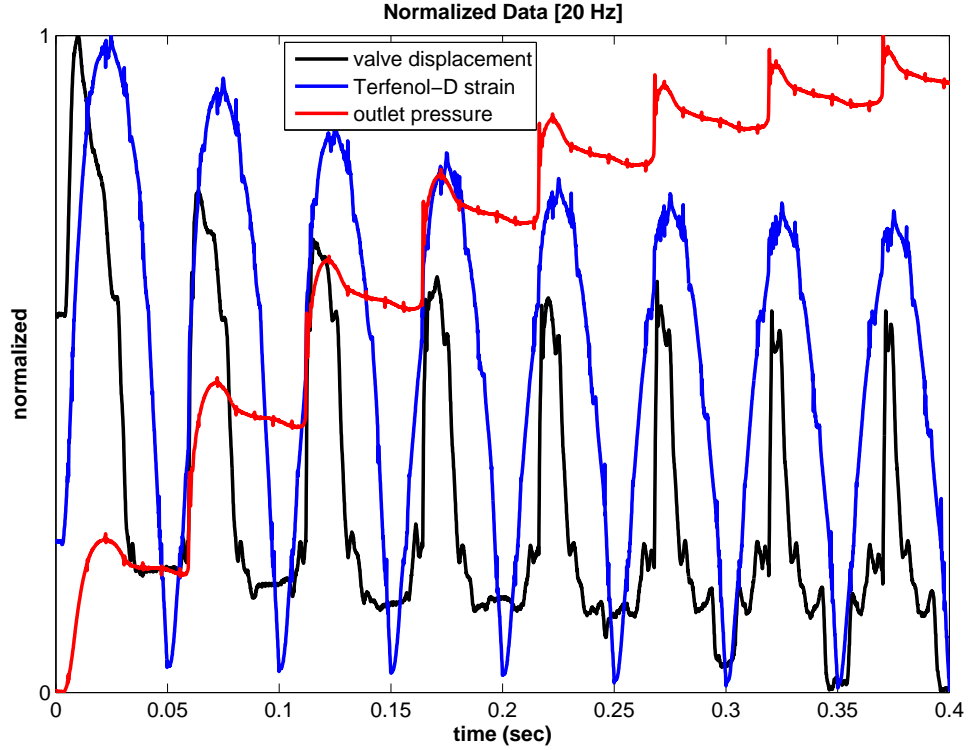


Figure 5.9: Terfenol-D pump response under no-flow conditions at 20 Hz. Normalized outlet valve motion, outlet pressure, and Terfenol-D strain at 20 Hz pumping frequency for 8 cycles. The outlet valve is responsive to the pressurizing stroke of the piston showing two regions of negative slope during piston retraction leading to pressure recoil and backflow.

The data at 100 Hz does not show the valve seating. Normalized valve displacement and solenoid current are shown in Figure 5.10(b). The results of in situ testing at 100 Hz illustrates the outlet valve lag behavior that is inherent to passive valves. At any frequency the outlet pressure will lag the chamber pressure due to the response of the valve. Furthermore the outlet valve will lag the difference in outlet and chamber pressure due to valve's mass, stiffness, and damping as well as the loading from the fluid and proximity effects. This lag is shown in Figure 5.10(b) and highlights the need

for modeling the fluid-structure interaction of the rectification valve and its frequency response. Figure 5.10(a) indicates the valve does not seat at this frequency. The valve lags the driving force created by the difference in chamber and outlet pressure to such a degree that the valve does not seat at the conclusions of one cycle before the driving pressure from the next cycle forces it open again.

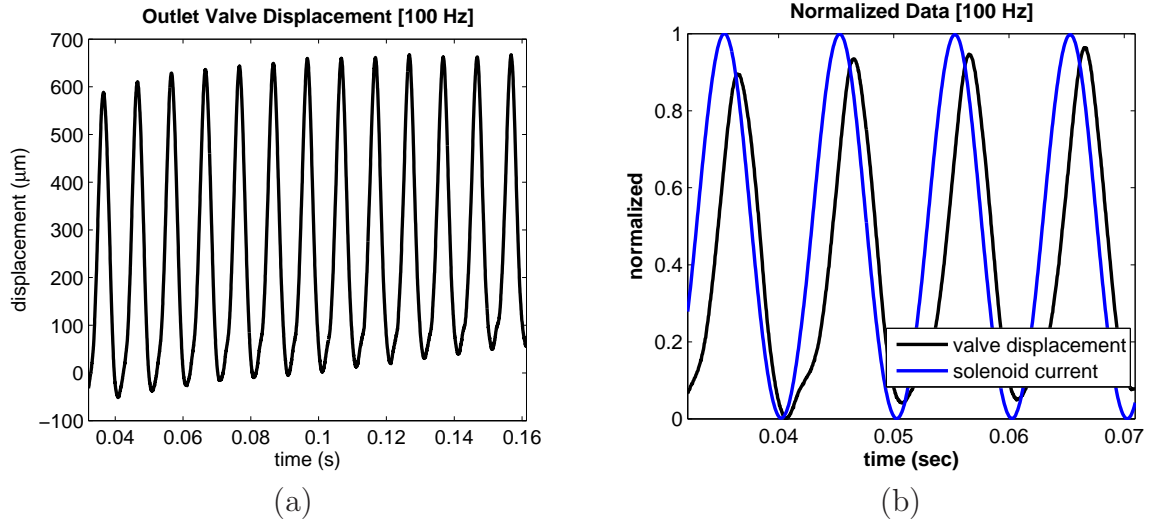


Figure 5.10: Terfenol-D pump response under no-flow conditions at 100 Hz. (a) In situ displacement trace for the outlet reed valve (b) normalized outlet reed motion and solenoid current at 100 Hz for 5 cycles.

## CHAPTER 6

### CONCLUDING REMARKS

#### 6.1 Summary of Results and Contribution

This research presents a fluid rectification valve dynamic model and numerical implementation for a magnetostrictive pump as well as a novel technique for in situ characterization of smart material actuation systems. The model is capable of predicting the time domain pressure response of the pump up to 1200 Hz in a no-flow condition. A single degree-of-freedom lumped-parameter model represents the fluid rectification valves in the mechanical domain of the system model. Fluid loading and proximity effects are captured by adding equivalent mass and damping to the reed valve mechanical model. This results in a flatter resonance peak occurring at a lower frequency relative to the frequency response of the valve in air. Three dimensional, fluid dynamic finite element simulations of the fluid port and reed valve in the head of the Terfenol-D pump quantify the effective resistance to flow at valve tip displacements from 2 to 1024  $\mu\text{m}$ . The FE simulation results provide the information to couple the motion of the valve in the mechanical domain to the valve's effective resistance to flow in the fluid domain. The mechanical model for the rectification valve, along with the coupling to the fluid domain, fully defines the fluid-structure coupling

of the valve in the model. System model simulations for an inertial loading of the EHA illustrate the effect of rectification valve dynamics on the performance of the actuation system. The simulated actuator velocity violates the theoretical prediction of linear proportionality to pumping frequency as the simulation results show attenuated performance above 1200 Hz. It is shown that extended velocity bandwidth and performance of the actuator is obtained by increasing the resonance of the valve. A novel method for in situ characterization of the pump is presented. In situ pump characterization under no-flow conditions at pumping frequencies of 10, 20 and 100 Hz is presented; including outlet valve displacement measurements. The results validate the novel method for in situ system characterization, reveal behavior for pump and rectification valve response, and highlight short-comings in the implementation that can be addressed in future iterations.

The contribution of this work is the dynamic modeling of a fluid rectification valve and implementation for a smart material pump driving an EHA. It is generally necessary to operate the pump at high frequencies to satisfy flow rate requirements. If the rectification valves achieve the desired flow rate at pump resonance, in the kHz range, the amount of output pressure per input current for the pump is dramatically increased. Therefore the capability to predict spectral response of the magnetostrictive pump and rectification valves enhances the system model as a design tool. Additionally the validation of the method of in situ measurement expands the possibilities for device characterization and thus the tools to develop high bandwidth valves and high performance actuation systems.

## 6.2 Research Opportunities

There are several pursuits that would further expand the capability of developing high performance rectification valves and improve the overall performance of smart material EHA systems. Increasing the degrees-of-freedom of the mechanical model for the reed-type valves would account more accurately for the physical occurrence of pressure distribution over the valve face. The percentage of the driving pressure over a given area of the valve could be varied in a multiple degree-of-freedom model which may be significant in dynamic behavior as a pressure distribution centered closer to the fixed end of the valve results in a higher apparent stiffness of the cantilevered valve. The higher order model would also capture higher modes of valve vibration. The fluid domain implementation for the rectification valve model would be made more physical by using a nonlinear orifice flow model rather than the linear resistance implementation presented in this work. The nonlinear orifice flow model would attenuate the flow through the valve at a high pressure differential rather than allowing flow rate to increase unbounded for increasing pressure. While the model presented here captures the expected trends of the actuator performance for high frequency operation it may be appropriate to include fluid inertia effects in the transmission lines of the circuit as these will be more significant at higher frequency oscillatory flows. Preliminary work has been done to implement the system model in the MATLAB Simscape environment. The model can be built in this environment using mechanical, fluid, and electrical elements joined in a similar way to the physical system. This increases the transparency of the SIMULINK system model and facilitates the implementation of the nonlinear orifice flow model for the valve and restricted passages in the hydraulic circuit.

The challenges of implementing the method for in situ valve measurement were discussed in section 4.3 and the results presented in section 5.4 illustrate the effect of these challenges. The next design iteration for acquiring valve motion data should focus on ensuring the viewing window (“insert”) does not move during testing and that it is highly transparent in the areas where the laser sensor must pass. This must not come at the expense of improper sealing at the boundaries of the viewing window. System compliance severely reduces pump performance and every effort should be made to ensure the modification to allow for valve measurement introduces zero additional compliance in the system.

Appendix B presents the results of displacement and force testing of cantilever unimorph samples using the magnetostrictive material Galfenol and several passive substrates. This work showed that for the particular combination of Galfenol and substrate tested the bimorph motion could not be effectively used as an active fluid rectification valve in the magnetostrictive pump. The smart materials and structures lab at Ohio State has previously developed working prototype magnetorheological (MR) fluid valves for fluid rectification in a smart material pump with good performance. While the question is currently still unanswered as to whether a system utilizing passive rectification valves can achieve favorable performance at pumping frequencies in the kHz range, active unimorph, MR, and needle-type valves should be considered as high performance replacements for their passive counterparts.

Some have considering using an array of micro-valves in place of the macro-scale rectification valves commonly used in smart material pumps [39, 40]. It is theorized that the higher stiffness and lower mass of these valves will significantly increase the usable range of frequency and that by arranging a high number of these in an array

the flow rate requirement of the pump can be satisfied. While the micro-fabrication techniques to produce these types of valves are relatively well developed compared to the valves themselves, the design and material for the micro-valve is critical in ensuring structural integrity and high performance and remains as the primary hurdle to implementing this technology. The impact of this technology for smart material pumps is significant enough to merit investigation especially in the case of reducing the size of the pump for small working-volume applications.

## APPENDIX A

### SYSTEM MODEL PARAMETER SUMMARY

Parameter	Value
Young's modulus of Terfenol-D rod ( $E_Y^H$ )	35 GPa
Cross-sectional area of Terfenol-D rod ( $A_{td}$ )	0.196 in <sup>2</sup>
Length of Terfenol-D rod ( $L_{td}$ )	4.5 in.
Stiffness of Terfenol-D rod ( $k_{td}$ )	38.8 MN/m
Stiffness of diaphragm ( $k_d$ )	2.15 MN/m
Effective mass of Terfenol-D transducer ( $m_{eff}$ )	0.124 kg
Damping ratio of Terfenol-D transducer ( $\zeta_{eff}$ )	0.09
Solenoid coil turns ( $N$ )	860
Piezomagnetic coupling coefficient ( $q$ )	$6.85 \times 10^{-9}$ m/amp
Pumping chamber height ( $h_{ch}$ )	0.05 in.
Pumping piston cross-sectional area ( $A_{pi}$ )	0.785 in <sup>2</sup>
Effective fluid bulk modulus ( $\beta_{eff}$ )	85 ksi
Mobil DTE25 hydraulic fluid density ( $\rho_f$ )	873 kg/m <sup>3</sup>
Mobil DTE25 hydraulic fluid viscosity ( $\mu_f$ )	0.0386 Pa-s
Lumped chamber fluid stiffness ( $k_f$ )	233 MN/m
Chamber fluid damping ratio ( $\zeta_f$ )	0.55
Chamber fluid mass ( $m_f$ )	$0.561 \times 10^{-3}$ kg
Reed valve thickness ( $t_r$ )	0.005 in
Reed valve stiffness ( $k_r$ )	6650 N/m
Effective reed valve damping ratio ( $\zeta_r$ )	0.1285
Effective reed valve mass ( $\bar{m}_r$ )	$0.3643 \times 10^{-3}$ kg
Reed valve fluid contact area ( $A_r$ )	0.0123 in <sup>2</sup>

Table A.1: System model parameters for the Terfenol-D pump, chamber, and rectification valves.

## APPENDIX B

### GALFENOL UNIMORPH TESTING

#### B.1 Experimental Setup

Galfenol is a magnetostrictive material and an alloy of gallium and iron. Galfenol unimorph samples provided by Etrema Products, Inc. are tested to characterize maximum displacement and force output. The unimorph samples are summarized in table B.1 and consist of a passive material (“substrate”) bonded to a Galfenol beam. The Galfenol is research grade 18.4 material that has been stress-annealed to NSWC-Carderock up to 45 MPa. The length and width of the substrate and Galfenol for each sample are 2 inches and 0.25 inches, respectively. The free length of the sample in the test stand is approximately 1 in. The thickness of the substrate and Galfenol is given in table B.1 as well as in the results.

Figure B.1 shows the test stand for activating the Galfenol unimorph samples. The magnetizing coil generates a magnetic field leading to magnetic flux that is directed by the circuit lengthwise through the beam. The lengthwise field induces elongation in the Galfenol beam. The substrate restricts the linear elongation inducing bending in the structure. The Galfenol unimorph samples are tested for potential implementation as active reed-type rectification valves for the smart material pump.

Substrate Material	Substrate Thickness [in]
Brass	0.015
Stainless Steel	0.005
Aluminum	0.060

Table B.1: Galfenol unimorph samples tested for free displacement and blocked force. Galfenol is 0.015 inches thick and all samples have a length of 2 inches and a width of 0.25 inches.

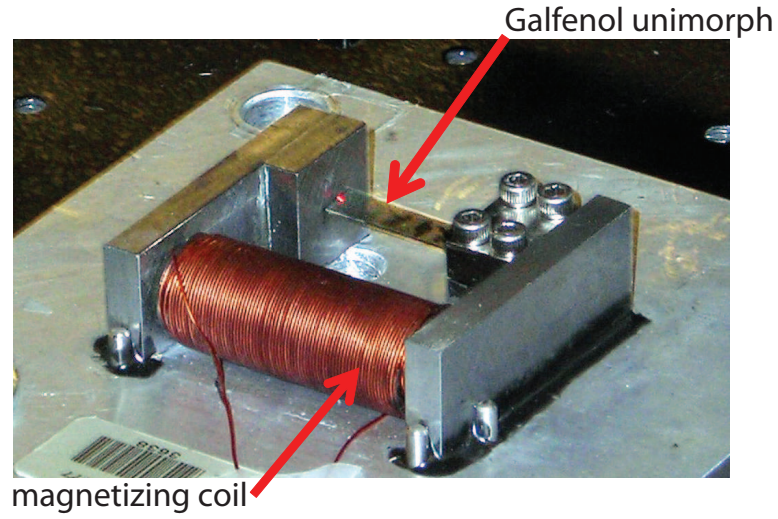


Figure B.1: Test stand for Galfenol unimorph sample testing.

## B.2 Quasi-static Testing Results

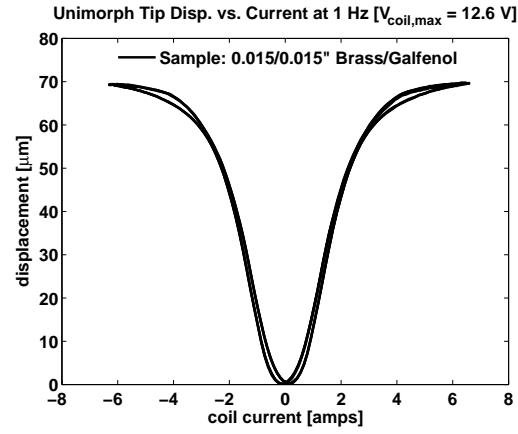
### B.2.1 Displacement Results

Figure B.2 shows the results for free displacement characterization of the Galfenol unimorph samples. The tests are performed at quasi-static frequencies of 0.2 and 1 Hz. Displacement is measured using the laser displacement sensor described in section 4.3.1. The thinnest substrate, stainless steel, provides the largest deflection

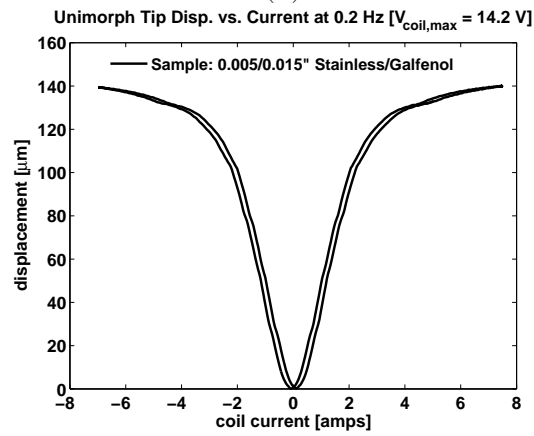
of 140  $\mu\text{m}$ . All samples show minimal hysteresis in the material and saturate near 8 amps of current through the magnetizing coil. The free displacement results of the stainless steel/Galfenol sample is encouraging as the displacement is near the measured results for valve displacement given in section 5.4.

### **B.2.2 Blocked Force Results**

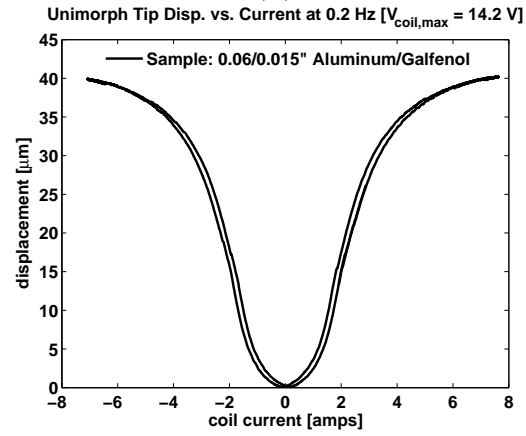
Figure B.3 shows the results for quasi-static characterization of the blocked force output for two samples. A load cell is placed near the end of the unimorph blocking the bending motion while measuring force applied by the tip of the beam. Force output is a critical metric for active valves as they would actuate against the high pressures of the working fluid. The results show a maximum of 50 milli-lb. produced by the aluminum/Galfenol sample. This sample produced the lowest amount of free deflection (40  $\mu\text{m}$ ) shown in figure B.2 (c). The stainless steel sample, which produced the largest deflection, was also tested but produced negligible force output and therefore is not presented here. While the results are encouraging, the force output of the Galfenol unimorphs is too low to merit further attention for active valves in the Terfenol-D pump. Other applications, which require control of fluid flow, may be better suited for this rapidly developing material. The results presented here indicate a tradeoff between free displacement and force output. Future work may revisit this type of active valve using Galfenol for this application if system requirements change or material performance improves.



(a)

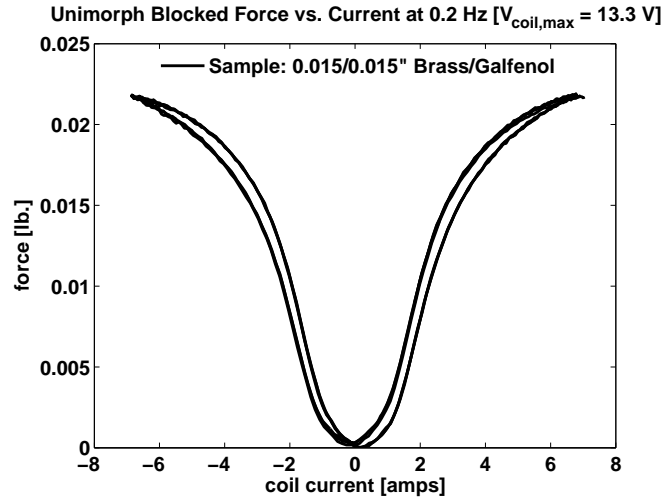


(b)

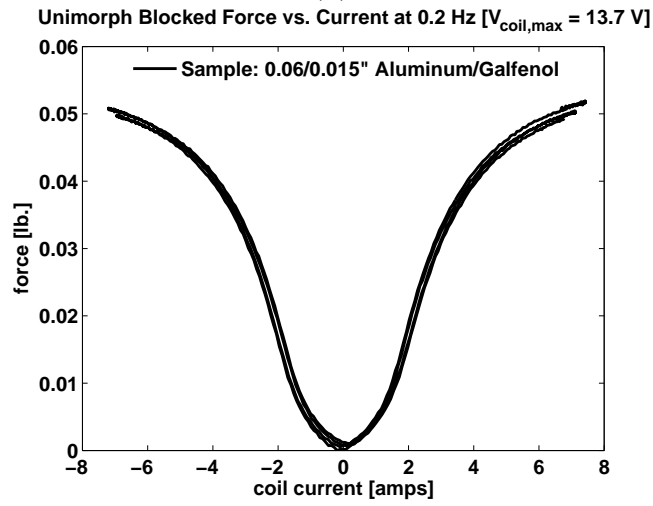


(c)

Figure B.2: Results of free displacement testing for Galfenol samples: (a) 0.015/0.015" brass/Galfenol (b) 0.005/0.015" stainless steel/Galfenol (c) 0.06/0.015" aluminum/Galfenol.



(a)



(b)

Figure B.3: Results of blocked force testing for Galfenol samples: (a) 0.015/0.015" brass/Galfenol (b) 0.06/0.015" aluminum/Galfenol.

## APPENDIX C

### DETAILED DRAWINGS

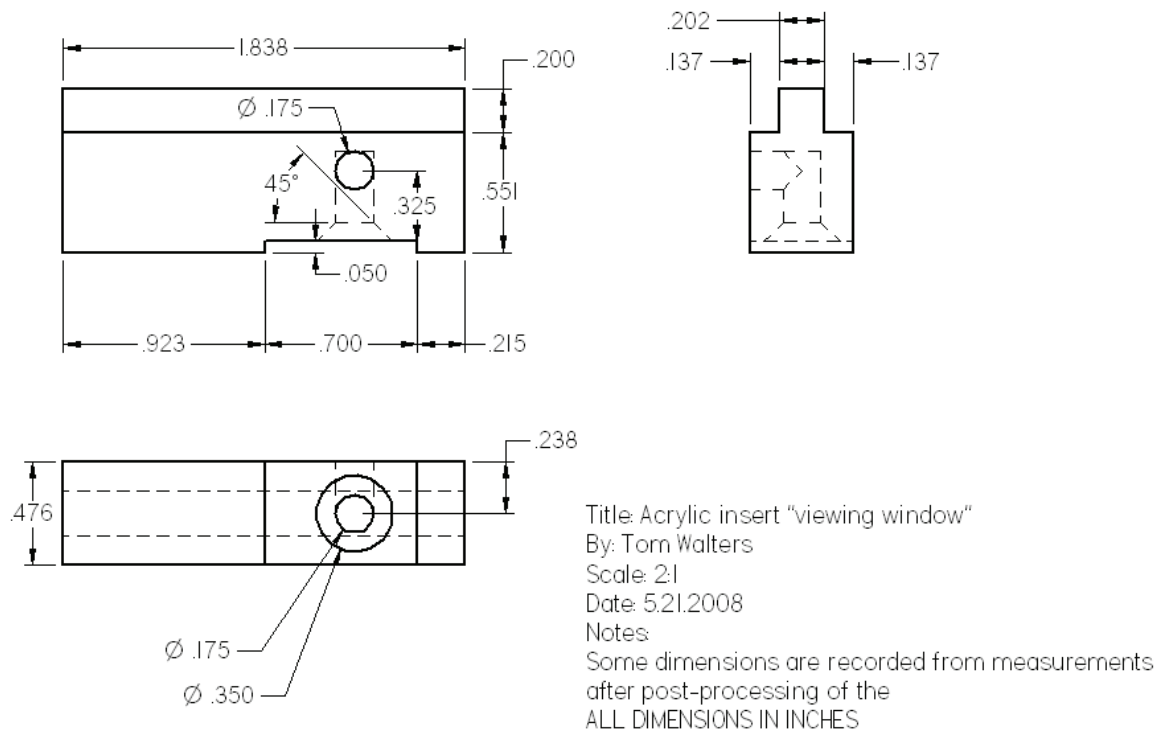


Figure C.1: Detailed drawing of acrylic insert “viewing window” for in situ valve characterization.

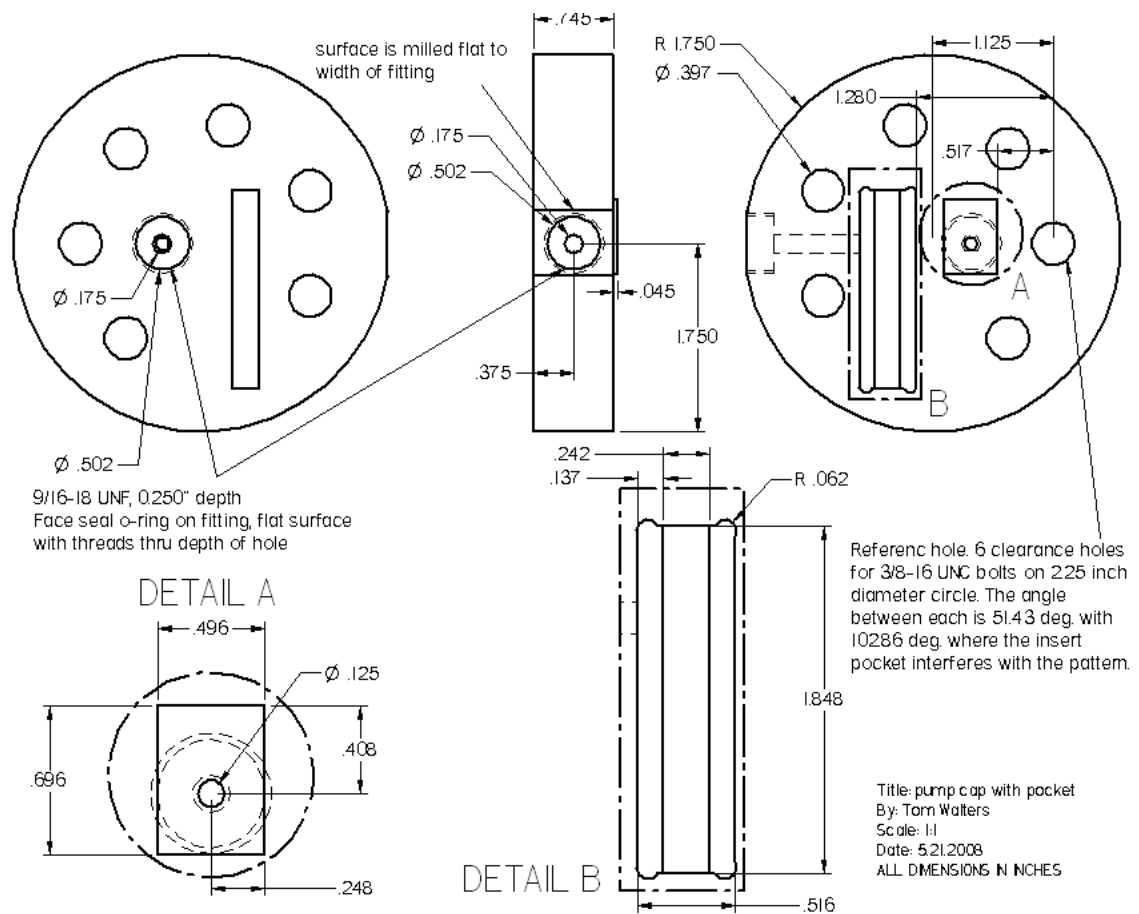


Figure C.2: Detailed drawing of modified pump cap for in situ valve characterization.

## BIBLIOGRAPHY

- [1] Etrema products, inc. Core technology: What is galphenol? Website, 2008. <http://www.etrema-usa.com/core/galphenol/>.
- [2] F. Ahmadkhanlou, J.L. Zite, and G. Washington. “A magnetorheological fluid-based controllable active knee brace”. volume 6527, page 65270O. SPIE, 2007.
- [3] Robert D. Blevins. *Formulas for Natural Frequency and Mode Shape*. Krieger Publishing Company, 2001.
- [4] Diann Brei, Jonathan Luntz, John Shaw, Nancy L. Johnson, Alan L. Browne, Paul W. Alexander, and Nilesh D. Mankame. “General Motors and the University of Michigan smart materials and structures collaborative research laboratory”. volume 6527, page 65270U. SPIE, 2007.
- [5] Elizabeth A. Bretz. “By-wire cars turn the corner”. *IEEE Spectrum*, pages 68–73, 2001.
- [6] K. Bridger, J. M. Sewell, A. V. Cooke, J. L. Lutian, D. Kohlhafer, G. E. Small, and P. M. Kuhn. “High-pressure magnetostrictive pump development: a comparison of prototype and modeled performance”. In E. H. Anderson, editor, *Smart Structures and Materials 2004: Industrial and Commercial Applications of Smart Structures Technologies*, volume 5388 of *Proc. SPIE*, pages 246–257, 2004.
- [7] F.T. Calkins. *Energy-based hysteresis model for magnetostrictive transducers*. PhD thesis, Iowa State University, Ames, IA, 2000.
- [8] NASA Dryden Flight Research Center. F-8 digital fly-by-wire aircraft, 2002.
- [9] P. Chang, A. Flatau, and S. Liu. “Review paper: Health monitoring of civil infrastructure”. *Structural Health Monitoring*, 2(3):257–267, 2003.
- [10] E. G. Chapman, S. L. Herdic, C. A. Keller, , and C. S. Lynch. “Development of miniaturized piezo-hydraulic pumps”. In E. V. White, editor, *Smart Structures and Materials 2005: Industrial and Commercial Applications of Smart Structures Technologies*, volume 5762 of *Proceedings of SPIE*, pages 299–310, 2005.

- [11] A. Chaudhuri and N.M. Wereley. “Dynamic model of a hybrid hydraulic actuator utilizing different smart materials”. In *2007 ASME International Mechanical Engineering Congress and Exposition*, Proc. IMECE '07, 2007.
- [12] A. Chaudhuri, J.-H. Yoo, and N.M. Wereley. “Dynamic modeling of a magnetostrictive hydraulic pump”. In *2006 ASME International Mechanical Engineering Congress and Exposition*, Proc. IMECE '06, 2006.
- [13] A. Chaudhuri, J.-H. Yoo, N.M. Wereley, and N. Nersessian. “Scaling-up issues with a magnetostrictive hydraulic pump”. In *2006 ASME International Mechanical Engineering Congress and Exposition*, Proc. IMECE '06, 2006.
- [14] A.E. Clark, J.B. Restorff, M. Wun-Fogle, and J.E. Lindberg. “Magnetoelastic coupling and  $\Delta E$  Effect in  $Tb_x Dy_{1-x}$  single crystals”. *Journal of Applied Physics*, 73:6150–6152, 1993.
- [15] R.F. Cusak. Patent: Magnetostrictive pump, September 1986.
- [16] M. J. Dapino. “On magnetostrictive materials and their use in adaptive structures”. *Journal of Structural Engineering and Mechanics*, 17:303–329, 2004.
- [17] M. J. Dapino. ME794M course notes, 2005.
- [18] Marcelo Dapino. *Nonlinear and hysteretic magnetomechanical model for magnetostrictive transducers*. PhD thesis, Iowa State University, Ames, IA, 1999.
- [19] M.J. Dapino, R. Singh, and G. Washington. NSF I/UCRC: Smart Vehicle Concepts Center. Website, 2007.
- [20] Ernest O. Doebelin. *System Dynamics: Modeling and Response*. Charles E. Merrill Publishing Company, 1972.
- [21] J. Ellison. Investigation of active materials as driving elements in a hydraulic-hybrid actuator. Master’s thesis, University of Maryland, College Park, MD, 2004.
- [22] J. Ellison, J. Sirohi, and I. Chopra. “Design and testing of a bidirectional magnetostrictive-hydraulic hybrid actuator”. In A. Flatau, editor, *Smart Structures and Materials 2004*, volume 5309 of *Proc. SPIE*, pages 483–494, 2004.
- [23] Goran Engdahl. *Handbook of Giant Magnetostrictive Materials*. Academic Press, 2000.
- [24] M. J. Gerver, James H. Goldie, John R. Swenbeck, P. Jones R. Shea, Robert T. Ilmonen, David M. Dozor, S. Armstrong, R. Roderick, Francis E. Nimblett, and R. Iovanni. “Magnetostrictive water pump”. In *Proceedings of SPIE Smart Structures and Materials*, pages 694–705, San Diego, CA, 1998.

- [25] W.E. Hurst. Piezohydraulic actuator design and modeling using a lumped-parameter approach. Master's thesis, Virginia Polytechnic Institute and State University, Blacksburg, VA, 2002.
- [26] S. John, C. Cadou, J-H Yoo, , and N. Wereley. "Application of CFD in the design and analysis of a piezoelectric hydraulic pump". *Journal of Intelligent Material Systems and Structures*, page Preprint, 2004.
- [27] S. John, A. Chaudhuri, and N.M. Wereley. "A magnetorheological actuation system: test and model". *Smart Materials and Structures*, 17(2):025023 (15pp), 2008.
- [28] S. John, J. Sirohi, G. Wang, and N.M. Wereley. "Comparison of piezoelectric, magnetostrictive, and electrostrictive hybrid hydraulic actuators". *Journal of Intelligent Material Systems and Structures*, 18:1035–1048, 2007.
- [29] S. John, J.H Yoo, J. Sirohi, and N.M. Wereley. "Bi-directional actuation of a piston using MR valves and a piezoelectric pump". In *2005 ASME International Mechanical Engineering Congress and Exposition*, Proc. IMECE '05, 2005.
- [30] Yury Kalish and Naeim A. Henein. "Stress analysis of multilayer piezoelectric actuators for diesel fuel injection subjected to square pulse voltage excitation". volume 6527, page 65270T. SPIE, 2007.
- [31] R. Kellogg and A. Flatau. "Blocked force investigation of a Terfenol-D transducer". In *International Symposium on Smart Structures and Materials*, volume 3668-19 of *Proceedings of SPIE*, 1999.
- [32] Rick Kellogg. The Delta-E effect in Terfenol-D and its application in a tunable mechanical resonator. Master's thesis, Iowa State University, Ames, IA, 2000.
- [33] K. Konishi, T. Yoshimura, K. Hashimoto, and N. Yamamoto. "Hydraulic actuators driven by piezoelectric elements (1<sup>st</sup> report, trial piezoelectric pump and its maximum power". *J. Japan Soc. Mech. Eng*, C 59, 1993.
- [34] T. Lee and I. Chopra. "Design issues of a high-stroke, on-blade piezostack actuator for a helicopter rotor with trailing edge flaps". *Journal of Intelligent Material Systems and Structures*, 11:328–342, 2000.
- [35] L. D. Mauck and C. S. Lynch. "Piezoelectric hydraulic pump development". *Journal of Intelligent Material Systems and Structures*, 11:758–764, 2000.
- [36] T. Naik, E.K. Longmire, and S.C. Mantell. "Dynamic response of a cantilever in liquid near a solid wall". *Sensors and Actuators A*, 102:240–254, 2002.

- [37] D. Nosse. “Compact actuation through magnetorheological flow control and rectification of magnetostrictive vibrations”. Master’s thesis, The Ohio State University, Columbus, Ohio, 2005.
- [38] D. Nosse and M. Dapino. “Magnetorheological valve for hybrid electrohydrostatic actuation”. *Journal of Intelligent Material Systems and Structures*, 18:1121–1136, 2007.
- [39] C. O’Neill and J. Burchfield. “Kinetic Ceramics piezoelectric hydraulic pumps”. In L. Porter Davis, editor, *Industrial and Commercial Applications of Smart Structures Technologies 2007*, volume 6527 of *Proc. SPIE*, page 65270I, 2007.
- [40] D. Roberts, H. Li, J. Steyn, O. Yaglioglu, and S. Spearing. “A piezoelectric microvalve for compact high-frequency, high-differential pressure hydraulic micropumping systems”. *Journal of Microelectromechanical Systems*, 12(1):81–92, Feb 2003.
- [41] M. Rupinsky and M. J. Dapino. “Smart material electrohydrostatic actuator for intelligent transportation systems”. In *2006 ASME International Mechanical Engineering Congress and Exposition*, Proc. IMECE ’06, 2006.
- [42] Michael J. Rupinsky. Smart material electrohydrostatic actuator for intelligent transportation systems. Master’s thesis, The Ohio State University, Columbus, OH, 2006.
- [43] J. Sirohi, C. Cadou, , and I. Chopra. “Investigation of the dynamic characteristics of a piezohydraulic actuator”. *Journal of Intelligent Material Systems and Structures*, 16:481–492, 2005.
- [44] J. Sirohi and I. Chopra. “Development of a compact piezoelectric-hydraulic hybrid actuator”. In *Smart Structures and Materials 2001*, volume 4327 of *Proc. SPIE*, pages 401–412, 2001.
- [45] J. Sirohi and I. Chopra. “Design and development of a high pumping frequency piezoelectric-hydraulic hybrid actuator”. *Journal of Intelligent Material Systems and Structures*, 14:135–147, 2003.
- [46] R. Smith. “*Smart material systems: model development*”. Frontiers in applied mathematics, 2005.
- [47] R.C. Smith, C. Bouron, and R. Zrostlik. “Partial and full inverse compensation for hysteresis in smart material systems”. *American Control Conference*, 4:2750–2754 vol.4, 2000.

- [48] R.C. Smith, M. Salapaka, A. Hatch, J. Smith, and T. De. “Model development and inverse compensator design for high speed nan positioning”. In *Conference on Decision and Control*, Proceedings of the 41st IEEE, pages 3652–3657, 2002.
- [49] R. Sneed, R. Smith, M. Cash, and E.H. Anderson. “Smart-material based hydraulic pump system for actuation of a morphing wing”. In *Adaptive Structures Conference*, Proc. AIAA, 2007.
- [50] H. Sodano, D. Inman, and G. Park. “A review of power harvesting from vibration using piezoelectric materials”. *The Shock and Vibration Digest*, 36:197–205, 2004.
- [51] Werner Soedel. *Sound and Vibrations of Positive Displacement Compressors*. CRC Press, 2007.
- [52] C.L. Stec. Patent: Piezoelectric pump, August 1962.
- [53] J-H. Yoo, J. Sirohi, and N. M. Wereley. “A magnetorheological piezohydraulic actuator”. *Journal of Intelligent Material Systems and Structures*, 16:943–953, 2005.
- [54] J-H. Yoo, J. Sirohi, N. M. Wereley, and I. Chopra. “A magnetorheological hydraulic actuator driven by a piezopump”. In *Proc. of IMECE*, 2003.